공학박사 학위논문

Development of mechanistic boiling heat partitioning model for horizontal tube under natural convection

자연대류 조건의 기구학적 수평 전열관 비등 열전달 모델 개발

2020 년 8 월

서울대학교 대학원
에너지시스템공학부
김 재 순

Development of mechanistic boiling heat partitioning model for horizontal tube under natural convection

자연대류 조건의 기구학적 수평전열관 비등열전달 모델 개발

지도교수 조 형 규

이 논문을 공학박사 학위논문으로 제출함
2020 년 8 월

서울대학교 대학원
에너지시스템공학부
김 재 순

김재순의 박사 학위논문을 인준함
2020 년 8 월

위 원 장	김 응 수	(인)
부위원장	조 형 규	(인)
위 원	이 유 호	(인)
위 원	어 동 진	(인)
위 원	김 형 대	(인)

Abstract

Development of mechanistic boiling heat partitioning model for horizontal tube under natural convection

Jae Soon Kim

Department of Energy System Engineering

The Graduate School

Seoul National University

Recently, new passive safety concepts have been proposed to enhance the system's performance and reliability that mostly incorporate shell-and-tube type heat exchangers in various configurations. Especially, the boiling phenomena within the heat exchanger geometry need to be examined experimentally and analytically because the heat transfer is significantly dependent on the configuration.

The heat-partitioning model is mechanistic boiling model and can directly reflect the mechanism of vapor bubble generation and actual phenomena. In this model, the boiling heat transfer can be calculated from bubble-related parameters such as the volume, velocity, frequency, and other influencing factors. Because of these advantages, it is currently widely used for predicting boiling heat transfer in computational fluid dynamics (CFD) codes. The bubbles generated on the horizontal tube display different characteristics depending on the generation

location. This characteristic of the bubble behavior directly affects the boiling heat transfer. Thus, a mechanistic boiling model with a detailed heat transfer mechanism for boiling is needed to consider the bubble motion

However, previous mechanistic boiling models were mostly developed for upward-facing plate surfaces or vertical tubes. Also, previous studies did not consider the curvature effect of a horizontal tube. Only Sateesh et al. (2005) considered the curvature effect and sliding of bubbles when modeling boiling heat transfer for a horizontal tube. However, their sub-models rely on a simplified analysis of the sliding bubble motion rather than on experimental data. In this context, appropriate sub-models explicitly applicable to horizontal tube boiling have not yet been proposed. Besides, the bubble life-cycle related parameters (e.g. bubble growth model, bubble velocity model, bubble departure model, bubble departure frequency model, bubble lift-off model, sliding length and area, and sliding interactions) have not been validated or experimentally conducted for use in horizontal tube conditions.

Therefore, the main objectives of the present work were developing the heat partitioning model for the horizontal tube. For this goal, single bubble boiling experiments on the horizontal tube outside were conducted. A series of experiments were conducted to observe the bubble behavior under saturated boiling conditions on the outside of a horizontal tube. Through the experiment, bubble growth rate, bubble velocity, contact diameter, bubble departure frequency, bubble departure diameter, etc. were obtained. Also bubble sub-models were developed based on the results. A specially devised heater was fabricated for visualization experiment and boiling bubbles were generated along a thin heated surface to facilitate observation of a single bubble’s motion. Also, an image processing methodology for the

analysis of experimental results was developed. By taking advantage of bubble incipience in the controlled area, accurate measurement of the dynamic bubble motion parameter became feasible with a digital image processing technique.

Along with the development of the bubble sub-models, the force balance model was modified to cylindrical coordinates to predict the sliding bubble behavior considering the curvature effect. The force balance model was validated by comparison of the predicted bubble velocity with the experimental data. In addition, a bubble departure diameter model was developed, and the bubble radius model and the frequency model were closed using the experimental results. Besides, the bubble merging, the lift-off diameter, and the distribution of nucleation sites, which is difficult to simplify due to the complex characteristics of the boiling phenomenon, were modelled through numerical method. Combining the sub-models, the mechanistic heat transfer model was established by determining the area ratio and heat flux for each heat transfer mechanism.

Moreover, the developed model was validated against to various previous horizontal tube experiments and PASCAL experiments in which pressure and subcooling continued to change. As a validation results, experimental results were reasonably well predicted by the developed boiling heat transfer model.

This study presents experimental techniques and measurement results for observing vapor bubble sliding phenomena, deriving the force balance equation, sub-model development results, heat transfer model development results, and validation results. It is expected that the developed model can be used to improve the boiling heat transfer model of system analysis codes or CFD model with the coupling method in the future.

Keywords

Boiling, Horizontal tube, Wall heat flux, Mechanistic model, Heat partitioning model, FPCB heater, Single bubble, Natural convection, Sliding bubble, Force balance model, Bubble velocity, Bubble merge, Bubble tracking, nucleation sites distribution, Monte-Carlo method, PAFS, PASCAL

Student Number: 2015-30289

List of Contents

List of Figures

List of Tables

Chapter 1

Introduction

1.1 Background and motivation

Precisely predicting the boiling heat transfer is important for analyzing the safety of a nuclear reactor because it takes place in various components (e.g., the reactor core, steam generator, and heat exchangers of safety systems) of the system under both normal and transient conditions. Recently, new passive safety concepts have been proposed to enhance the system's performance and reliability (Bae et al., 2012) that mostly incorporate shell-and-tube type heat exchangers in various configurations. In order to evaluate their performance accurately and confirm the integrity of a nuclear reactor at the time of an accident, the heat transfer phenomena in these heat exchangers need to be investigated. Especially, the boiling phenomena within the heat exchanger geometry need to be examined experimentally and analytically because the heat transfer is significantly dependent on the configuration.

The present study focused on the boiling heat transfer on the outer surface of a horizontal tube. This occurs frequently in industrial-purpose shell-and-tube type heat exchangers for which the shell side is a heat sink where boiling occurs. Particularly in the nuclear industry, this phenomenon is utilized to remove the decay heat that is generated in the reactor core in transient and accident situations. For

example, APR+ (an advanced GEN-III reactor developed by Korea Hydro and Nuclear Power, KNHP) is equipped with a passive auxiliary feedwater system (PAFS) (Bae et al., 2012). PAFS incorporates a heat exchanger comprising horizontal U-tube bundles submerged in a large water pool and is connected to the secondary side of the steam generator, as shown in Figure 1. 1. During an accident, the steam generated in the steam generator transfers to the heat exchanger. It flows inside the heat exchanger tubes, condenses, and then returns to the steam generator by the gravity. Meanwhile, the heat of the condensation is released to the water pool through the tubes of the heat exchanger, which generates vapor bubbles on their outer surfaces.

The bubbles generated on the horizontal tube display different characteristics depending on the generation location, as shown in Figure 1. 2. The bubbles on the upper part of the tube detach from the surface, which is predominantly analogous to a pool boiling on a horizontal plate. However, bubbles on the lower part slide along the downward-facing heated surface after departure and grow as they slide until they lift off from the surface. This characteristic of the bubble behavior directly affects the boiling heat transfer. Thus, a mechanistic boiling model with a detailed heat transfer mechanism for boiling is needed to consider the bubble sliding motion. The sliding bubbles on the downward-facing heated surface appear not only on the horizontal heat exchanger tubes but also in other safety systems of nuclear reactors, such as the IVR-ERVCS (In-Vessel Retention of molten corium through External Reactor Vessel Cooling) (Theofanous et al., 1997), core catchers (Lee et al., 2013), and isolation condenser (Gluntz & Cooke, 1991). In this context, studying the sliding motion along a downward-facing heated surface is an important part of developing an enhanced boiling model applicable to safety systems. Accordingly,

models that consider this phenomenon have been proposed in previous studies.

Boiling models for analyzing the heat transfer rate can be classified into classical and mechanistic models. The former is developed by regressing experimental results with respect to various conditional parameters, and the latter incorporates each mechanism that reflects the boiling heat transfer principle. Examples of classical correlations include those by Chen (1966), Kutateladze (1961), Polley et al. (1980), Singh et al. (1985), Hwang and Yao (1986), and Webb and Gupte (1992). Most of the widely used classical nucleate boiling correlations are based on Chen's model (1966), which was developed for the flow boiling in a vertical tube and calculated from the sum of the single-phase convection heat transfer and two-phase boiling heat transfer. Although many researchers have improved upon this model according to various geometries, fluid, and flow conditions, their work has been limited in that they could not directly reflect the detailed mechanism of the boiling heat transfer and relied on empirical fitting to experimental data.

The heat-partitioning model is mechanistic and can directly reflect the mechanism of vapor bubble generation and actual phenomena. Researchers have been especially attracted by the extensibility of the model since it was first proposed by Kurul and Podowski (1990). In this model, the boiling heat transfer can be calculated from bubble-related parameters such as the volume, velocity, frequency, and other influencing factors. Because of these advantages, it is currently widely used for predicting boiling heat transfer in computational fluid dynamics (CFD) codes. The model has been continuously improved by different groups such as Sateesh et al. (2005), Basu et al. (2005), Yeoh et al. (2008), and Gilman and Baglietto (2017). As an example, the heat-partitioning model proposed by Sateesh

et al. for a horizontal tube is given below:

$$q_{tot} = (q_{me} + q_{tc})\chi_{st} + (q_{mes} + q_{tcs})\chi_s + q_{nc}, \quad (1.1)$$

where q_{tot} is the total heat flux, q_{me} is the heat flux due to microlayer evaporation and superheated layer evaporation for stationary bubbles, q_{tc} is the heat flux due to transient conduction for stationary bubbles, q_{mes} is the heat flux due to microlayer evaporation for sliding bubbles, q_{tcs} is the heat flux due to transient conduction for sliding bubbles, q_{nc} is the heat flux due to natural convection, χ_{st} is a parameter defined by the projected area and nucleation site density for stationary bubbles, and χ_s is a parameter defined by the projected area, nucleation site density, and χ_{st} for sliding bubbles.

Evaporation means the heat transferred by two mechanisms of evaporation to bubbles; one is the evaporation from a thin microlayer under the bubble; and the other the one from superheated layer around the bubble surface. In the case of a subcooled boiling condensation may occur on the bubble surface around the subcooling liquid (Figure 1. 3). As an example, the equations of evaporation and condensation are proposed as follows by Yoo et al. (2018):

Microlayer evaporation

$$q''_{ev,ml} = \sqrt{\frac{k_s \rho_s c_s}{k_l \rho_l c_{p,l}}} Pr^{-0.5} \left(\rho_l c_{p,l} \Delta T_w\right) {\alpha_l}^{0.5} t_{sl}^{-0.5} \quad (1.2)$$

Superheated liquid layer evaporation

$$q''_{ev,sLL} = \frac{b k_l \Delta T_w}{\sqrt{\pi \alpha_l t_{sl}}} \quad (1.3)$$

Condensation

$$q_c^{"} = h_c \Delta T_{sub} \tag{1.4}$$

Condensation heat transfer coefficient

$$h_c = \frac{C h_{fg} D_b}{2\left(\frac{1}{\rho_g} - \frac{1}{\rho_f}\right)} \tag{1.5}$$

where,

$\Delta T_w = T_w - T_{sat}$

C: empirical constant

Yu et al. (2018) experimentally confirmed the existence of the microlayer under the bubble using a synchrotron x-ray.

Transient conduction refers to a phenomenon in which quenching occurs and heat transfer is temporarily enhanced as the surrounding fluid flows into the place of the superheated layer that has been removed apart as the bubble passes. The degree of heat transfer enhancement can be expressed as shown in Figure 1. 4. The heat transfer is instantaneously enhanced, and the enhancement gradually decreases with time. The effect of the transient conduction diminishes as the heat transfer approaches to that of the single-phase convection. In general, the equation of transient conduction is expressed as follows.

Transient conduction

$$q_{tc}" = \int \frac{k_l(T_w - T_l)}{\sqrt{\pi \alpha_l t}} dt \quad (1.6)$$

Transient conduction was experimentally confirmed by IR experiments by Yoo et al. (2018).

From the heater wall point of view, the single-phase convection occurs in the remaining areas where microlayer evaporation and transient conduction do not occur (Figure 1. 5). In this case, a correlation derived according to the thermal-hydraulic conditions of the problem is generally used.

The heat partitioning model has been continuously improved by several researchers since it was first proposed by Podowski (1990). Sateesh considered sliding in Podowski's model and predicted the total heat transfer by dividing each case into a stationary bubble and a sliding bubble case for microlayer evaporation and transient conduction. Basu (2005) also considered the sliding of the bubbles, and the total heat transfer was calculated by dividing the cases onto bubble sliding conditions and stationary conditions. Most recently, Gilman's (2017) study improved the model based on Basu's assumptions through a stochastic approach to bubble merging and nucleation site growth. However, the existing models include unrealistic assumptions to simplify the problem for analytical calculations. Representatively, the models assume that the nucleation site is uniformly arranged in the form of a grid, which is significantly different from the actual phenomenon. Besides, the timing of bubbles merge is simplified without considering the mechanistic characteristics of the boiling.

Moreover, for using the existing heat partitioning model in horizontal tube

conditions, there are various limitations in the application of each variable. The heat partitioning model includes microlayer evaporation and transient conduction for both stationary bubbles and sliding bubbles. In order to apply a heat-partitioning model accurately, parameters associated with the bubble motion such as the bubble velocity and bubble volume (or bubble radius) are of great importance. For example, the transient conduction of sliding bubbles q_{tcs} in Eq. (1.1) can be expressed with the following sub-model:

$$q_{tcs} = 2\sqrt{\frac{k_l \rho_l C_{pl}}{\pi t_w}} \Delta T n_b t_w f \int_{t_d}^{t_l} K 2 r_b(t) U_b(t) dt, \quad (1.7)$$

where U_b and r_b are the bubble velocity and bubble radius, respectively. Eq. (1.7) represents the transient conduction, and the terms directly include the velocity and radius of a sliding bubble. The bubble radius and velocity during sliding are also included in the remaining terms of Eq. (1.1) and are important factors in predicting wall heat transfer.

Each bubble variable greatly affects the overall heat transfer prediction performance. Even though it is very important to accurately acquire the variables, there are still insufficient horizontal tube experimental results that can be used for model verification or development. In particular, most experiments are focused on a vertical plane or a horizontal plane geometry, and for horizontal tubes, experimental results obtained from single bubble tests do not exist yet.

In the horizontal tube geometry, not only the experimental results, but also the model and verification results for the bubble variables are insufficient (Table 1. 1). A force balance model, bubble size model, bubble velocity model, bubble frequency model, and bubble merging model, etc. are needed to predict the bubble behavior

on a horizontal tube so that the total heat transfer can be predicted through the mechanistic model. Nucleation site density models, area of influence, and single-phase convection models can use existing ones. The nucleation site density represents the number of bubble generation sites per unit area on the surface. The area of influence represents the ratio of the area affected by the sliding bubble and the area where transient conduction occurs. However, the bubble growth model, bubble velocity model, bubble departure model, bubble departure frequency model, bubble lift-off model, sliding length and area, and sliding interactions have not been validated or experimentally conducted for use in horizontal tube conditions.

A force balance model is needed to predict the bubble behavior. Klausner et al. (1993) proposed a force balance model that can calculate the forces acting on bubbles and subsequently predict the velocity, bubble departure, and lift-off. Their model has been modified by many researchers to expand its coverage and apply it as a sub-model for heat partitioning (Yun et al., 2012, Sugrue et al., 2014). However, this model was developed for horizontal plates and needs to be adapted for cylindrical coordinates to apply to horizontal tubes.

For bubble velocity in the existing heat partitioning model, a simple assumption was used. For these conditions, the bubble velocity was assumed to be the same as the flow velocity of the surrounding liquid (Gilman & Baglietto, 2017) or half the fluid velocity (Bae et al., 2010) due to the environment with a high Reynolds number. However, in the mechanistic model at pool boiling or natural convective condition, the bubble velocity greatly affects the evaporation to single-phase convection and transient conduction.

The bubble growth model has been proposed by many researchers. Plesset and Zwick (1954), Scriven (1959), Zuber (1961), Mikic et al. (1970), Ünal (1976), Yun

et al (2010), Colombo and Fairweather (2015), and Hoang et al. (2016) have all proposed models for predicting the bubble growth and radius.

However, these models were mostly developed for upward-facing plate surfaces or vertical tubes. Although Maity (2000) and Qiu & Dhir (2002) studied boiling heat transfer on downward-facing inclined planes, they did not consider the curvature effect of a horizontal tube. Sateesh et al. (2005) considered the curvature effect and sliding of bubbles when modeling boiling heat transfer for a horizontal tube. However, their sub-models rely on a simplified analysis of the sliding bubble motion rather than on experimental data. In this context, appropriate sub-models explicitly applicable to horizontal tube boiling have not yet been proposed.

1.2 The objective of the present study

The main objective of the present work was to develop the heat partitioning model for the horizontal tube. The overview of the study is schematically shown in Figure 1. 6. For this goal, experiments in a horizontal tube were conducted. Also, an image processing methodology for experiments was developed. Experimental results and trends of the bubble parameters were obtained through experiments, and sub-models of the bubble parameters were developed through the results. In addition, the bubble merging and lift-off, which is difficult to simplify due to the complex characteristics of the boiling phenomenon, was obtained through numerical modeling. Through the developed sub-model and numerical model, a mechanical heat transfer model that can be used in horizontal tubes was developed.

A series of experiments were conducted to observe the bubble behavior under boiling conditions on the lower surface of a horizontal tube. Through the

experiment, bubble growth under the horizontal tube condition, bubble velocity, contact diameter, bubble departure frequency, and bubble departure diameter, etc. were obtained. A specially devised heater was fabricated for this purpose and boiling bubbles were generated along a thin heated surface to facilitate observation of a single bubble's motion. By taking advantage of bubble incipience in the controlled area, accurate measurement of the bubble motion became feasible along with a digital image processing technique.

Before developing the bubble sub-models, a force balance model was derived to predict the sliding bubble behavior, where the curvature effect was included in an existing force balance model and cylindrical coordinates were adopted. The force balance formula was validated by comparison of the predicted bubble velocity with the experimental data. Moreover, a bubble departure diameter model was developed, and the bubble radius model and the frequency model were selected based on the comparison result with the experimental results.

Next, through the numerical modeling, the mechanistic heat transfer model was completed by determining the area ratio and heat flux for each heat transfer mechanism, along with the bubble merging, lift-off diameter, and transient conduction. The model can generate bubble nucleation sites randomly or uniformly according to the options. In the case of randomly distributed sites, the average value and range of the calculation results were obtained using the Monte-Carlo method.

The developed model was validated by experiments conducted with various tube diameters and PASCAL experiments in which pressure and subcooling continuously changed. As a result, the model reasonably predicted the wall heat flux.

This study presents experimental techniques and measurement results for

observing vapor bubble sliding phenomena, deriving the force balance equation, sub-model development results, heat transfer model development results, and validation results.

Table 1. 1 Classification of previous sub-models for horizontal tube

Bubble life cycle	**Development or validation necessary**	**Existing models applicable**
Growth	Bubble growth	Active nucleation sites
Departure	Bubble departure	-
	Bubble departure frequency	
Sliding	Bubble sliding velocity	Area of influence
	Sliding interactions	
	Sliding distance and area	
Lift-off	Bubble lift-off	-
Heat transfer mechanism	-	Evaporation
		Transient conduction
		Single-phase convection

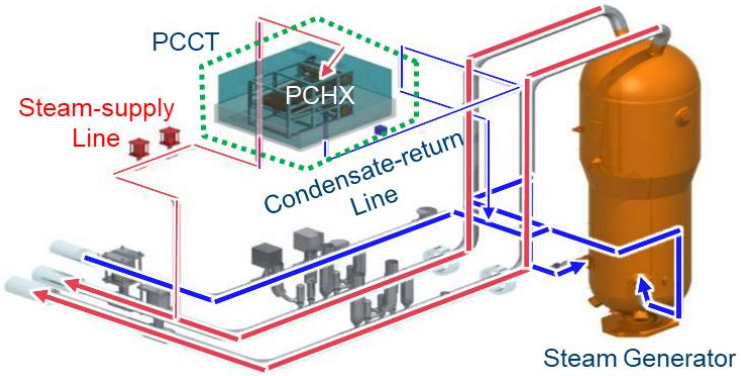

(a)

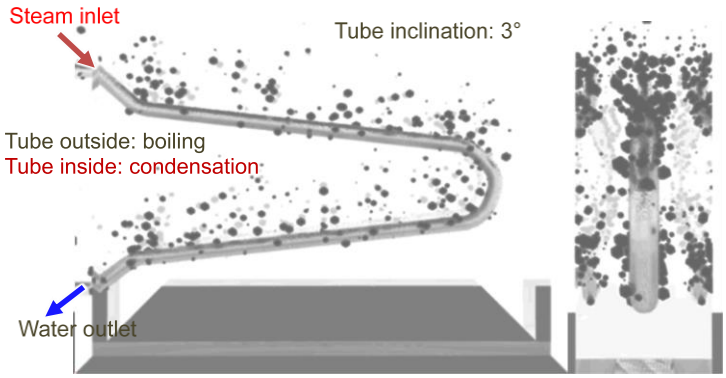

(b)

Figure 1. 1 Passive auxiliary feedwater system and illustration of boiling phenomena: (a) PAFS system configuration (Kang et al., 2012) and (b) boiling heat transfer on the heat exchanger tube.

(a)

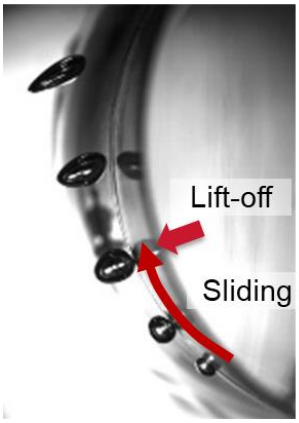

(b)

Figure 1. 2 Different bubble movements on the horizontal tube: (a) upper half and

(b) lower half.

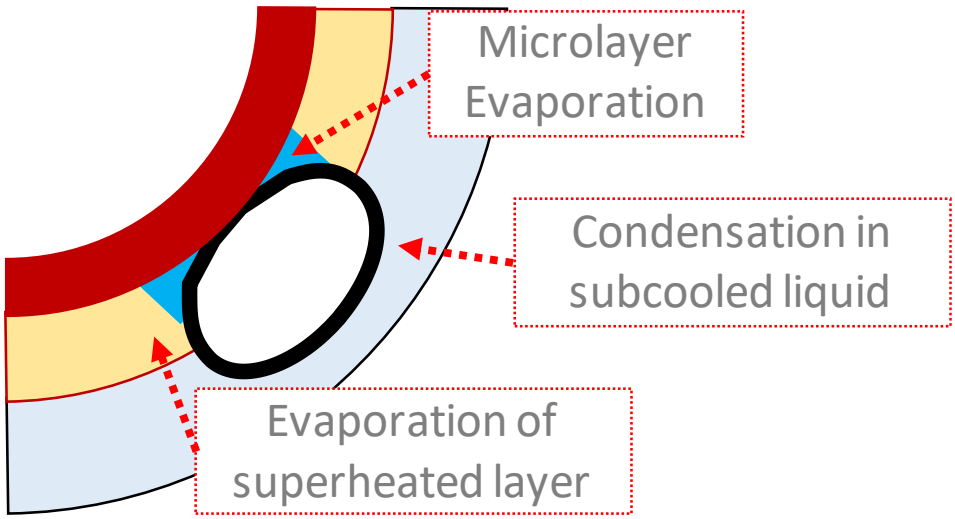

Figure 1. 3 Bubble growth mechanism

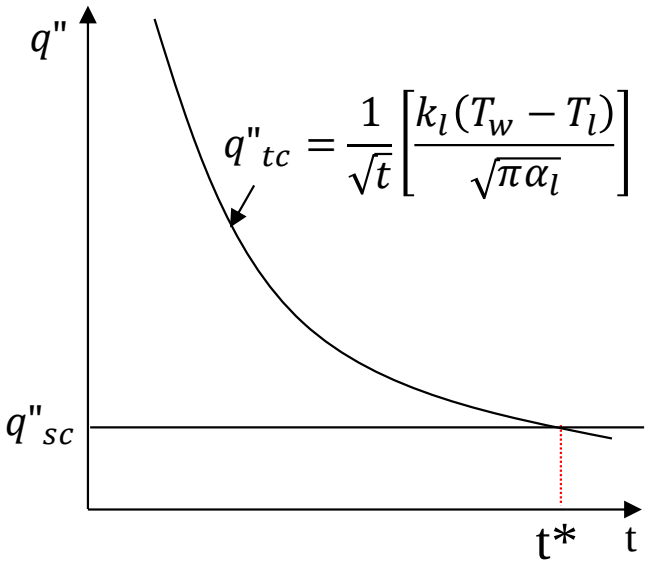

Figure 1. 4 Transient conduction heat flux

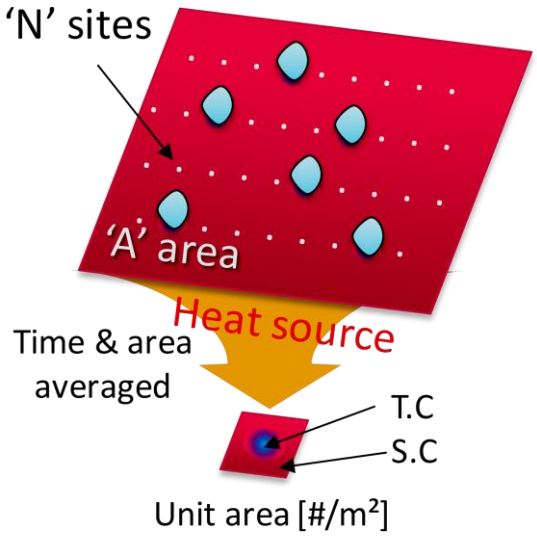

Figure 1. 5 Area of single-phase convection

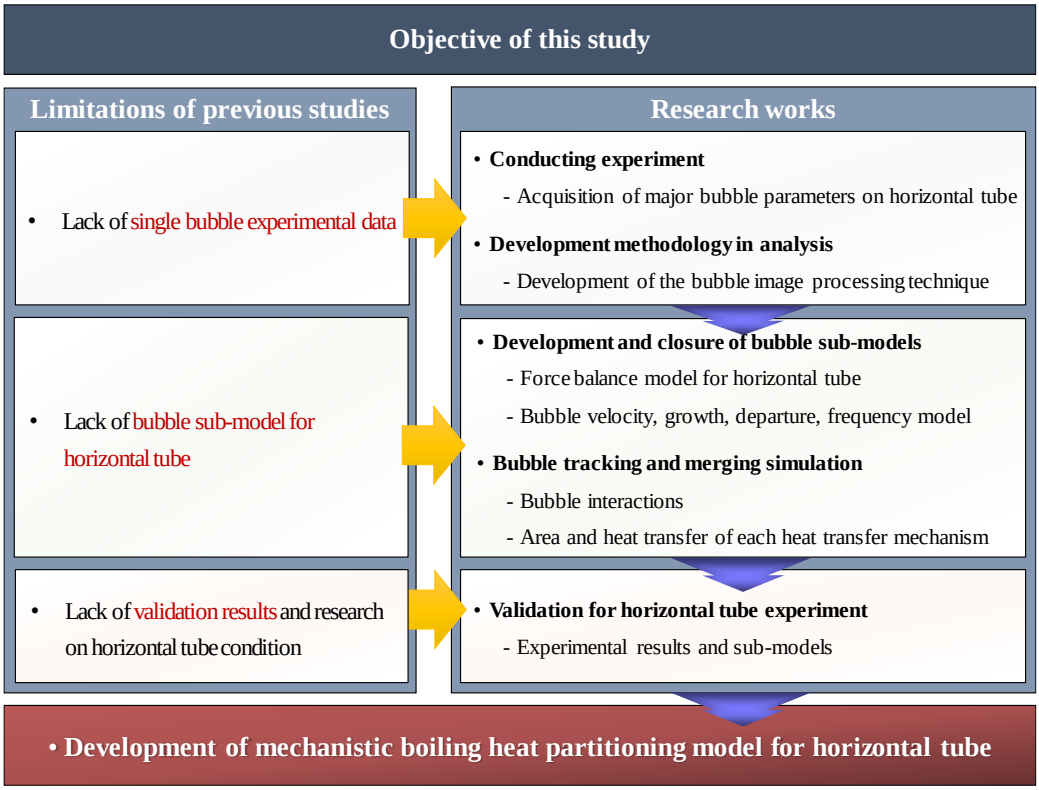

Figure 1. 6 Research overview

Chapter 2.

Experiment

2.1 Purpose of the experiment

As shown in Eq. (1.2), the bubble sliding velocity, bubble frequency, radius (or volume) transient, departure diameter, waiting time, growth time and contact diameter were required to develop sub-models of the heat partitioning. However, in previous studies, single bubble experimental results and sub-models that can be used in horizontal tube conditions do not exist or have not been validated under horizontal tube conditions. In particular, although these bubble sub-models are desired to be developed based on a single boiling bubble experiment in order to be used in a mechanistic model, most of the experimental results have not yet existed due to the difficulties of the experiment. Therefore, in this study, experiment loops and special heaters were manufactured and experiments were performed to measure the main parameters under horizontal tube conditions.

2.2 Experimental apparatus

2.2.1 Experimental loop

Figure 2. 1 shows the experimental loop, which included a water tank, pump, preheater, test section, and heat exchanger connected to a chiller. The water was supplied from the water tank by the pump and heated to the saturation temperature by the preheater. The saturated water was boiled through the heater installed inside the test section. The heat exchanger was installed at the exit of the test section to condense the vapor bubbles, created a subcooled liquid. The cooled water was transferred to the water tank for circulation. The preheater was used for boiling for more than two hours before the experiment to deaerate dissolved non-condensable gases.

2.2.2 Test section

The configuration and size of the test section are shown in Figure 2. 2. The test section was a 0.11 m × 0.11 m transparent square duct made of polycarbonate for visualization. The test section height was 0.5 m, and a flow straightener was installed at the inlet to flatten the velocity profile. At the middle elevation of the test section, a specially designed heater rod was located with a diameter of 50 mm. The diameter was determined according to the heat exchanger tube diameter of PAFS in APR+ (Bae et al., 2012).

2.2.3 Measurement devices

The measurement parameters of the experiment are shown in Figure 2. 1. The flow rate was measured by a Coriolis flowmeter (RHM-17498, Rheonik) with a measurement range of 0–4.17 kg/s and a measurement error of less than ±0.3%. The pressure was measured by a Rosemount 2051CG with a ±0.01% span error, and the differential pressure between the inlet and outlet of the test section was measured by a Rosemount 2051CD with ±0.02% span error. T-type thermocouples manufactured by Omega were used to measure the liquid temperature with a measurement error of ±1 °C. The thermocouples were installed in the water storage tank, pump inlet and outlet, preheater chamber, test section inlet and outlet, and downstream of the heat exchanger, as indicated in Figure 2. 1. The measurement results were collected with a data acquisition system (NI9211, National Instruments).

2.2.4 Imaging devices

The bubble parameters of the experiment were measured with a digital image processing technique. Each experimental condition was photographed for 5 s. During this time, 90–320 bubbles were photographed depending on the conditions. The volume and velocity of the bubbles were averaged for the data acquisition duration to derive representative values for a specific condition. The images were acquired at 1000 fps from shadowgraphs using a high-speed camera (Phantom V711-16G-M) and backlighting.

2.2.5 Image processing methodology

The acquired images were binarised and analyzed to measure the bubble volume and velocity. Fig. Figure 2. 3 (a) shows the simplified sequence of the image processing. The procedure includes background image subtraction, binarisation, hole filling, edge smoothening, and verification. In the previous study, a pair of bubble images were recorded simultaneously with two synchronized high-speed cameras (Figure 2. 3(b)): one in the rod radial direction and the other in the rod axial direction. Then, a three-dimensional volume reconstruction method was applied to evaluate the bubble volume. If vapor bubbles were photographed in different directions at the same time, the top and bottom points are the same. Therefore, the axis connecting the top (highest) point and the bottom (lowest) point is used as a reference axis that both pictures can share. The bubble is cut by the height of this axis, and the distance from the reference point to the outermost point of the bubbles is assumed as the axis of the ellipse. In this way, four ellipses at height are obtained by using the total four axes as the axes of the ellipse. If it is stacked by height, the bubbles can be reconstructed in three dimensions. The result of the 3D-reconstruction of the bubbles is as shown in Figure 2. 4. It was confirmed that the 3D-reconstruction results are valid with photographed results. The image processing procedure is described in detail in the co-worker of the authors' previous study (Kim et al., 2017).

2.2.6 Verification of the image processing

Both uncertainties of the monoscopic and stereoscopic observation methods were verified using an imaginary phantom created by the CAD program. The verification procedure is described in detail in the co-worker of the authors' previous study (Kim et al., 2017). Phantom's features were selected based on the study by Kim et al. (2011). The estimated volume measurement error was in the range of −26.7%~33.4%. The best result was obtained with the observation angle of 45°. This result demonstrates that the monoscopic method may cause a significant error in estimating a volume of considerably deformed bubbles. Afterward, the same procedure was repeated with the stereoscopic analysis. For this, six pairs of images were used with observation angles of (0º, 90º), (15º, 105º), (30º, 120º), (45º, 135º), (60º, 150º), (75º, 165º). The present stereoscopic observation reduced the volume measurement error significantly into the range of −1.1%~4.7%. In particular, the error was lower than ±1.1% when the observation directions were in parallel with the semi-principal axes (observation angle pair: 0º and 90º), and the error was enlarged when the ellipsoid was visualized in the diagonal direction between the semi-principal axes (observation angle pair: 45º and 135º). It should be noted that the present experiment takes images from the axial and radial directions of the horizontal rod and they are in parallel with the semi-principal axes of the oblate bubbles. This implies that the present experimental setup and the observation angles can maximize the accuracy of the stereoscopic visualization method.

Based on the experimental data, the relation between the volume from the stereoscopic method and a conventional monoscopic method was established under

various flow and heat flux conditions (Figure 2. 5). The results indicated that the volume obtained with one camera in the axial direction was -30%–0% less than the volume obtained with the stereoscopic method. The reason for the underestimation is the bubble deformation pattern. In the monoscopic method, a horizontal cross-section of the bubble was assumed to have a circular shape. But the bubble volume is large and accelerated, it can be significantly deformed and have an ellipsoidal shape. Especially, the major axis of the ellipsoid is tilted from the horizon as the bubble moves along the circumferential direction of the horizontal heater. Owing to this, the volume estimated using the monoscopic method shows a significant variation with respect to the visualization direction. The views along the heater axial direction caused underestimation of the bubble volume and the other caused overestimation. In the present study, the database from the previous study was applied to evaluate the bubble volume from images obtained from the camera in the rod axial direction. This compensated for non-spherical bubble shapes in the bubble volume evaluation. The uncertainties of the measured bubble parameters were analyzed by combining the bias errors and precision errors. For the bubble volume measurement, the sources of uncertainty considered were (i) camera resolution (±13.87μm), (ii) volume compensation for the monoscopic method (±15% volume compensation error of the final volume result) and (iii) the precision uncertainty (Max. ±2.3mm³). For the bubble velocity measurement, the uncertainty sources below were considered; (i) camera resolution ($\pm 2.36 \cdot 10^{-3}$ m/s), and (ii) the precision uncertainty (Max. ±0.032m/s). These were included in the final measurement results and their error bars.

2.3 Narrow heater for single bubble experiment

2.3.1 Design and fabrication of special heaters

A conventional cartridge heater was not suitable for the present experiment; applying one would generate bubbles on the overall heated surface, and the overlapping bubbles would interrupt the visualization of important bubble behavior along the curved surface such as the moment of the bubble lift-off (Figure 2. 6). For this reason, a flexible heater was fabricated with a heating width of 3.0 mm and attached to a polycarbonate rod, as shown in Figure 2. 7 and Figure 2. 8. Preliminary experiments were conducted with varying heating thicknesses, and the optimized thickness result was 3.0 mm. The electric circuit of a flexible heater was manufactured using a Flexible Printed Circuit Board (FPCB). And Figure 2. 9 depicts the internal structure (layer) of the flexible heater. The surface of the heater had a small dent to create an artificial cavity where bubbles would be generated.

Because the devised heater generated bubbles on the controlled area, bubbles were generated along the narrow strip. This enhanced visualization of the bubble motion by avoiding overlap. This feature allowed bubble parameters to be measured through visualization along the heater rod axial direction, including the bubble contact length and moment of bubble lift-off as exemplified in Figure 1. 2.

2.3.2 Surface characteristics

The surface of the heating area was covered with a polyimide layer (FPCB) or copper. The roughness of a polyimide surface ranges from 12 to 35 nm (Fiorenza et

al., 2013) with a contact angle of 73.8°–76.9° (Cho et al., 2005, Gotoh et al., 2003, Figure 2. 10)

2.3.3 Artificial cavity

The number of nucleation sites depends on the surface properties of the heated surface. The cavity, consisting of a crevice and or a scratch, containing gas and/or vapor is the possible active nucleation site. The artificial cavity artificially creates a dent on the surface, creating an environment where bubbles are easily generated through trapped gas. The method of conducting an experiment by creating an artificial cavity on the surface has been used in studies such as Van Helder et al. (1995), Kandlikar & Stumm (1995), Yoshikawa & Colin (2010), and Rousselt (2014). In this study, the surface of the heater had a small dent with a diameter of approximately 100 μm (Figure 2. 11) for polyimide surfaced heater (FPCB) and 30 μm for copper surfaced heater (Figure 2. 12).

2.4 Preliminary experiment results

2.4.1 Sensitivity test on different heating width

Prior to conducting this experiment, the sensitivity of boiling according to the heating width was experimentally confirmed. As shown in Figure 2. 13 and Figure 2. 14, in the case of the heater with narrower than 1.0mm, the size of the individual bubbles is small and the generation frequency of the bubbles is very large. This was a sufficient condition for the formation of bubbles locally, but due to the lack of

formation of a superheated layer due to the narrow heating surface, the bubbles seem to grow relatively slowly. In addition, since the growth of bubbles is slow despite the same wall heat transfer, it is estimated that the frequency is increased due to less heat being transferred to the individual bubbles.

When the heating width is wider than 3.0mm, the bubble generation pattern is not different from the test with 1.0mm – 3.0 mm width, but as another nucleation sites are activated along the heater width direction, the bubble merge and overlapping in visualization were observed. For this reason, the heater width of 3.0 mm was selected for the present single bubble experiment.

2.4.2 Effect of the existence of an artificial cavity

The presence of the artificial cavity promotes the initial generation of bubbles through the trapped gas. In order to compare and confirm the difference in boiling phenomena due to the presence of artificial cavities, preliminary experiments were conducted separately by dividing the case with and without the cavity in the heater with the polyimide surface. There are many different roughness parameters in use, but Ra is by far the most common. The parameter Ra represents arithmetical mean deviation of the assessed surface profile. The surface of polyimide is relatively smooth compared to copper and SUS and has a small Ra value. In the absence of an artificial cavity, a higher wall heat flux was required for the bubble to be initiated for the first time. In addition, the size of the generated bubbles was larger and the frequency of bubble generation was lower (Figure 2. 15). This appears to be a phenomenon in which the formation of bubbles is delayed due to the surface property that boiling is hard to occur even though a superheated layer is sufficiently

accumulated around the heating surface. Conversely, in the case of an artificial cavity exists, it was confirmed that the size of a single bubble is relatively small and the frequency of bubbles is increased. In order to determine which of these two conditions is more similar to the experiment conducted on the conventional heater, the experiment was conducted under the same wall heat flux as in the experiment of Ryu et al. (2014), and the final lift-off diameter of the bubble was compared (Figure 2. 16). As a result, the condition with an artificial cavity showed a lift-off diameter similar to the experiment, and it was concluded that it is similar to the actual boiling phenomenon.

2.4.3 Effect of surface material (Polyimide and copper surface)

The boiling phenomenon depends on the surface properties of the heating surface. As shown in Figure 2. 17, it can be seen that the size of a single bubble is slightly smaller and the frequency is slightly increased on the copper surface than polyimide. This is because the surface of copper is easier to generate bubbles than polyimide with a low surface roughness Ra value. More detailed experimental results are covered in the next chapter.

2.5 Test matrix

The experiments were carried out at a heat flux of 26–66 kW/m² and flow rate of 0.011–0.028 m/s (0.13–0.32 kg/s) to mimic natural convection (Bae et al., 2012). The inlet Reynolds number was between 4280 and 10,890. A stagnant flow condition was not included in the experiment because a stabilized condition could

not be achieved. However, the conditions with flow rates are more realistic as the natural circulation flow rate exists in the cooling water tank in the prototypic passive safety system. The experimental cases were selected only if consecutive single bubbles were generated on the controlled heating area; this satisfied the study objective of investigating the bubble volume and velocity excluding the bubble coalescence while bubbles slide. The test section was at atmospheric pressure and the corresponding saturation temperature. The tests were performed with two locations for the artificial nucleation site: 23° and 45° from the bottom of the heater rod. The experimental conditions are summarised in Table 2. 1 and Table 2. 2.

Table 2. 1 Test matrix for FPCB

Nucleation site angle		23°			45°		
Mass flow rate		0.13 kg/s	0.26 kg/s	0.32 kg/s	0.13 kg/s	0.26 kg/s	0.32 kg/s
Wall heat flux	26 kW/m²	Q26M13A23	Q26M26A23	Q26M32A23	Q26M13A45	Q26M26A45	Q26M32A45
	30 kW/m²	Q30M13A23	Q30M26A23	Q30M32A23	Q30M13A45	Q30M26A45	Q30M32A45
	49 kW/m²	Q49M13A23	Q49M26A23	Q49M32A23	Q49M13A45	Q49M26A45	Q49M32A45
Nucleation site angle		90°			135°		
Mass flow rate		0.13 kg/s	0.26 kg/s	0.32 kg/s	0.13 kg/s	0.26 kg/s	0.32 kg/s
Wall heat flux	26 kW/m²	Q26M13A90	Q26M26A90	Q26M32A90	Q26M13A135	Q26M26A135	Q26M32A135
	30 kW/m²	Q30M13A90	Q30M26A90	Q30M32A90	Q30M13A135	Q30M26A45	Q30M32A45
	49 kW/m²	Q49M13A90	Q49M26A90	Q49M32A90	Q49M13A135	Q49M26A135	Q49M32A135
	66 kW/m²	Q66M13A90	Q66M26A90	Q66M32A90	Q66M13A135	Q66M26A135	Q66M32A135

Only some results are shown due to merging of bubbles

Table 2. 2 Text matrix for copper

Nucleation site angle		23°			45°		
Mass flow rate		0.13 kg/s	0.26 kg/s	0.32 kg/s	0.13 kg/s	0.26 kg/s	0.32 kg/s
Wall heat flux	26 kW/m²	Q26M13A23	Q26M26A23	Q26M32A23	Q26M13A45	Q26M26A45	Q26M32A45
	30 kW/m²	Q30M13A23	Q30M26A23	Q30M32A23	Q30M13A45	Q30M26A45	Q30M32A45
	49 kW/m²	Q49M13A23	Q49M26A23	Q49M32A23	Q49M13A45	Q49M26A45	Q49M32A45
	66 kW/m²	Q66M13A23	Q66M26A23	Q66M32A23	Q66M13A45	Q66M26A45	Q66M32A45
Nucleation site angle		90°			135°		
Mass flow rate		0.13 kg/s	0.26 kg/s	0.32 kg/s	0.13 kg/s	0.26 kg/s	0.32 kg/s
Wall heat flux	26 kW/m²	Q26M13A90	Q26M26A90	Q26M32A90	Q26M13A135	Q26M26A135	Q26M32A135
	30 kW/m²	Q30M13A90	Q30M26A90	Q30M32A90	Q30M13A135	Q30M26A45	Q30M32A45
	49 kW/m²	Q49M13A90	Q49M26A90	Q49M32A90	Q49M13A135	Q49M26A135	Q49M32A135
	66 kW/m²	Q66M13A90	Q66M26A90	Q66M32A90	Q66M13A135	Q66M26A135	Q66M32A135
Nucleation site angle		180°					
Mass flow rate		0.13 kg/s	0.26 kg/s	0.32 kg/s			
Wall heat flux	26 kW/m²	Q26M13A23	Q26M26A23	Q26M32A23			
	30 kW/m²	Q30M13A23	Q30M26A23	Q30M32A23			

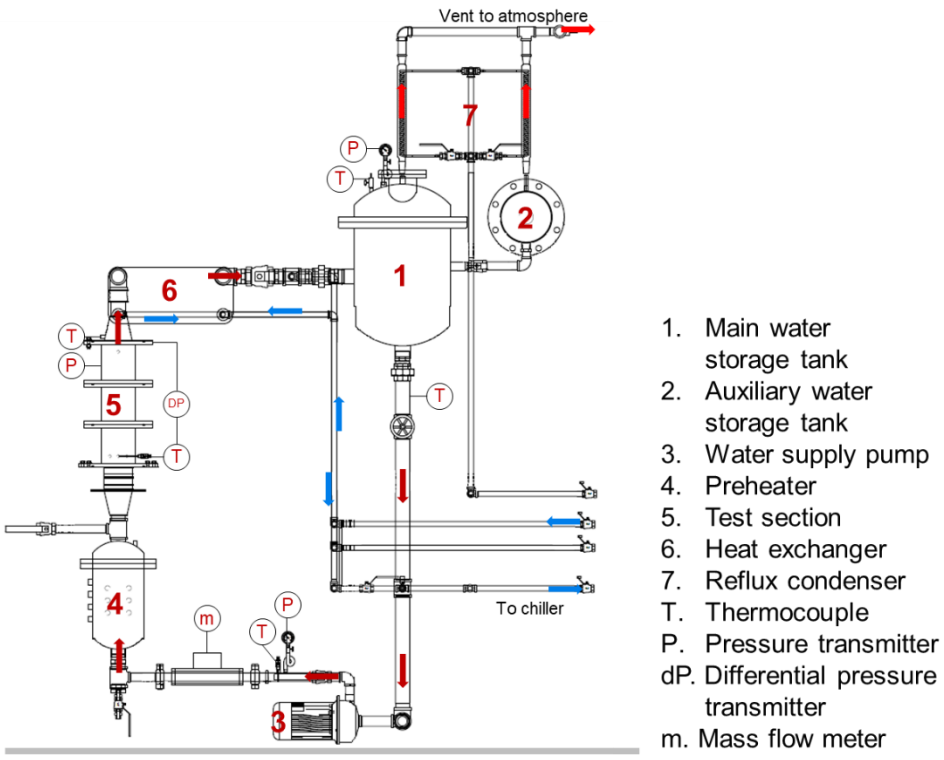

Figure 2. 1 Schematic of the experiment loop.

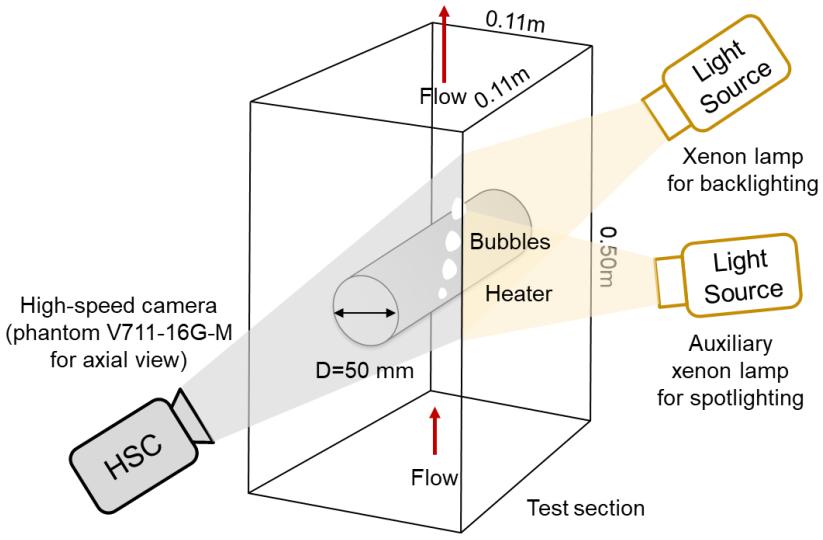

Figure 2. 2 Schematic diagram of the test section and set up for the visualization system.

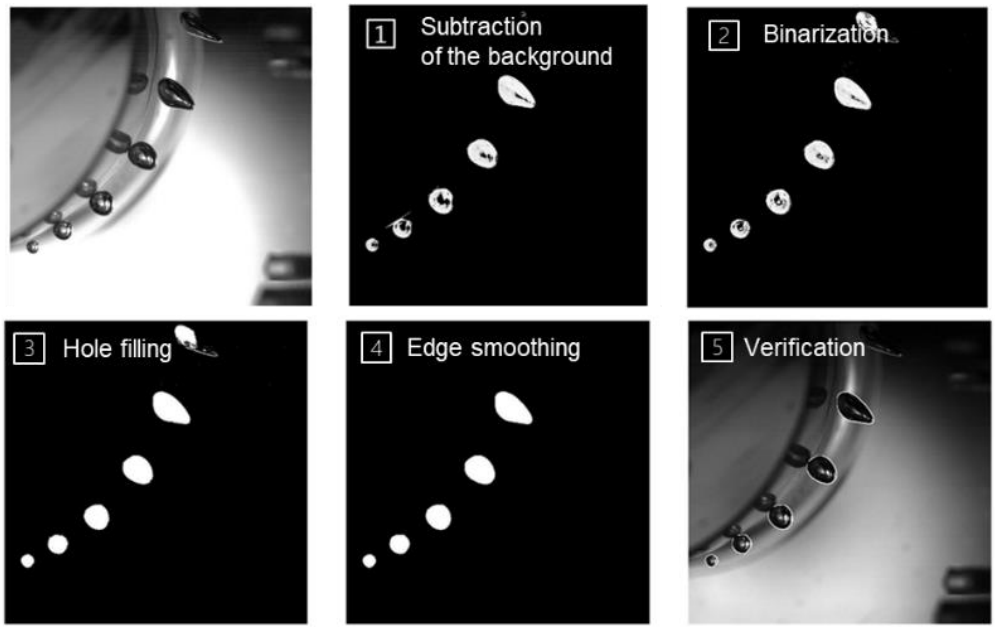

(a)

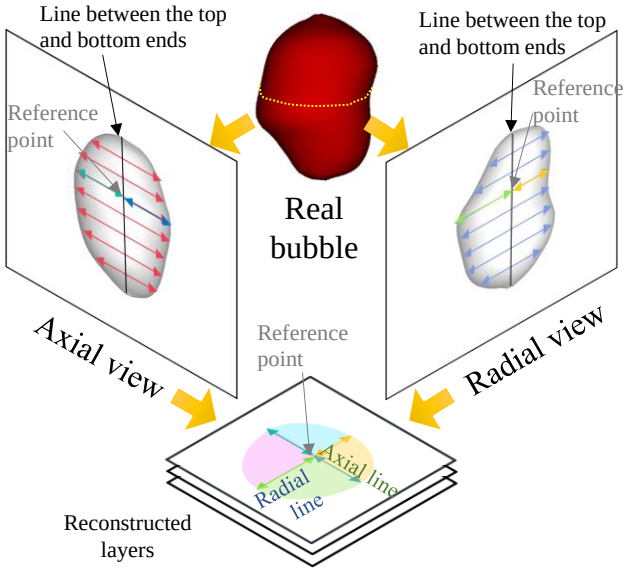

(b)

Figure 2. 3 Image processing procedure and volume reconstruction method: (a) Image processing procedure (b) volume reconstruction method (Kim et al., 2017)

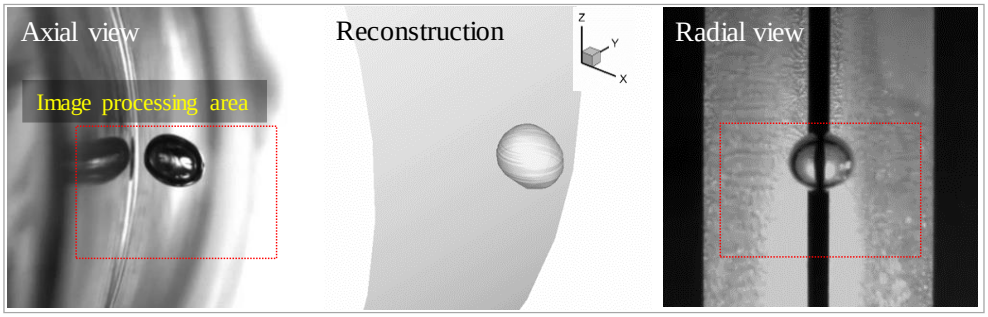

(a)

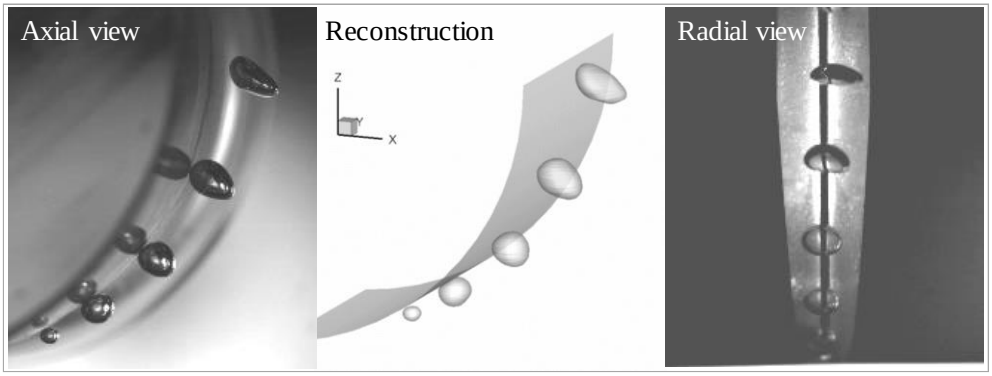

(b)

Figure 2. 4 3D bubble reconstruction results
(a) 90º nucleation site; (b) 23º nucleation site

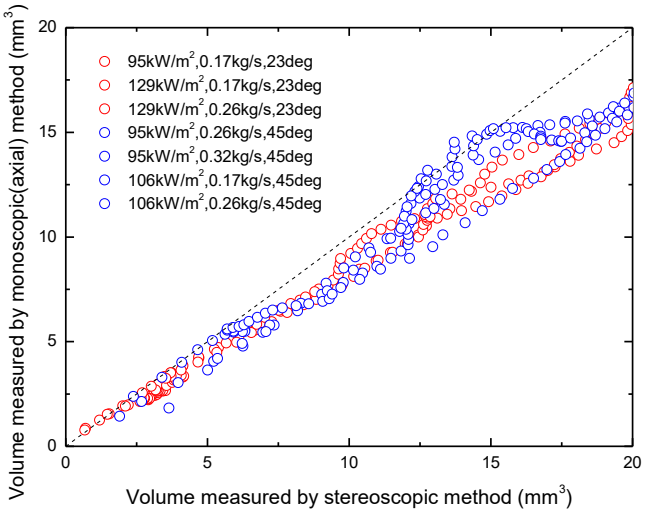

Figure 2. 5 Comparison result of bubble volumes between the monoscopic and stereoscopic method

(a) (b)

Figure 2. 6 Difference in boiling phenomenon according to the thickness of the heater heating part:
(a) conventional cartridge heater, (b) heater used in this study

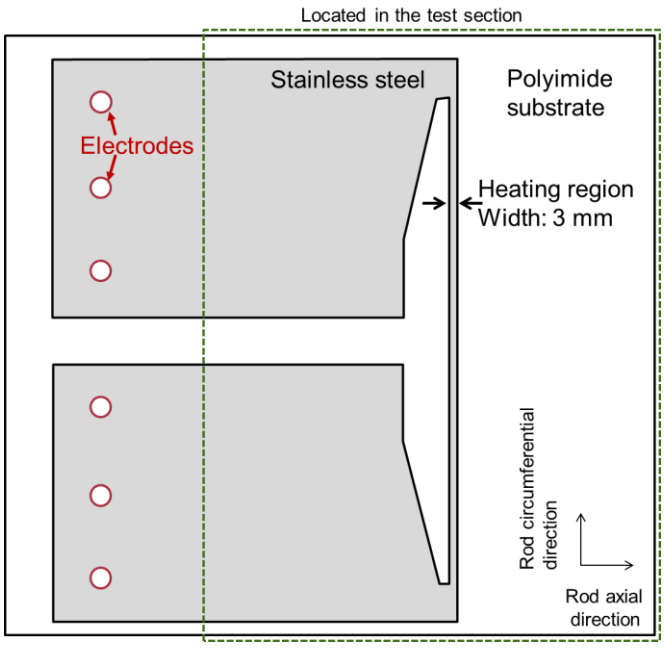

Figure 2. 7 Circuit design of the heater

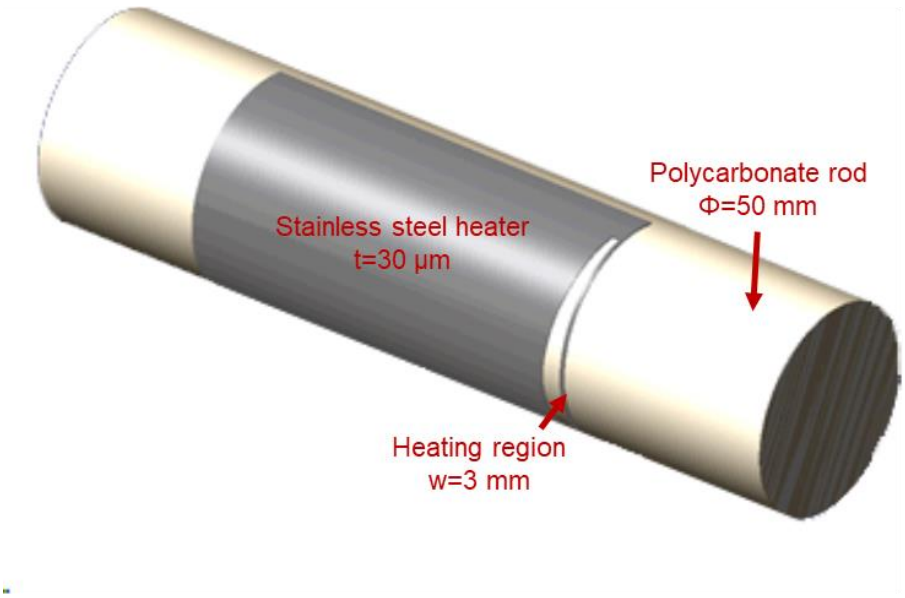

Figure 2. 8 Schematic diagram of the heater attached to the rod

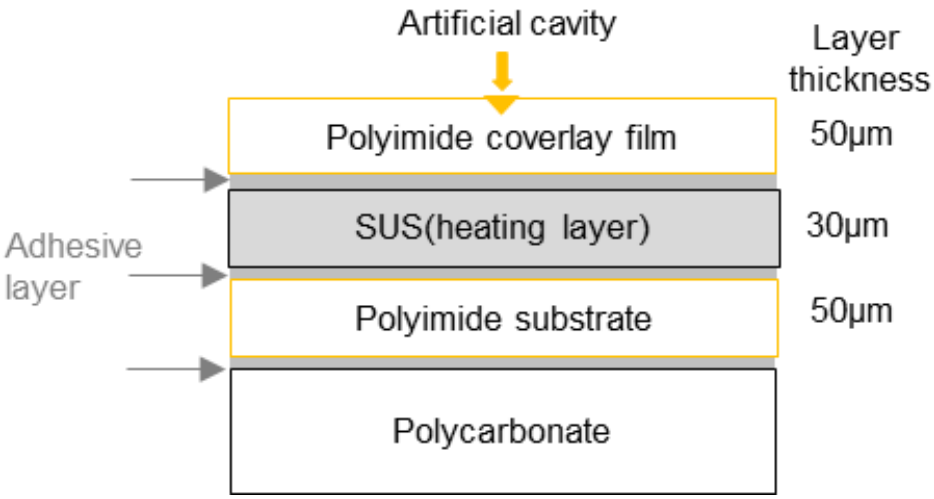

Figure 2. 9 Schematic of the heater layer

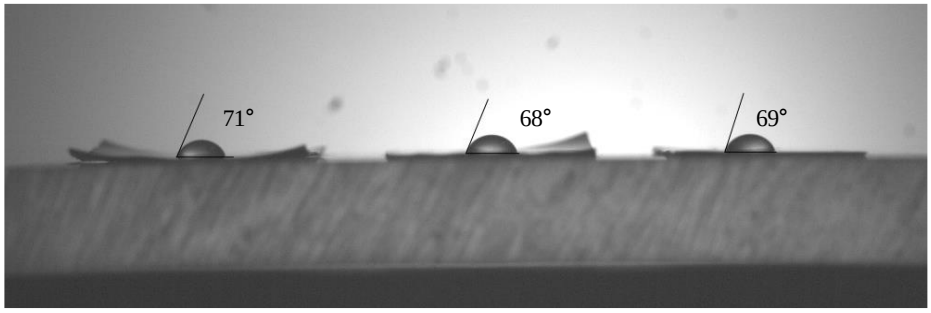

Figure 2. 10 Contact angle experiment (FPCB)

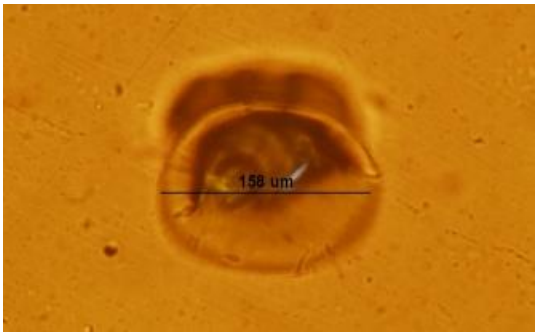

Figure 2. 11 Artificial cavity on the polyimide surface

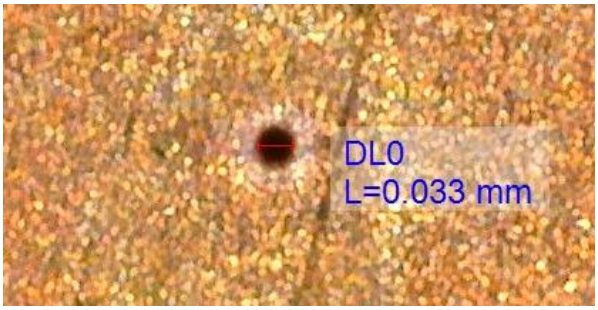

Figure 2. 12 Artificial cavity on the copper surface

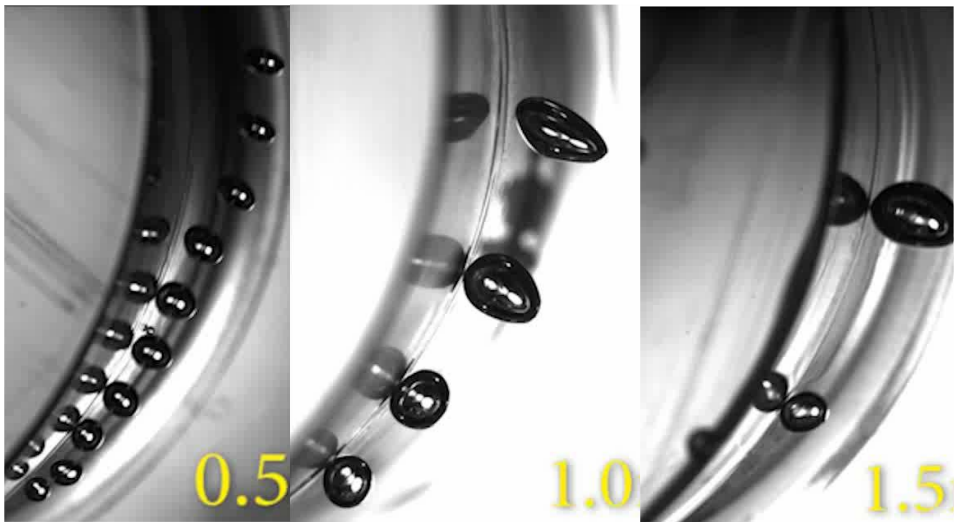

(a) (b) (c)

Figure 2. 13 Difference in boiling phenomenon according to heater heating width:
(a) w=0.5mm, (b) w=1.0mm, (c) w=1.5mm,
(Nucleation site: 45º, heat flux: 106kW/m², inlet velocity: 0.022m/s)

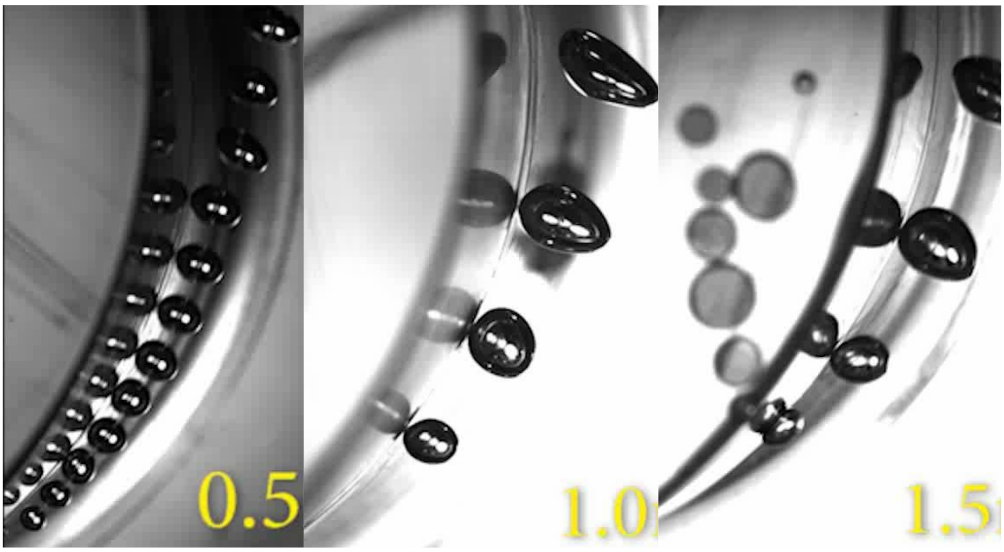

(a) (b) (c)

Figure 2. 14 Difference in boiling phenomenon according to heater heating width:
(a) w=0.5mm, (b) w=1.0mm, (c) w=1.5mm,
(Nucleation site: 45º, heat flux: 129kW/m², inlet velocity: 0.022m/s)

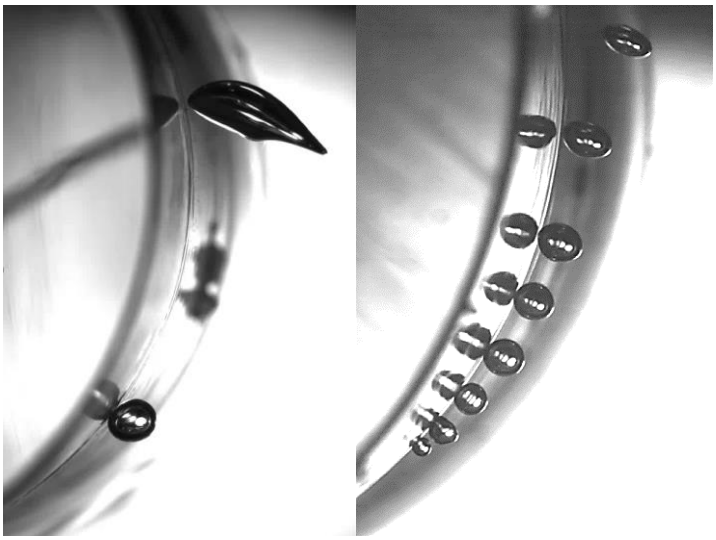

(a) (b)

Figure 2. 15 Difference in boiling phenomena depending on the presence of an artificial cavity: (a) without an artificial cavity, (b) with an artificial cavity (Nucleation site: 45°, heat flux: 66kW/m²)

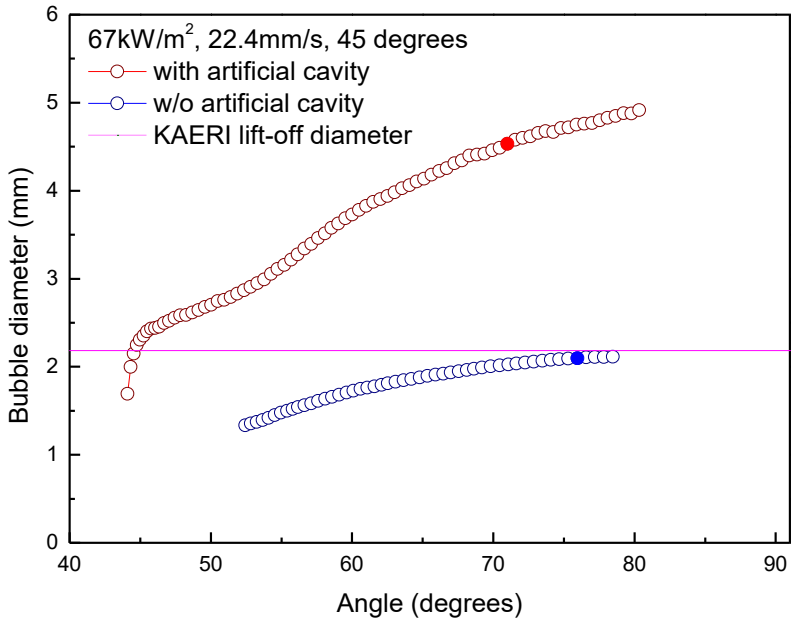

Figure 2. 16 Difference in bubble diameter depending on the presence of an artificial cavity

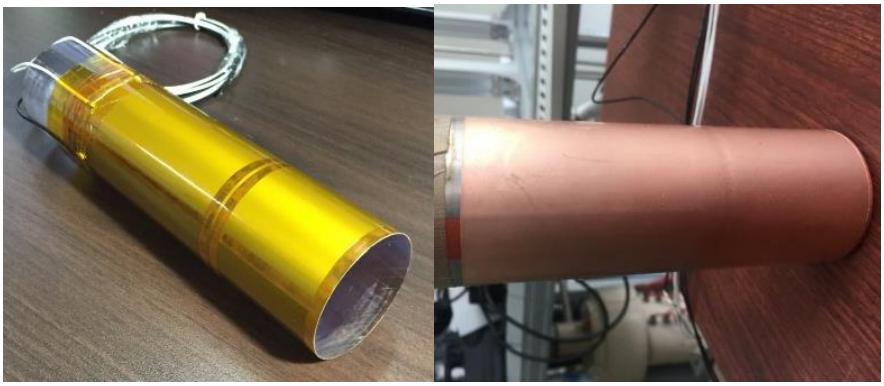

(a) Heater with a different surface material

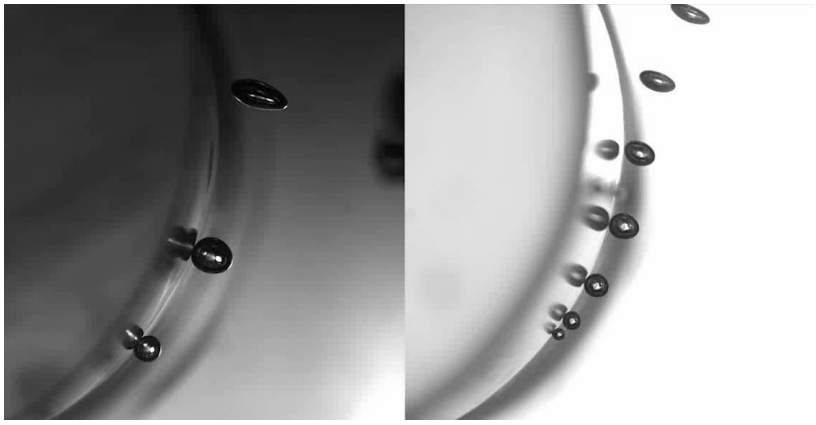

(b) Nucleation site: 45°, heat flux: 26kW/m²

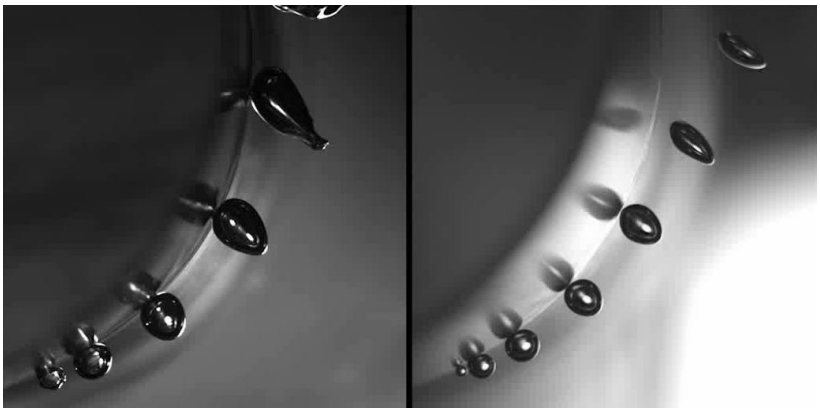

(c) Nucleation site: 23°, heat flux: 66kW/m²

Figure 2. 17 Difference in boiling phenomenon according to surface materials (left: polyimide, right: copper)

Chapter 3

Experimental results and discussions

3.1 Boiling phenomenon on the horizontal tube heater

In the present experiment, the bubble velocity and the bubble volume were measured as the main parameters. Among the experimental data, the cases in which bubble coalescence with the preceding bubble did not occur, were collected with a focus on single bubble behavior. Figure 3. 1 and Figure 3. 2 exemplify the life cycle of a bubble on the tube lower side visualized at two different bubble nucleation sites. The life cycles of a bubble include four stages, the birth, departure, sliding, and lift-off. Figure 3. 1 and Figure 3. 2 are the results observed on a copper surface, and on a polyimide surface respectively. If the bubbles appeared to be completely separated from the heated surface in the images, that moment was defined as the bubble lift-off. Figure 3. 3 and Figure 3. 4 exemplify the life cycles of a bubble on the tube upper side visualized at three different bubble nucleation sites. These cycles include the birth, departure, and lift-off. Unlike the lower part of the tube, bubble lift-offs immediately without a bubble sliding. At the upper and lower side of the tube, the proportions of heat transfer mechanism are different due to the different boiling phenomena at each case.

3.2 Bubble departure frequency

From the point of view of the nucleation site where the bubbles are generated, they have cycles of birth, departure, and waiting. Then, a new bubble is generated with the start of a new cycle. On the nucleation site, the bubble begins to grow after its birth. The bubble grows gradually and when they reach a certain volume, they begin to move (slide) away from the nucleation site of the initial birth, which is called the bubble departure. The time interval from the birth to the departure is called departure time t_d (or growth time t_g). Again, in order to new bubbles to form at the site, sufficient superheated layers must be accumulated around the site. It takes time for bubbles to be generated and grow as energy accumulation is required to supply the latent heat. The time interval between departure and birth of a new bubble is called waiting time t_w.

Bubble (departure) frequency is expressed as the reciprocal of the sum of departure time and waiting time. Bubble frequency represents the number of bubbles produced per unit time at one nucleation site. The expression is as follows.

Bubble departure frequency

$$f = \frac{1}{t_w + t_d} \tag{3.1}$$

Figure 3. 5 shows the bubble frequency (number of bubbles generated per second) with respect to the liquid mass flow rate. In principle, the bubble receives a higher drag force with increased relative velocity and this causes more frequent bubble departure from the surface and the increased bubble departure frequency.

In addition, on the lower side of the horizontal tube, the larger the angle of the nucleation site is, the greater the buoyancy is at the same volume and at the same drag force. This results in the rapid movement of bubbles from the site, increasing the bubble frequency.

Under higher heat flux conditions, bubbles were more frequently generated. Even if the heat flux increases, the departure diameter would be the same as it is determined dominantly by the buoyancy. However, the time that the bubbles reach the departure diameter would be faster. Thus, bubbles more quickly depart from the site, and the bubble frequency increases. Furthermore, the experiment was conducted using a single bubble generation (nucleation) site in this study. Therefore, the amount of liquid enthalpy accumulated from 0 to 45 degrees is larger than the accumulated amount from 0 to 23 degrees. This accumulated liquid enthalpy influences the bubble generation rate. The bubbles generated at 45° grow faster than those at 23° resulting in faster departures and higher frequencies. Besides, the bubbles generated at 45 degrees receive a higher buoyancy force because of the steeper heating surface angle. It may also contribute to the higher departure frequency of the bubbles generated at 45°

3.3 Bubble size parameters

3.3.1 Bubble volume growth

In this study, the bubble volume transient was measured, which is an important variable that affects not only boiling heat transfer but also the amount of single-phase heat transfer, especially from the perspective of mechanical boiling heat

transfer. Figure 3. 6 shows examples of the measured bubble volume and contact length over the time under experimental conditions corresponding to those for Figure 3. 1. The contact length was the length of the wall surface area in contact with the bubble including the microlayer. The bubble volume increased over time as the heat was continuously accumulated. The volume of a bubble increased proportional to the time to the power of 3/2 as it slides. The increasing trend decelerated before lift-off process because the contact area of the bubble was significantly reduced during the lift-off process. The bubbles generated at the 23° nucleation site had a greater sliding length, which increased the bubble volume at lift-off process. The bubbles at 45° showed a slightly greater rate of increase in the volume. This can be explained by the enthalpy in the superheated liquid layer near the nucleation site. The enthalpy of the liquid increased from the bottom end of the heated surface to the nucleation site. Because the 45° case had a greater heating length upstream of the nucleation site, more energy was accumulated in the liquid. Thus, when nucleation started, the bubble in the 45° case had a faster growth rate.

Figure 3. 7 and Figure 3. 8 show the experimental results for the bubble volume under different conditions. The results showed a clear tendency that the wall heat flux effects on the bubble growth rate. The comparison between Figure 3. 7 (a), Figure 3. 7(b), Figure 3. 8 (a) and (b) show that the rate of volume increase was lower at a higher heat flux. Under higher heat flux conditions, bubbles were generated more frequently. This feature decreased the bubble waiting time, which induced a lower liquid enthalpy that accumulated along the bubble sliding path. As a result, this effect lowered the growth rate of the sliding bubble at a higher heat flux.

The effect of the liquid flow rate on the bubble growth rate is rather indistinctive.

As shown in Figure 3. 7 and Figure 3. 8, the volumes of the vapor bubbles increased over time with similar growth rates regardless of the flow rates early in the bubble history. This implies that the liquid velocity near the wall had an insignificant influence on the bubble growth rate during this period. As the bubbles accelerated, the growth rate varied with it slightly.

Depending on the bubble frequency trend along with the liquid flow rate, however, the growth rate trend was changed. When the bubble frequency has an increasing trend along with the mass flow rate (Q30A23 and Q30A45 in Figure 3. 5), the volume increasing rate was decreased with the flow rate. It is a correspondent with the heat flux effect described in the paragraph above. On the other hand, when the wall heat flux is small (Q26A23 and Q26A45 in Figure 3. 5), it was difficult to find a clear tendency between the bubble frequency and the flow rate due to the large fluctuations in the bubble frequency. Under these conditions, the effect of the liquid flow rate showed the indistinctive tendency. These experimental results showed that the bubble growth rate is more dominantly influenced by the bubble frequency than the liquid flow rate.

The increase in bubble size is consistent with the results reported by previous researches such as Plesset and Zwick (1954), Scriven (1959), Zuber (1961), Mikic et al. (1970), Ünal (1976), Yun et al. (2012), Colombo and Fairweather (2015), and Hoang et al. (2016) that the time transient of the bubble diameter (radius) is proportional to the square root of time. The increasing tendency is determined by the sum of heat from the superheated layer around the bubble and heat from the microlayer evaporation. In general, when there is subcooling, condensation heat transfer is additionally considered, but the effect of condensation was excluded because the present experiment was conducted under saturated conditions.

In the experiment of this study, the wall temperature of the heater was not measured. Therefore, the bubble size with respect to time was obtained and the wall temperature can be estimated using an existing bubble size model.

3.3.2 Contact diameter

In this study, the contact diameter, which is the diameter of the area where the bubble and the heating surface contact, was measured. Contact diameter is generally related to the growth of bubbles through the microlayer or the surface tension between the heated surface and the bubbles (Figure 3. 9). A dry spot exists at the center of the inner area of the diameter, and a microlayer is surrounded at the outmost area. But the present visualization method cannot identify the dry-out region and the microlayer region separately. The microlayer is a fine thin film having an average thickness of about 2 nm (Yoo et al., 2018, Gilamn & Baglietto, 2017), and heat of evaporation is transferred to the bubbles through the layer.

The ratio of contact diameter to bubble diameter obtained by the experiment is shown in Figure 3. 10 to Figure 3. 13. Since the contact diameter was photographed in the axial direction only, there are some fluctuations when there are vibrations in the bubble. The contact diameter starts up to 80% at the initial stage of bubble formation, and gradually decreases linearly with time. Finally, becomes zero as the bubbles lift-off from the heating surface.

3.3.3 Departure diameter

The bubble departure diameter is defined as the bubble diameter when the bubble starts to depart from the nucleation site. After the bubbles are generated, the size of the bubbles increases continuously due to heat transferred from the wall and the surrounding superheated layer. When the sum of buoyancy and drag force becomes stronger than the surface tension force, it gradually starts to depart from the formation point.

Figure 3. 14 and Figure 3. 15 show the departure diameter at the polyimide surface and the copper surface, respectively against the mass flow rate. An increase in liquid flow rate causes a decrease in departure diameter. This is because the relative velocity between the bubble and the surrounding fluid increases, so the bubble received the increased drag force. In the experimental results, a decrease in departure diameter was not large because the increase in flow rate was not enough to affect the results sufficiently.

An increase in the angle of the nucleation site results in a smaller departure diameter. This is due to the geometrical characteristics of the horizontal tube. Even with the same volume of bubbles, the buoyancy force according to the angle between the bubbles and the heating surface is different. As the angle increases, the buoyancy force increases and the bubbles can departure from the initial nucleation site even at a smaller size.

The effect of heat flux does not significantly affect the departure diameter. This is because the bubble departure depends largely on the force it receives regardless of the heat. However, when the heat flux is increased, the departure time is shortened because the rate of increase in the diameter of bubbles over time becomes

larger.

3.3.4 Lift-off diameter

In this study, it was experimentally confirmed that the bubbles under the horizontal tube had a life-cycle of birth-sliding-lift off and did not lift-off until reaching about 90 degrees. This is different from lift-off on the vertical or upward surface. On the vertical or upward surface, the bubbles lift-off from the surface when they reach a certain size. Even if the bubble has sufficient force to lift-off from the surface on the lower part of the horizontal tube, the bubble does not lift - off from the surface and continues to grow due to the upper structure that physically suppresses the lift-off of the bubble. When the bubble reaches about 90° without the upper structure, bubble lift-offs from the surface. On the other hand, in the upper part of the horizontal tube, bubbles do not slide and continue to grow at the nucleation site, and when the size of the bubbles reaches a certain size called lift-off diameter, they lift-off from the surface.

Figure 3. 16 and Figure 3. 17, are the experimental results of lift-off diameter obtained from the polyimide surface heater and copper surface heater, respectively. 23~90 degrees correspond to the lower half of the tube, and 90~135 degrees correspond to the upper half of the tube, and the upper half of the tube is characterized by lift-off the surface without sliding.

Theoretically, the lift-off diameter becomes smaller as the mass flow rate increases. The rate of bubble volume increase over time is not changed, but the velocity of bubbles increases, and the time required to lift-off the surface is shortened. This causes the bubbles to lift-off the surface in smaller volumes. In

figures, this trend is well seen within the error range.

In the lower half of the horizontal tube, as the angle of the nucleation site increases, the lift-off diameter decreases. This is because the velocity of bubbles increases and the distance and time to slide is shortened. Even if the volume increase rate of the bubbles through the heating surface and the superheated layer is the same regardless of the nucleation angle, since the buoyancy received from the initial stage is greater due to the angle of nucleation site, the bubbles generated at a larger angle have a greater velocity even in the same volume. In addition, the integration of the velocity with respect to the time becomes the sliding distance, and bubbles generated at a larger angle also have a shorter running distance.

The effect of heat flux is difficult to clearly distinguish. As the heat flux increases, the growth rate of bubble volume increases, also the force that the bubble receives from the beginning increases. As a result, bubble velocity increases. The results are shown in Figure 3. 16 and Figure 3. 17 are those obtained at about 26 to 66 kW/m², and the range of conditions is limited to clearly see the trend. In the case of the polyimide surface shown in Figure 3. 16 and the bubbles generated at 45º, the lift-off diameter slightly decreased as the heat flux increased from 26 kW/m² to 49 kW/m². Conversely, in the 23º case of the copper surface of Figure 3. 17, the heat flux increased gradually from 27 kW/m² to 66 kW/m². However, it is difficult to conclude the tendency, since it showed a tendency within the error range. As the two factors of the effect of volume increase rate and velocity increase effect competed with each other, it is concluded that it can be analyzed only by calculating the exact force according to volume and time.

3.4 Bubble velocity

Figure 3. 18 and Figure 3. 19 show the bubble velocity with respect to the bubble volume. As a bubble slid, its volume increased because of the supplied heat, which caused the bubble to acceleration owing to the buoyancy force. Because of the geometric characteristics of the horizontal tube, where the direction of the surface tangential vector varied continuously, the bubble velocity continuously increased from the bubble generation to lift-off without reaching a specific terminal velocity. Even at the same bubble volume, the bubble velocity varied with the external flow rate. A higher bubble velocity was obtained with a higher liquid flow rate, so it was obviously affected by the drag force.

Meanwhile, the rate of increasing bubble velocity when the bubble volume was less than 0.5 mm^3 was related to the bubble frequency. At a higher bubble frequency (e.g. Q30M32A45 in Figure 3. 19), the rate of increase in the bubble velocity with respect to the volume appeared to be much higher. This phenomenon may be the effect of the preceding bubble on the trailing bubble. At a high bubble frequency, the wake of the preceding bubble may effectively accelerate the trailing bubble and result in a faster bubble velocity. As shown in Figure 3. 5, cases with a high flow rate had a significantly greater bubble frequency than those with low mass flow rates. This implies that the preceding bubble effect needs to be considered to accurately predict the bubble velocity.

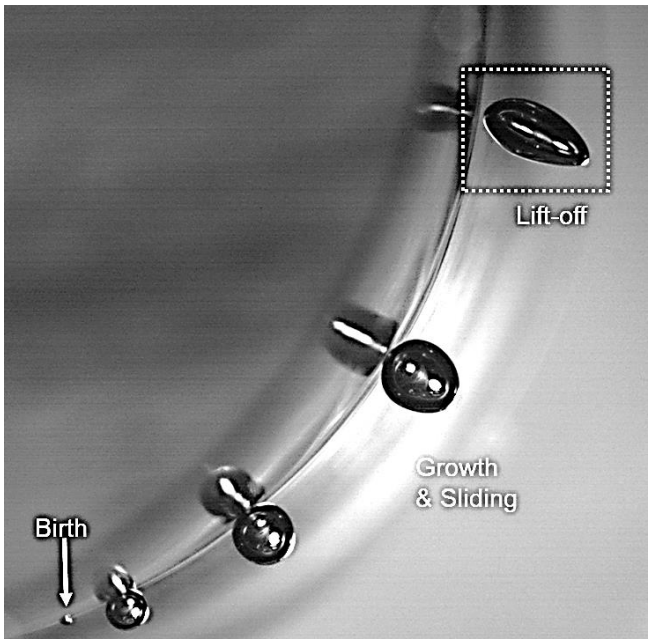

(a)

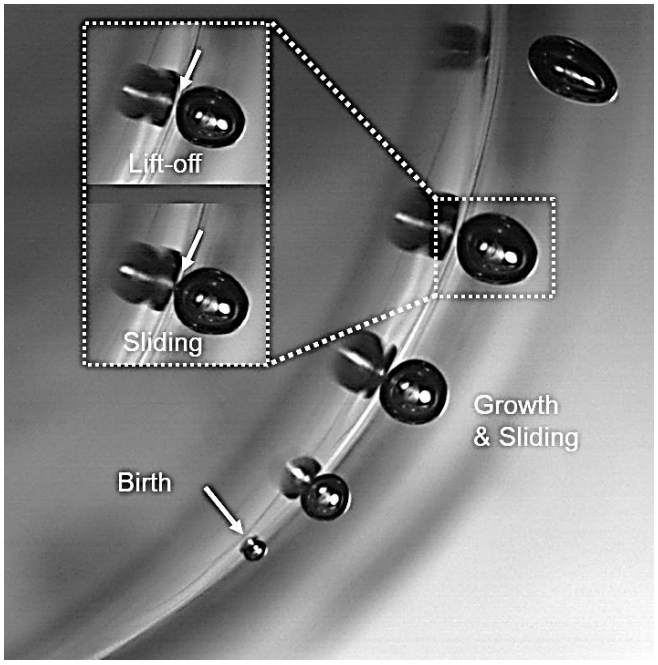

(b)

Figure 3. 1 Life cycles of a bubble on the polyimide tube lower side (a) Q26M13A23 and (b) Q26M13A45.

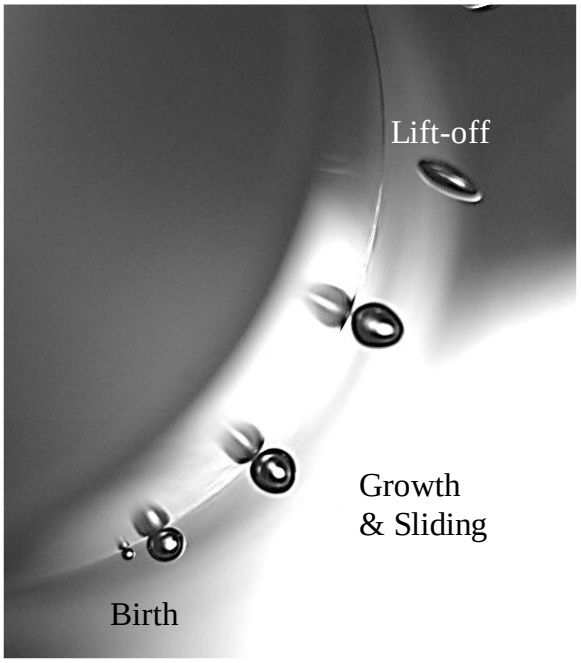

(a)

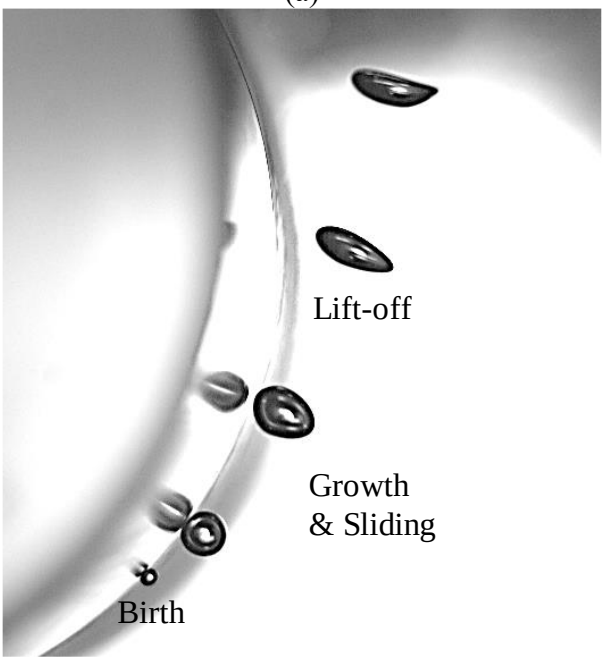

(b)

Figure 3. 2 Life cycles of a bubble on copper tube lower side
(a) Q49M13A23 and (b) Q49M13A45

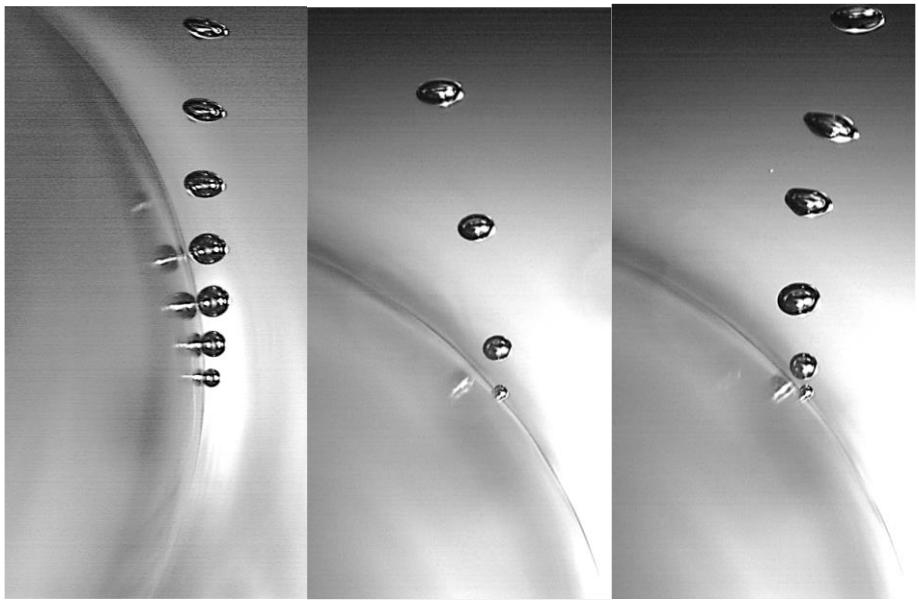

(a) (b) (c)

Figure 3. 3 Life cycles of a bubble on the polyimide tube upper side (a) Q26M13A90 and (b) Q26M13A135 (c) Q30M13A135.

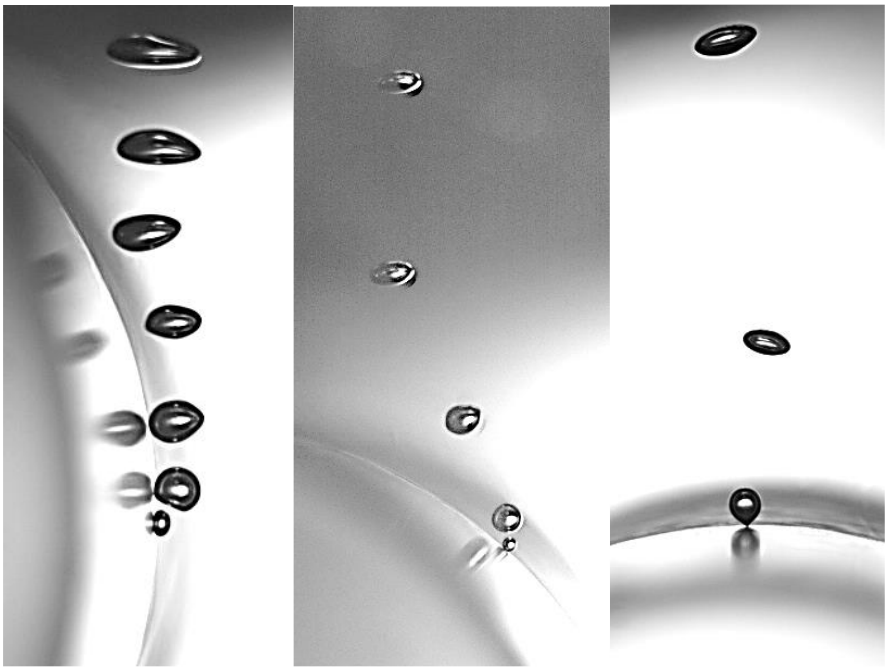

(a) (b) (c)

Figure 3. 4 Life cycles of a bubble on copper tube upper side

(a) Q66M13A90 and (b) Q66M13A135 (c) Q66M13A180.

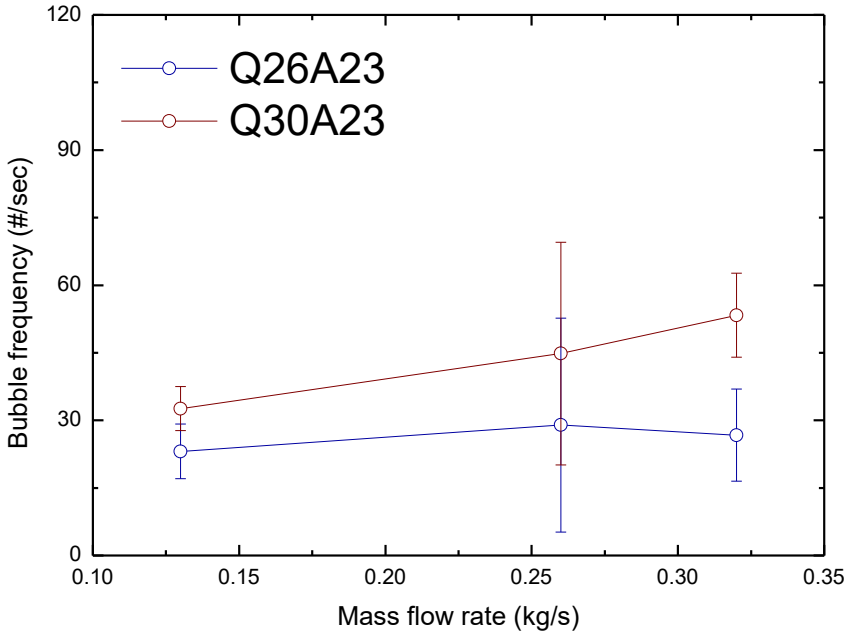

(a)

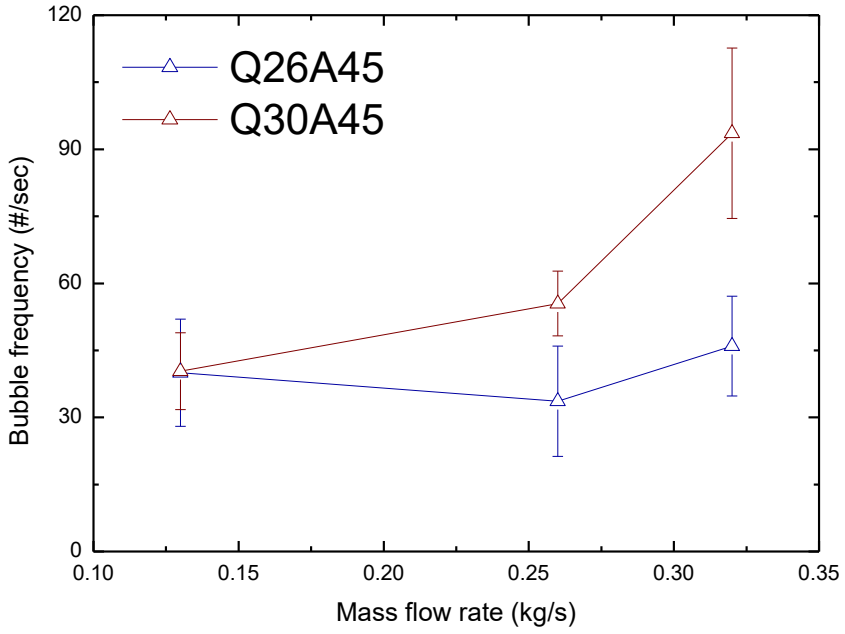

(b)

Figure 3. 5 Bubble frequency by inlet mass flow rate: (a) nucleation site at 23°

and (b) nucleation site at 45°.

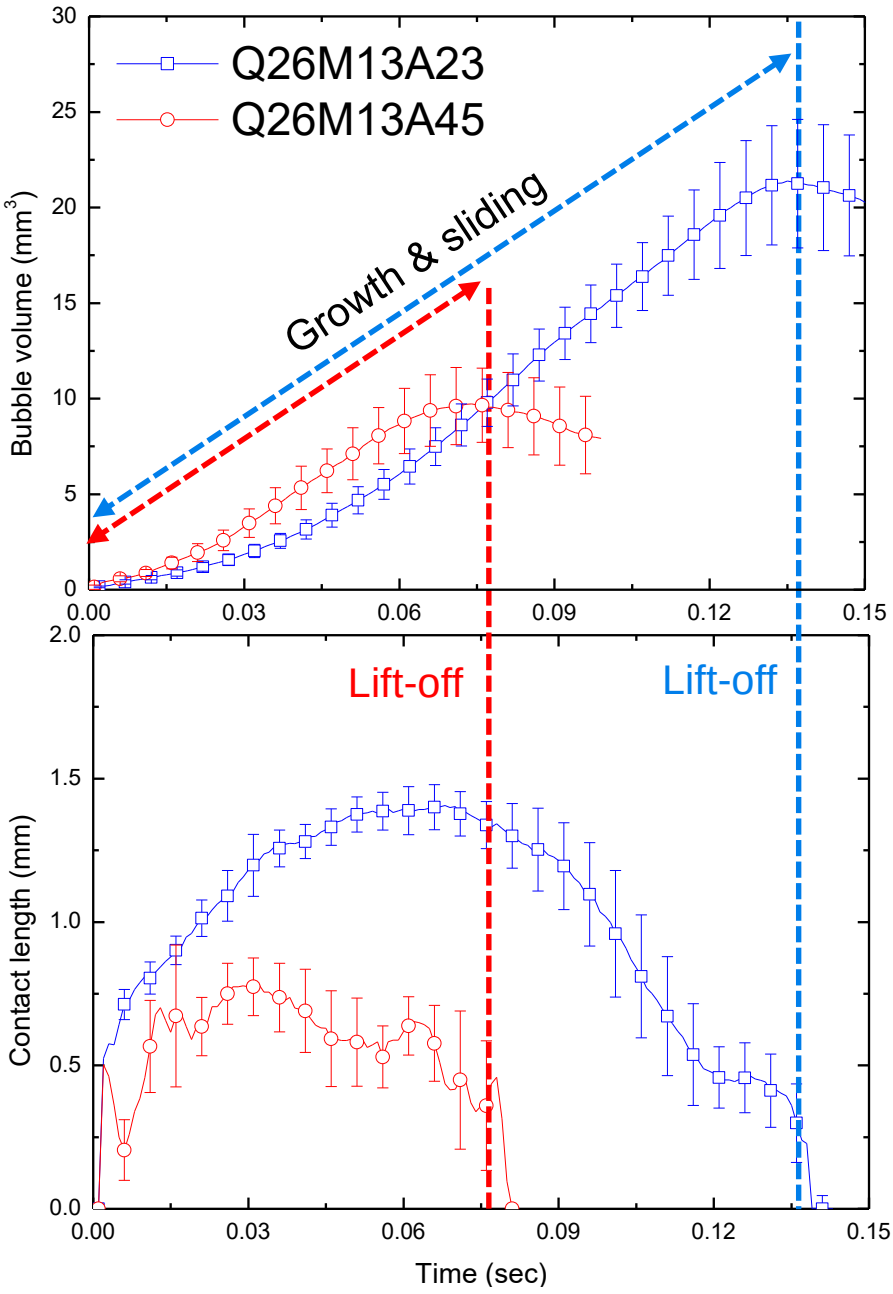

Figure 3. 6 Bubble volume and contact length transient in the bubble life cycle.

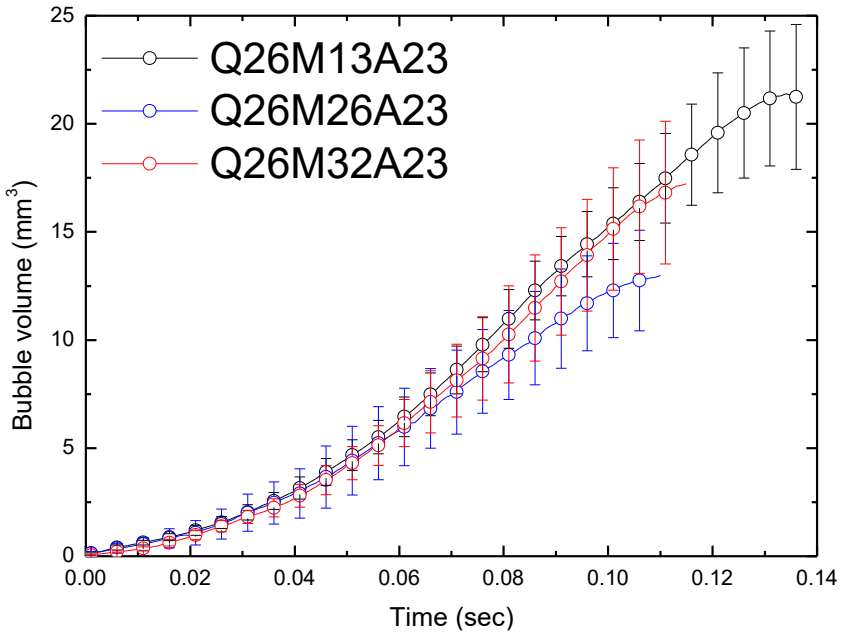

(a)

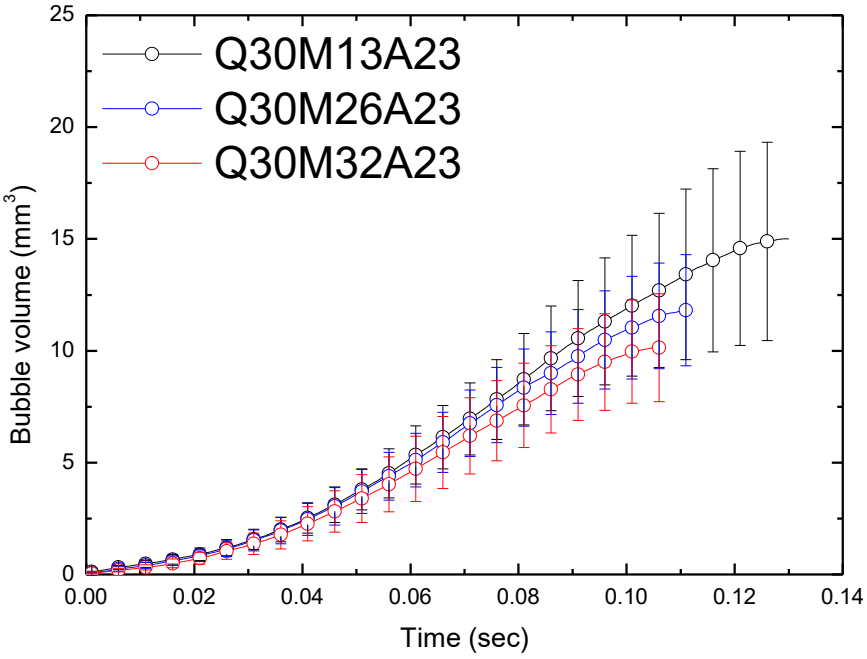

(b)

Figure 3. 7 Experimental results for the bubble volume over time: (a) Q26A23 and (b) Q30A23.

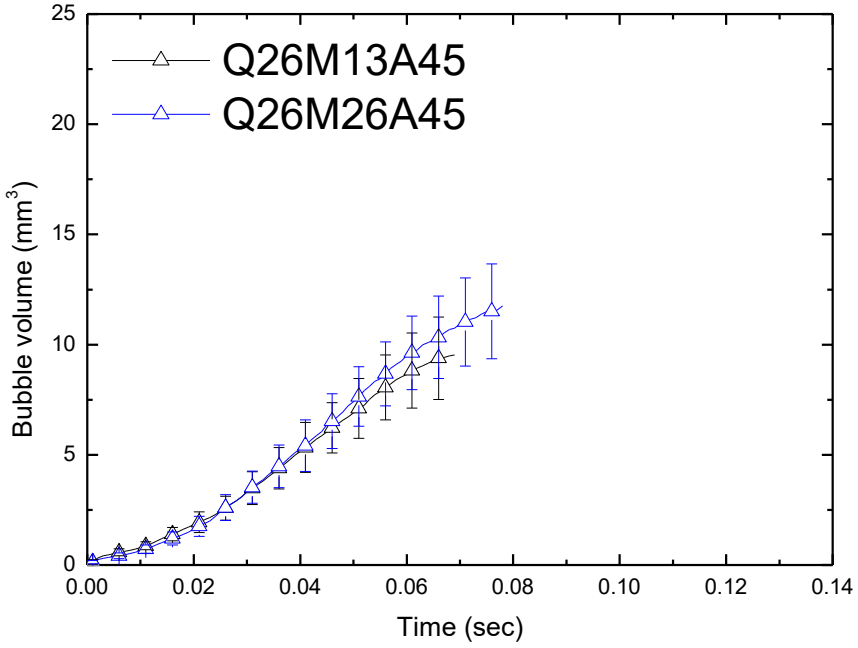

(a)

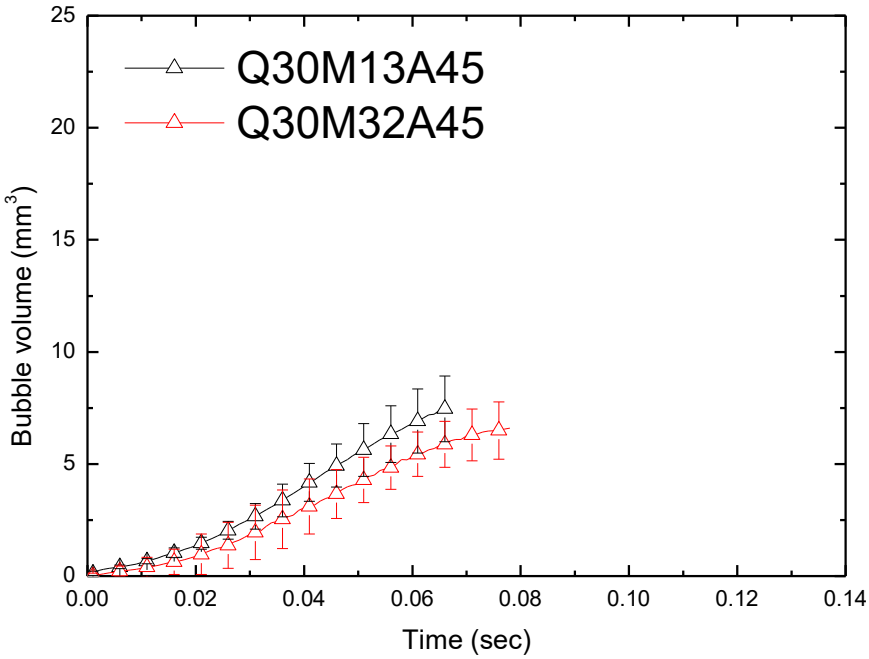

(b)

Figure 3. 8 Experimental results for the bubble volume over time:

(a) Q26A45 and (b) Q30A45.

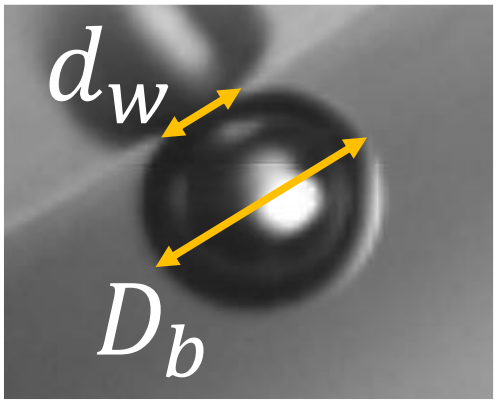

Figure 3. 9 Definition of contact diameter in this study

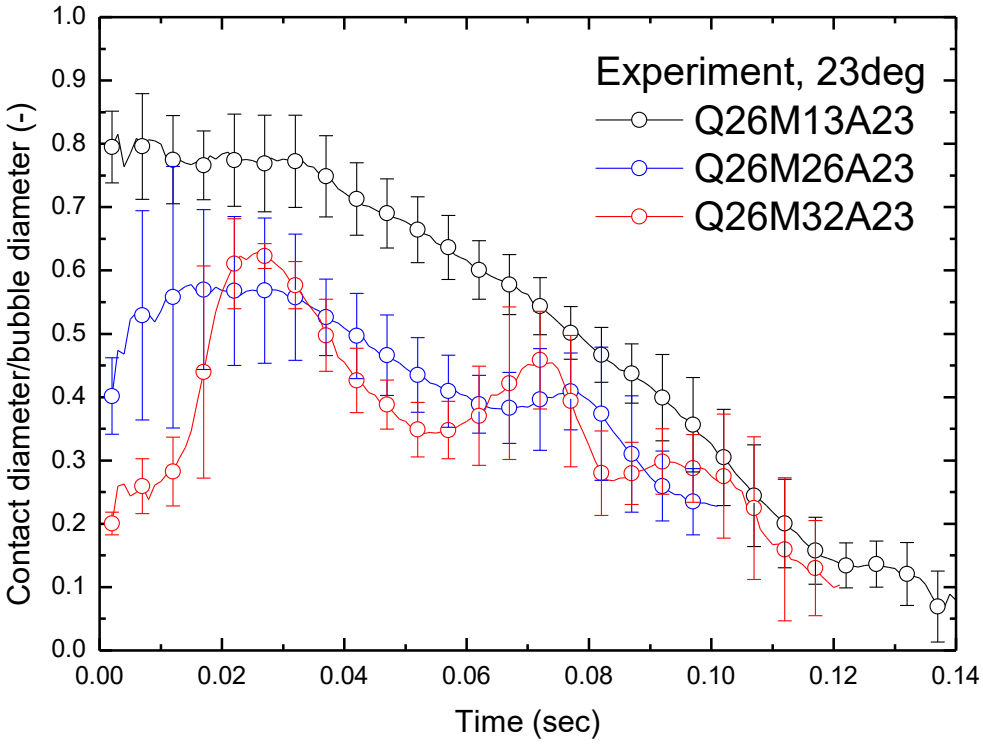

Figure 3. 10 Contact diameter ratio (FPCB, Q23A23)

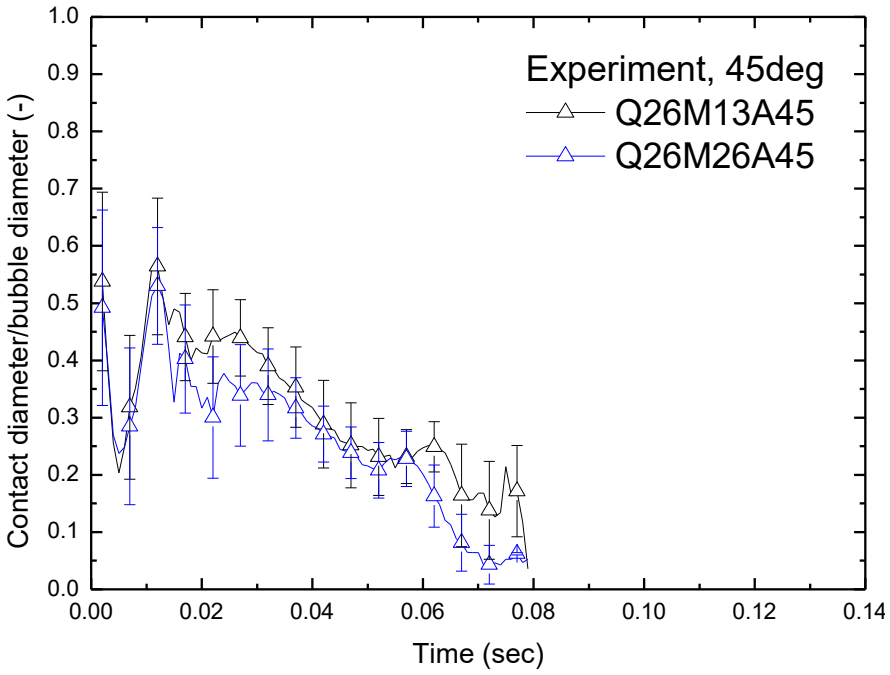

Figure 3. 11 Contact diameter ratio (FPCB, Q23A45)

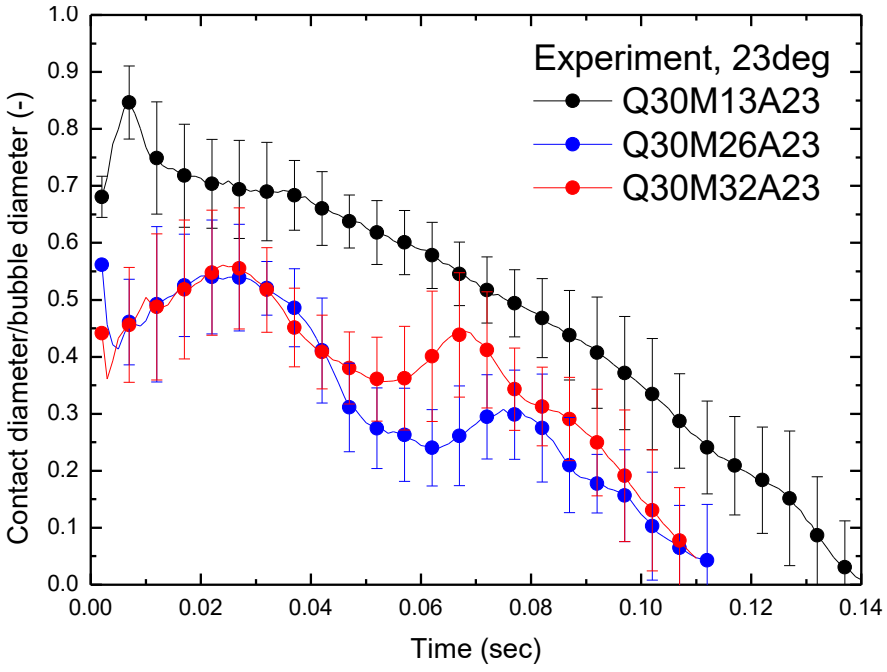

Figure 3. 12 Contact diameter ratio (FPCB, Q30A23)

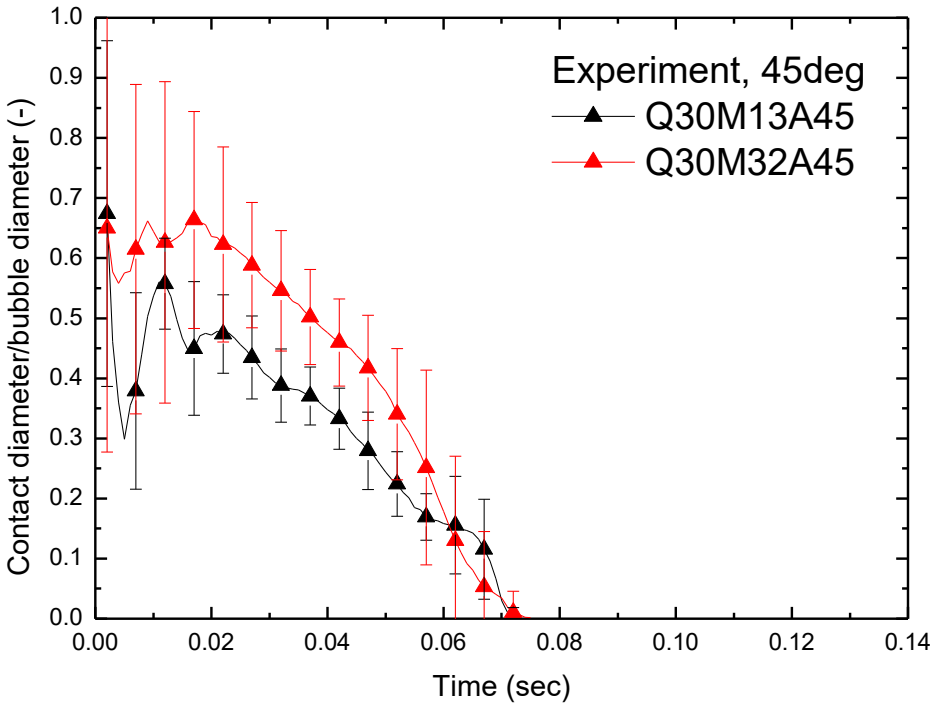

Figure 3. 13 Contact diameter ratio (FPCB, Q30A45)

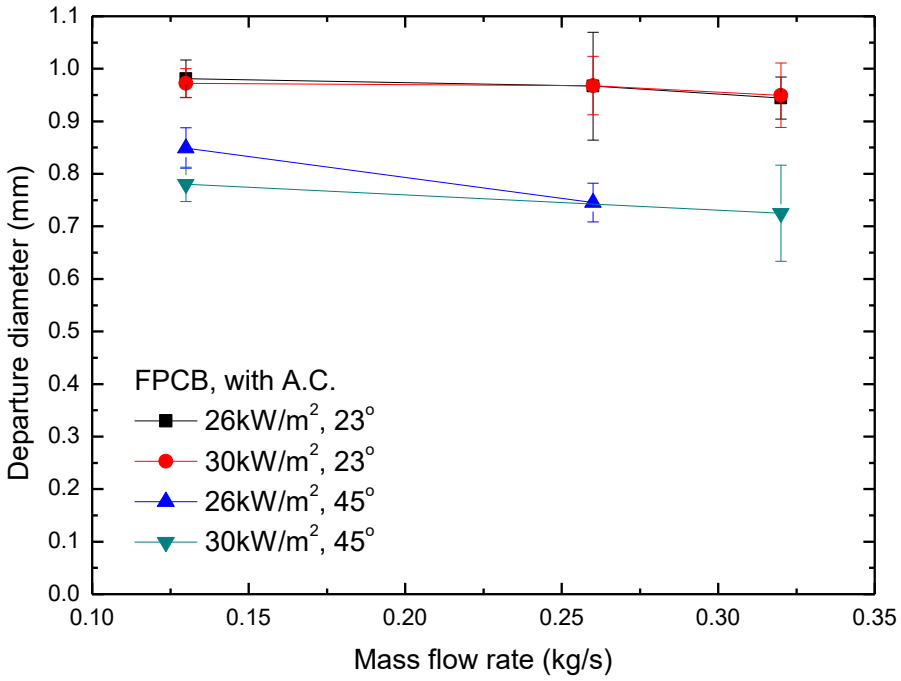

Figure 3. 14 Departure diameter, polyimide surfaced heater

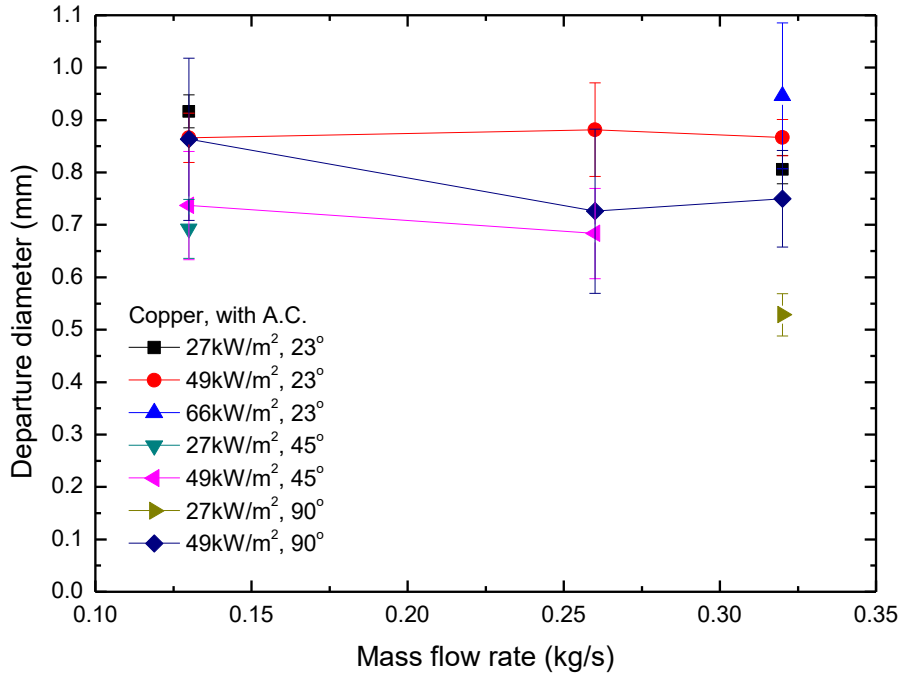

Figure 3. 15 Departure diameter, copper surfaced heater

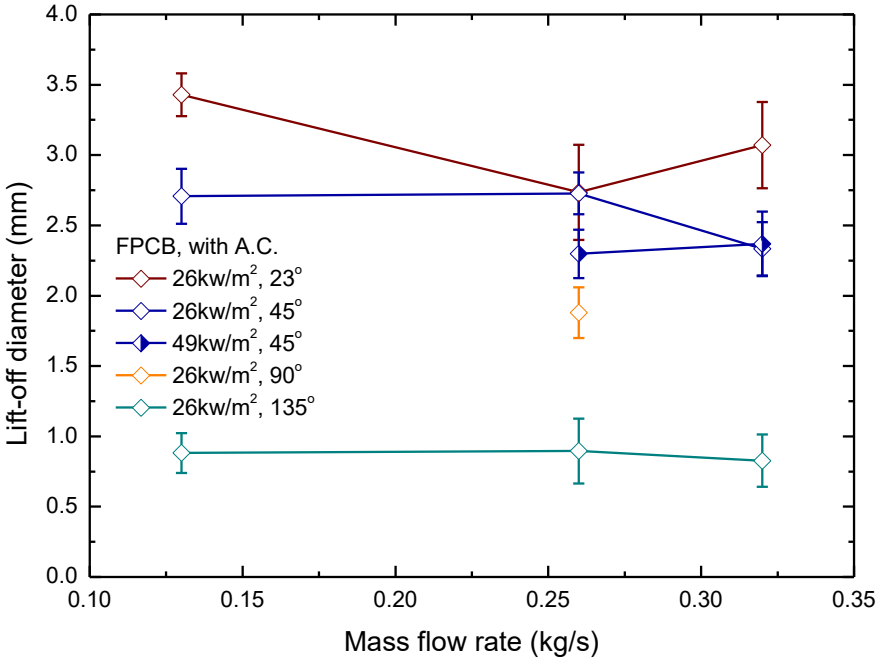

Figure 3. 16 Lift-off diameter, polyimide surfaced heater

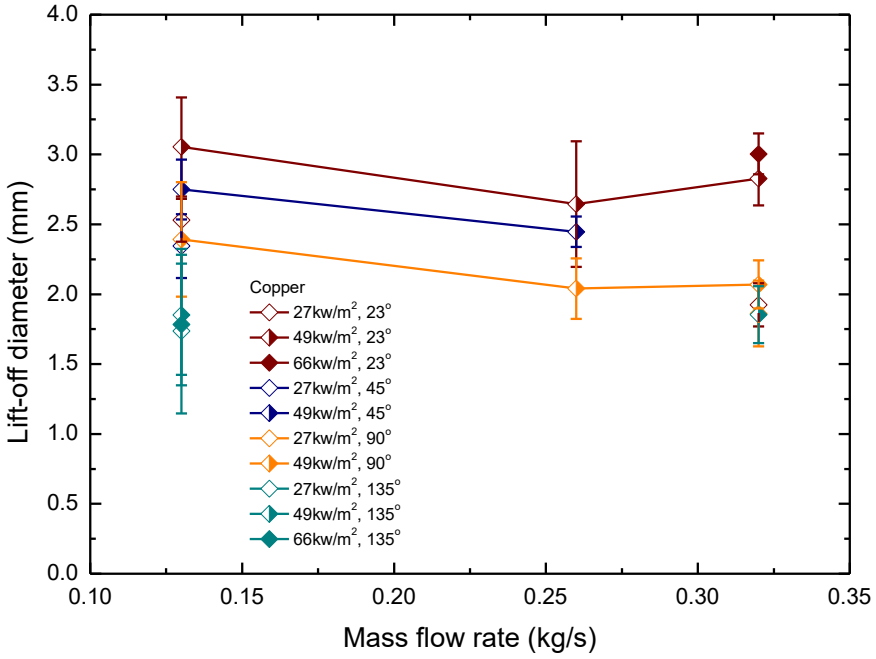

Figure 3. 17 Lift-off diameter, copper surfaced heater

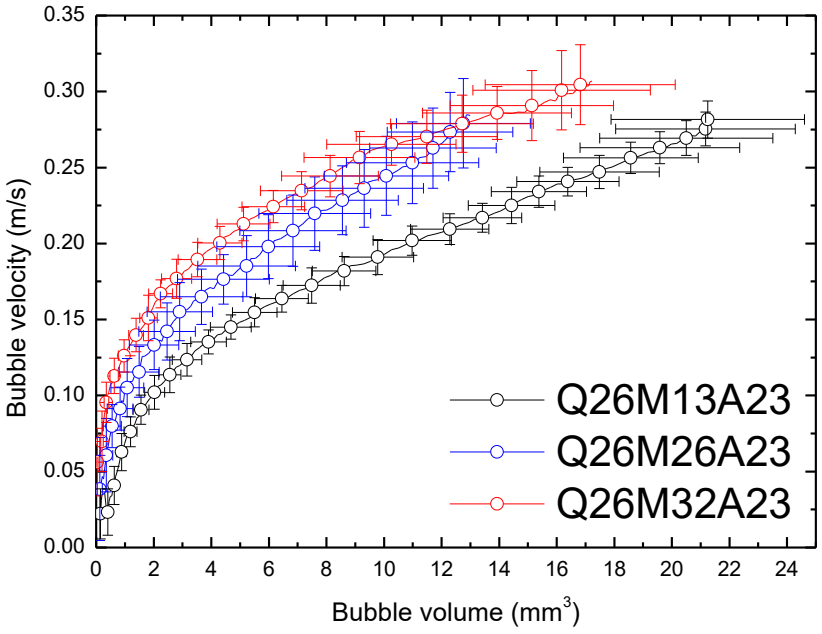

(a)

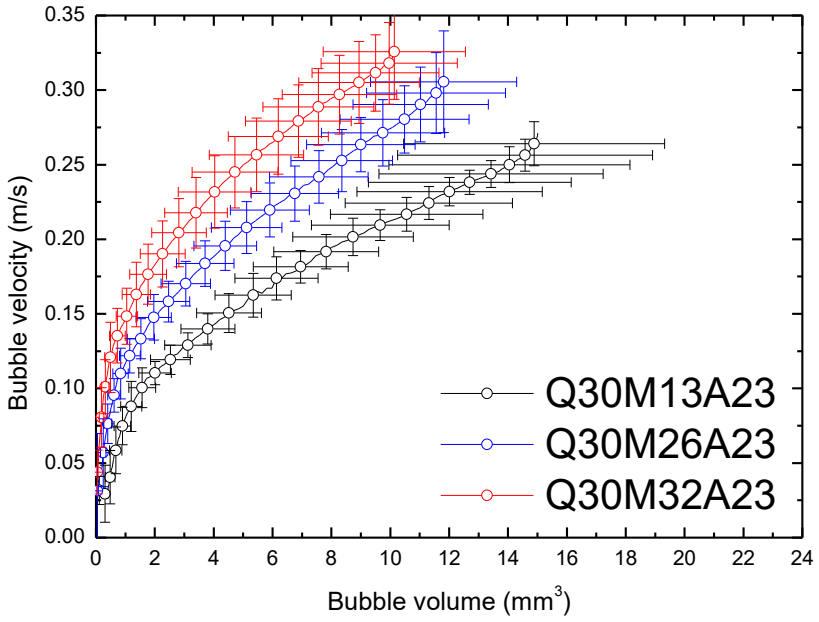

(b)

Figure 3. 18 Experimental results for the bubble velocity by bubble volume: (a) Q26A23 and (b) Q30A23.

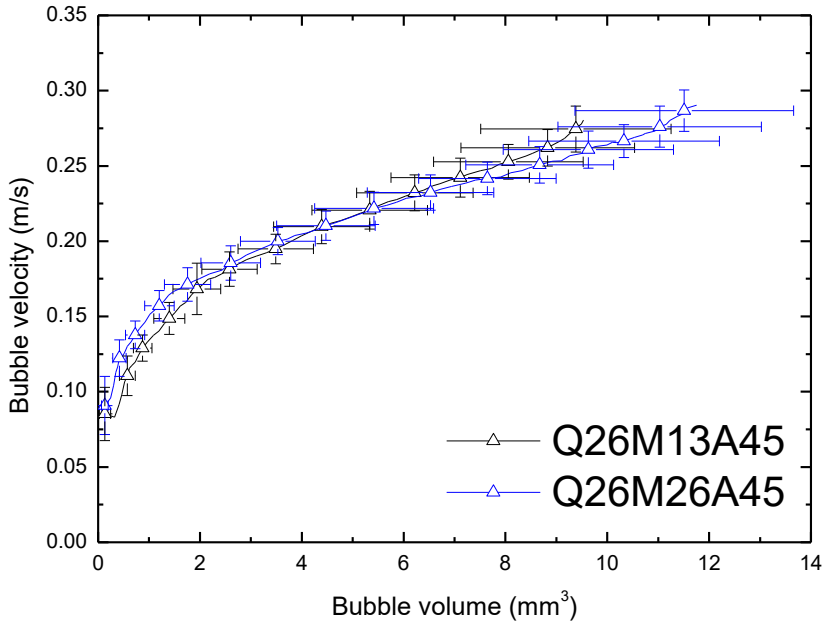

(a)

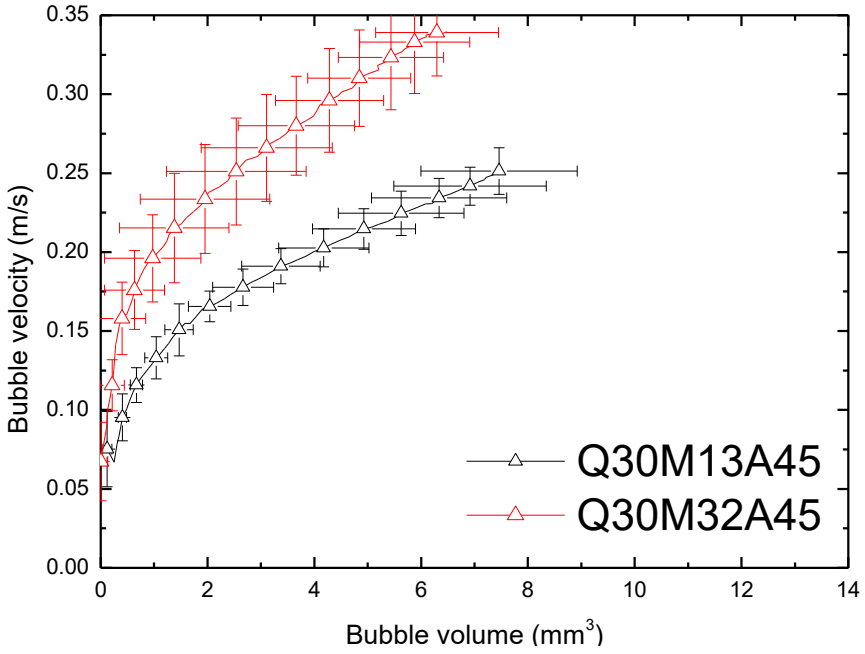

(b)

Figure 3. 19 Experimental results for the bubble velocity by bubble volume: (a) Q26A45 (b) Q30A45.

Chapter 4

Sub-model development and validations

4.1 Development and validation of the mechanistic modified force balance model

4.1.1 Modified force balance model and bubble velocity prediction

Accurate prediction of bubble velocity is very important in mechanistic heat transfer models. In the equations of the heat partitioning model mentioned in equations 1.1 to 1.6, it can be seen that the bubble velocity affects both transient conduction and microlayer evaporation.

The mechanical force balance model is a model that predicts bubble behavior by analyzing forces acting on bubbles and is widely used in predicting bubbles velocity, departure, lift-off, etc. Klauser et al. (1993) first proposed a force balance model and targeted saturated forced convection condition on horizontal plate geometry. Yeoh and Tu (2004) extended Klausner's force balance model to a vertical surface and subcooled boiling at low pressure in a vertical annulus channel. Yun et al. (2012)improved the force balance model to extend its applicability to subcooled boiling at high pressure in a vertical pipe. Recently, Sugrue et al. (2014)

extended the force balance model to various surface orientations. However, further investigation and validation are required in order to extend its applicability to a horizontal tube. Because most of the previous validation works have been conducted with a plate or vertical channel geometries.

In the force balance analyses of previous studies, the bubble velocity was assumed to be the same as the bulk velocity (Gilman & Baglietto, 2017), (Yun et al., 2012) or half of the bulk velocity (Bae et al., 2010). This may be valid if the bulk velocity is significantly greater than the velocity of the bubble. However, this assumption is not appropriate because this study targets natural convection conditions that are close to pool boiling conditions. In the mechanical heat partitioning model, accurately predicting the velocity of bubbles is one of the main factors in the overall heat transfer calculation. Therefore, in this study, a force balance analysis was performed to evaluate the velocity of the bubble and forces acting on it based on the experimental data. Klausner's force balance model was modified to adopt the r–θ coordinate system to accommodate the horizontal tube condition. The bubble acceleration vector of circular motion is expressed as the angular acceleration of r–θ coordinates system, and the circumferential acceleration components in the θ-directions are Eq. (4.1) In this study, the force acting in the θ direction (circumferential direction) was analyzed; only the circumferential velocity of the bubble as it slid along the heater surface was considered. The r-directional force balance analysis was excluded but is described in a previous paper by the co-workers (Kim et al., 2017). The sum of the forces exerted on the bubble in the θ direction is expressed below and includes the buoyancy force, quasi-steady drag force, surface tension force, and added mass (Figure 4. 1, Table 4. 1).

$$F_{tot,\theta} = F_{b\theta} + F_{qs\theta} + F_{s\theta} + F_{am\theta} \quad (4.1)$$

$F_{b\theta}$ is the buoyancy force in the θ direction acting on the bubble. The buoyancy increases with the bubble volume and angle of nucleation site θ_b (i.e. the angle between the surface normal vector and gravitational force).

The quasi-steady drag force $F_{qs\theta}$ is the drag force exerted in the θ direction when the bubble is moving at a velocity different from that of the liquid and is calculated from the relative velocities of the external fluid and bubble. The drag force changes with the bubble configuration, but a spherical bubble shape was assumed to simplify the modeling. Based on this assumption, the bubble cross-sectional area (A) and bubble resistance coefficient (C_D) were determined as listed in Table 4. 1. To evaluate the drag force, the liquid velocity was required. In the force balance analyses of previous studies, the bulk velocity was assumed to be the same as the bulk velocity for the drag force evaluation except when the bubble frequency was greater than a certain criterion. According to the insight obtained in the previous section, the bubble velocity notably increased when the bubble frequency was high in Figure 4. 2. Based on this, it was assumed that the wake effect of the preceding bubble needed to be considered when the gap between two consecutive bubbles was less than twice of bubble diameter ($L_{bubble} \leq 2D_b$). This assumption is based on the local liquid velocity measurement data using PIV for the sliding air bubbles and the experimental observation was explained in the latter section. Figure 4. 3 shows assumptions and experimental results between normalized bubble distance and normalized local liquid velocity. At the same time, the liquid velocity was assumed to be the average of the bulk liquid and sliding bubble for the limiting case when two bubbles make a contact ($L_{bubble} = 0$). A

linear interpolation was applied between the two boundary values, as given below:

$$U_l = \frac{U_{bulk}+U_b}{2} = U_{l,0} \ , \text{ when } L_{bubble} = 0, \quad (4.2)$$

$$U_l = (1 - W) \cdot U_{l,0} + W \cdot U_{bulk}, \ W = L_{bubble}/2D_b, \text{ when } \ 0 < L_{bubble} < 2D_b, \quad (4.3)$$

$$U_l = U_{bulk}, \qquad \text{when } \ L_{bubble} \geq 2D_b, \quad (4.4)$$

where, W is the linear interpolation weight factor

With the above assumption, the acceleration of the bubble by a preceding bubble could be considered in the bubble velocity modeling.

The surface tension force $F_{s\theta}$ in the θ direction generated by the portion of the bubble contacting the wall (Klausner et al., 1993, Kim et al., 2017), the dynamic contact angle, and the area of the bubble contact were required. In this study, the advancing and receding dynamic contact angles (α and β, respectively) were obtained based on visual observation and set to 45° and 30°, respectively.

The added mass force F_{am} was included as a virtual mass because the surrounding fluid needed to be accelerated for the bubble to progress (Thorncroft & Klausner, 2001). In the Eq. Table 4. 1-(4), the first term in Table 4. 1-(4), is the added mass force due to bubble progression, and the second term is the added mass force due to bubble growth as a volume of fluid moved outward following a phase change (Thorncroft & Klausner, 2001). However, the added mass force due to bubble growth was negligible compared to that exerted by the surrounding fluid. Because the heat flux is not so large that the second term due to bubble growth is relatively very small.

By integrating Eq. (4.5) numerically, the bubble acceleration could be evaluated at every time step. The bubble velocity and location could also be evaluated by integrating the acceleration under the initial conditions. The numerical integration of the equation started with the bubble departure volume as the initial condition. When the departure moment was not captured, the diameter and the velocity closest to the bubble departure were set to as the initial conditions. For the integration, the bubble volume, contact diameter, dynamic contact angles, drag coefficient, and liquid velocity were needed. Let $U_{b,i}$ and $\theta_{b,i}$ be the bubble velocity and position, respectively, at the *i*-th time step. Then, $U_{b,i+1}$ and $\theta_{b,i+1}$ are the bubble velocity and position, respectively, at the $(i + 1)$-th time step after a short time duration (Δt). With the explicit Euler numerical integration, the bubble velocity and location angle can be expressed as follows:

$$U_{b,i+1} = U_{b,i} + a\Delta t \ , \ \theta_{b,i+1} = \theta_{b,i} + \frac{U_{b,i}}{R}\Delta t \tag{4.5}$$

The time step for the force balance analysis was set to 0.001 s to maintain consistency with the time span associated with the frame rate of the high-speed video recording. The bubble velocity calculation process is shown in Figure 4. 4. The measured experimental values of the bubble volume were used for each time step. Because the bubble volume had a dominant effect on the force balance analysis, using the volume of bubbles obtained by the experiment is to determine the accuracy of only the bubble velocity prediction model using the correct volume value. After verifying that the bubble velocity model has reasonable predictive performance, the model can be predicted using the existing bubbles growth model.

4.1.2 Local liquid velocity experiment using air bubble in water

In this study, an additional air bubble PIV test was performed to investigate the local liquid velocity around air bubbles and the fluid field changes around the bubble during the sliding. Based on the experimental results, a simplified assumption for the liquid velocity was proposed to calculate the quasi-steady drag of the force balance model.

In this experiment, the surrounding flow velocity field changes due to the sliding of a single air bubble. For this reason, air bubbles were generated sufficiently slowly so that the flow field was not greatly affected by the preceding bubbles. Working fluid was water and the experiments were carried out at a flow rate of 0.12kg/s. The test section was at atmospheric pressure and the ambient temperature. The experimental setup is illustrated in Figure 4. 5.

In the experiment, the bubble images were taken using both PTV and PIV methods; the former for the bubble velocity and the latter for the liquid velocity. The bubble images were analyzed in the same way as the phase separation technique described in the previous chapter, and the location and velocity were analyzed. The continuous light was irradiated for the PIV and fluorescent particles were mixed into the fluid.

A typical result is shown in Figure 4. 6. In this case, the fluorescent particles emit light of a higher frequency by receiving the laser light, and a high pass filter is installed in front of a high-speed camera. Through this, wavelengths other than laser light reflected by the fluorescent particles were blocked to increase the accuracy of PIV analysis. For flow field analysis, Insight 4G, a commercial PIV software, was used. The PIV analysis results are shown in Figure 4. 6 (c).

Figure 4. 7 shows the local liquid velocity over time measured at a specific location, indicated by a white dot where the maximum liquid velocity appears. As the bubble passed through this point, it can be seen that the local liquid velocity was affected. Initially, the velocity of the local liquid maintains the bulk velocity and is not affected by bubbles (Figure 4. 7 ①). However, as the bubble approached the sampling point, the liquid in the measurement section began to accelerate (Figure 4. 7 ②), and immediately after the bubble passed, the local liquid velocity at the position reached its maximum value, which was almost the same as the bubble velocity (Figure 4. 7 ④). Then, as the bubble moved away and over time, the flow velocity at the measuring point was reduced to its original bulk velocity (Figure 4. 7 ⑦). This change in local liquid velocity was repeated periodically as the trailing bubble passes.

It should be noted that the liquid velocity right behind the bubble was close to the sliding bubble velocity at the center location of the bubble. If there are no bubbles, the flow velocity profile starts from zero on the heater surface and increased to the bulk flow velocity as the distance to the rod surface increases. If bubbles exist, however, the liquid velocity profile approaches the bubble velocity and then decreases to the bulk velocity (the bubble velocity is faster than the bulk velocity for most of the time except at the very beginning of initial bubble generation under the experimental conditions of this study). Previous studies that did not consider the effect of the wake induced by a preceding bubble mainly used the bulk flow velocity or the local velocity estimated by the wall function in the calculation of drag force acting on bubbles. However, this study confirmed that the local liquid velocity could change up to the bubble velocity according to the wake of the bubble.

Based on this observation, it was assumed that the trailing bubble sliding continuously with the preceding bubble has an average value of the bubble velocity and the bulk flow velocity. The maximum distance affected by the preceding bubble was assumed to be twice the bubble diameter and was assumed to decrease linearly as the distance between bubbles increases.

4.1.3 Validation of suggested velocity prediction model

The force balance model described in the previous section was used to predict the bubble velocity in the θ direction. Figure 4. 8 ~ Figure 4. 11 compares the experimental values for the bubble velocity and the values obtained with the force balance. The experimental results showed that the bubbles accelerated rapidly within a short time after their departure, and the increase in the velocity gradually decelerated as the bubbles slid along the heater wall. Before reaching terminal velocity, the bubbles lifted off the heated surface. This trend was attributed to the continuously changing bubble volume because of evaporation and the varying angle between the gravitational force and wall due to the horizontal tube geometry. The bubble sliding velocity predicted by the force balance model qualitatively reproduced this tendency well. Figure 4. 12 and Figure 4. 13 compares the predicted bubble sliding velocity with and without the liquid velocity correction from Eq. (4.2) to (4.4) at relatively high bubble frequencies. The force balance model consistently underestimated the bubble velocity without the correction. This clarifies that the local liquid velocity correction is needed to consider the wake generated by the preceding bubble. As shown in Figure 4. 14, the model predicted the bubble velocity within an error of about ±14% (2sigma) after the correction. In addition, the result

of calculation using only the most dominant forces, buoyancy, and drag, excluding surface tension by simplifying the force balance model, is shown in Figure 4. 15. In this case, the force acting in the negative direction disappeared, and it was confirmed that the velocity was predicted by about +7% over the entire case compared to the case where all the forces were used.

Figure 4. 16 and Figure 4. 17 displays the magnitude of each force obtained from the force balance analysis for two cases. The dominant forces turned out to be the buoyancy, quasi-steady drag and added mass forces. In the results, the buoyancy force grew rapidly over time because of the increases in the bubble volume and angle of the wall, which increased the gravitational force as the bubble slid. Throughout the period during which bubbles were generated and lifted off, the buoyancy was considered to be the only significant positive directional force in the advancing direction. Because the velocity difference between the bubble and liquid increased with the bubble velocity, the quasi-steady drag increased accordingly. This force acted in the opposite direction of the bubble advancement. At the beginning of the bubble cycle, the magnitude of this force was relatively small, but it occupied most of the opposite directional force as the bubble accelerated. The added mass force acted to decelerate the bubble in the opposite of the sliding direction. It took up 20%–40% of the opposite directional force during the cycle. The surface tension force initially accounted for about 60% of the opposite directional force, but the proportion became relatively small as the bubbles grew and accelerated. This analysis showed that the surface tension force in the θ direction did not have a significant influence on the predicted sliding bubble velocity.

The above force analysis showed that the balance between the drag and

gravitational forces played a major role in determining the bubble sliding velocity. The balance between inertia forces such as the drag force and the gravitational force can be represented in the dimensionless form with the Froude number. Thus, the experimental data and force balance analysis results are plotted in Figure 4. 18 with the local Froude number defined as follows:

$$Fr_\theta = \frac{U_{b,\theta} - U_{l,\theta}}{\sqrt{g \cdot r_{b,\theta}}} \tag{4.6}$$

where θ is the circumferential location of the bubble. The liquid velocity in Eq. (4.2) to (4.4) was applied to consider the liquid acceleration from the preceding bubble. The Froude number showed a sharp increase immediately after bubble formation. After the bubble departed, the increasing trend decelerated and instead increased rather linearly. The Froude number curves of all cases converged approximately to a single line regardless of the bubble generation location, heat flux, and bulk liquid flow rate. On a horizontal tube surface, instead of reaching the terminal velocity, the sliding bubble velocity seemed to increase according to constant linear inertia–buoyancy force ratio (Fr). The bubbles continued to increase in radius (or volume) as they slid, which resulted in a larger denominator. Also, bubble velocity continued to increase because the bubble continuously accelerated by θ directional net force (always positive in these experimental conditions), which resulted in a larger numerator. Therefore, the force ratio was non-dimensionalized by the Froude number which contains the bubble velocity and bubble radius. This analysis showed that the sliding bubble velocity correlates well with the bubble location when it is non-dimensionalized with a form of Fr and can be applied as a representative dimensionless number to correlate to the sliding velocity in the heat

partitioning model.

4.2 Closure of bubble growth model

Accurate prediction of bubble volume is very important in mechanistic heat transfer models. As with the bubble velocity, it can be seen that the bubble size also affects both transient conduction and microlayer evaporation in the equations of the heat partitioning models mentioned in equations 1.1 to 1.6.

Bubble growth in the horizontal tube is in principle not different from that in the vertical and horizontal planes (Figure 1. 3). This is because the bubble growth is caused by heat transfer at the wall surface and heat transfer at the superheated layer near the wall, and the formation of the wall and superheated layer in the horizontal tube is not different from other geometry. Therefore, compared the experimental results with the existing models developed on other geometry.

Representative existing bubble growth models include Zuber (1961), Yoo (2018), and Colombo (2015), and Sateesh uses Benjamin and Balakrsishnan's (1996) formulas in his heat partitioning model. Each model is as follows.

Zuber (1961)

$$R(t) = \frac{2bc_{p,l}\rho_l(T_{wall}-T_{sat})}{h_{fg}\rho_v}\sqrt{\frac{\alpha_l}{\pi}t} \tag{4.7}$$

Benjamin & Balakrishnan (1996)

$$R(t) = 0.775\left[\left(\frac{g}{{\nu_l}^2}\right)\left(\frac{\sigma}{\rho_l g}\right)^{1.5}\right]^{0.135}\sqrt{\frac{k_l(T_{wall}-T_{sat})}{h_{fg}\rho_v}t} \tag{4.8}$$

Yoo et al. (2018)

$$R(t) = \left[c_{p,l}\rho_l \sqrt{\frac{k_s\rho_s c_s}{k_l\rho_l c_{p,l}}} \mathrm{Pr}^{-0.5} \sqrt{\alpha_l} \left\{ 1.22 \left(\sqrt{\frac{k_s\rho_s c_s}{k_l\rho_l c_{p,l}}} \right)^{-0.79} \cdot \exp(-0.204Ja \right) \right\} + \frac{2bk_l}{\sqrt{\pi\alpha_l}} \right] \frac{(T_{wall}-T_{sat})}{h_{fg}\rho_v} \sqrt{t} \quad (4.9)$$

Zuber's model was derived from bubble growth in a completely enclosed with a superheated layer. Zuber's model has been extensively validated and used by many researchers for a long time. In subsequent studies, evaporation and condensation by microlayer were considered in addition to Zuber's model. Recently, Yoo et al. proposed an equation that reflected all three principles, and experimentally validated the subcooling to 13.5K in water and refrigerants.

Existing bubble size models are commonly proportional to 1/2 of the time. The results of the experiments were also proportional to the 1/2 power of time, the same as existing models. But the wall temperature of the heating surface has not been measured in this experiment and the heat transfer amount may be different due to narrow heating width, so the feasibility of using an existing model was confirmed.

In order to confirm the feasibility, two different equations were used to derive the wall temperature of the heating surface. The first is in terms of the bubble radius model, which is the relationship between wall temperature and bubble growth. Since the experiment was conducted under saturation conditions, the unknown is the bubble radius and wall temperature. In this study, bubble growth over time was measured through experiments. Therefore, wall temperature, which is an unknown, can be obtained by the bubble radius equation.

In addition, in the experiment, bubbles were continuously generated on a thin heating surface. From the viewpoint of the heater area, it can be assumed that bubbles continuously pass through the thin heating surface and transient conduction

is occurring in the entire heating surface. The microlayer evaporation in the area where the heater and the bubble contacted was neglected because the area ratio was relatively small. When using a heat partitioning model such as Basu, assuming that transient conduction is occurring on the entire thin heating surface, the equation is as follows:

Basu, fully transient conduction

$$q_w" = q_{tc}" = \frac{1}{t_w+t_g}\int_0^t \frac{k_l}{\sqrt{\pi\alpha_l t}}(T_{wall}-T_{sat})A_{sl}R_f N_a dt = \frac{2k_l}{\sqrt{\pi\alpha_l}}(T_{wall}-T_{sat})f^{0.5} \quad (4.10)$$

Here, the heat flux and the bubble frequency were obtained through the experimental results, and when the fluid properties are substituted, the unknown value is only the wall temperature. The wall temperature derived through two different equations was compared. It was confirmed that the wall temperature obtained by using the models of Zuber and Yoo et al. coincides with the wall temperature obtained through Basu et al.'s wall heat transfer of the wall. Therefore, in the present experiments conducted on horizontal tubes, it was confirmed that the principle in the thermal phenomenon was the same as the existing models from different geometry. It was confirmed that Zuber's model and Yoo's model, which matched their tendency with the present experiment, can be used on horizontal tubes.

4.3 Development of bubble departure diameter and departure time model

A force balance model can be used to predict the departure time of bubbles and the diameter of departure bubbles. In this study, the equation for predicting the bubble departure diameter in the horizontal tube was derived through the modified force balance model. In the lower half of the horizontal tube, the buoyancy applied to each angle is different, so a model that reflects the angle (position) of the nucleation site is needed. However, in the existing studies, there is no departure diameter model considering the angle of the nucleation site under the horizontal tube.

4.3.1 Development of bubble departure model using a modified force balance model

The modified force balance model presented in Section 4.1 was used to derive the departure diameter model. The forces required for the calculation are buoyancy, drag, and surface tension. The surface tension in the formula shown in Table 4. 1 is when the bubble slides. When the bubble is generated, the dynamic upstream contact angle α and dynamic downstream contact angle β are almost the same. Since α and β are the same, there is a problem that surface tension is calculated as zero. Therefore, this problem was solved by using the surface tension equation that uses only one contact angle when the bubble is stationary, and the surface tension and the remaining forces at this time are as follows:

Buoyancy force

$$F_{b\theta} = (\rho_l - \rho_v) g V_b \sin\theta_b \tag{4.11}$$

Quasi-steady drag

$$F_{qs\theta} = \frac{1}{2} C_d \rho_l {U_l}^2 A_b \tag{4.12}$$

Surface tension for stagnant bubble

$$F_{s\theta} = \pi \sigma R_{b,D} \sin\theta_m (1 - \cos\theta_m) \tag{4.13}$$

At bubble departure,

$$F_{b\theta} + F_{qs\theta} = F_{s\theta} \text{ when } (U_{bulk} > U_{bubble}) \tag{4.14}$$

Therefore,

$$(\rho_l - \rho_v) g V_b \sin\theta_b + \frac{1}{2} C_d \rho_l {U_l}^2 A_b = \pi \sigma R_{b,D} \sin\theta_m (1 - \cos\theta_m) \tag{4.15}$$

Assuming the spherical bubble shape,

$$V_b = \frac{4}{3} \pi R_b^3 \tag{4.16}$$

$$A_b = \pi R_b^2 \tag{4.17}$$

Summing up the expression for R_b

$$(\rho_l - \rho_v) g \frac{4}{3} \pi R_b^3 \sin\theta_b + \frac{1}{2} C_d \rho_l {U_l}^2 \pi R_b^2 - \pi \sigma R_b \sin\theta_m (1 - \cos\theta_m) = 0 \tag{4.18}$$

Divide all sides by R_b,

$$(\rho_l - \rho_v) g \frac{4}{3} R_b^2 \sin\theta_b + \frac{1}{2} C_d \rho_l {U_l}^2 R_b - \sigma \sin\theta_m (1 - \cos\theta_m) = 0 \tag{4.19}$$

Solving the quadratic equation for R_b

$$R_b = \frac{-\frac{1}{2}C_d\rho_l U_l{}^2 \pm \sqrt{\frac{1}{4}C_d{}^2\rho_l{}^2 U_l{}^4 + \frac{16}{3}(\rho_l-\rho_v)g\sigma\sin\theta_m(1-\cos\theta_m)\sin\theta_b}}{\frac{8}{3}(\rho_l-\rho_v)g\sin\theta_b} \quad (4.20)$$

R_b must be a positive real number,

Bubble departure radius

$$R_b = \frac{1}{\sin\theta_b}\left(-\frac{3C_d\rho_l U_l{}^2}{16(\rho_l-\rho_v)g} + \frac{3}{8}\sqrt{\frac{C_d{}^2\rho_l{}^2 U_l{}^4}{4(\rho_l-\rho_v)^2 g^2} + \frac{16}{3(\rho_l-\rho_v)g}\sigma\sin\theta_m(1-\cos\theta_m)\sin\theta_b}\right) \quad (4.21)$$

Organized into dimensionless number Fr_D, l_c

$$R_b = \frac{1}{\sin\theta_b}\left(-\frac{3C_d Fr^2 l_c}{16} + \frac{3}{8}\sqrt{\frac{C_d{}^2 l_c{}^2 Fr^4}{4} + \frac{16}{3}l_c{}^2\sin\theta_m(1-\cos\theta_m)\sin\theta_b}\right) \quad (4.22)$$

Where,

$$Fr_D = \frac{U_l}{\sqrt{g\frac{\rho_l-\rho_v}{\rho_l}l_c}},\ l_c = \sqrt{\frac{\sigma}{g(\rho_l-\rho_v)}}$$

Therefore, the nondimensional bubble departure radius is

Nondimensionalized bubble departure radius

$$\frac{R_b}{l_c} = \frac{1}{\sin\theta_b}\left(-\frac{3C_d Fr^2}{16} + \frac{3}{8}\sqrt{\frac{C_d{}^2 Fr^4}{4} + \frac{16}{3}\sin\theta_m(1-\cos\theta_m)\sin\theta_b}\right) \quad (4.23)$$

4.3.2 Validation of developed departure diameter model and comparison with existing models

The developed departure diameter model in Section 4.3.1 was validated with the experimental results. In addition, the relative performance of the model was confirmed by comparing the departure diameter model used in other mechanistic heat partitioning models.

Basu et al. suggested the departure diameter model empirically based on Maity's (2000) experiments. The Ja_{sup} in the present experiment is very small (wall superheat is low), so it deviates from the valid Ja_{sup} range of this equation, but was used for comparison of tendency. The model is as follows:

Nondimensionalized bubble departure diameter model, Basu et al.

$$\frac{D_d}{l_c} = 1.3(\sin\phi)^{0.4}\left[0.13exp\left(-1.75\times10^{-4}Re_l\right)+0.005\right]Ja_{sup}^{0.45}exp(-0.0065Ja_{sub}) \quad (4.24)$$

Sateesh also derived the departure diameter using the force balance equation of Cornwell and Schuller (1982). Since this model assumes pool boiling, the flow velocity is not reflected and therefore the drag force on the departure diameter is neglected. Sateesh induced the bubble departure diameter at the moment when the buoyancy and the surface tension were equal. However, even though this equation was used under horizontal tube conditions, the angle of the bubble nucleation site was not reflected. The model is as follows:

Bubble departure diameter model, Sateesh et al.

$$D_d = \sqrt{\frac{12N\sigma}{Mg(\rho_l-\rho_v)}} \quad (4.25)$$

Where,

$$\mathrm{N} = \frac{sin\theta_m(1 - cos\theta_m)}{\pi - \theta_m + sin\theta_m cos\theta_m}$$

$$\mathrm{M} = \frac{(2 - cos\theta_m)(1 + cos\theta_m)^2}{\pi - \theta_m + sin\theta_m cos\theta_m} \tag{4.26}$$

Figure 4. 19 shows the evaluation results of bubble departure diameter models. The horizontal axis is the result obtained in the present experiment, and the vertical axis is the bubble departure diameter derived in Section 4.3.1 and the predicted values of the models used in the existing heat partitioning model. Since the contact angle can be different depending on the surface characteristics, the contact angle that best matches the experimental value for each model was used to examine the tendency, and the value is shown in the figure. As a result of the evaluation, the existing models do not consider the angle of the nucleation site of the horizontal tube, so they cannot follow the experimental values at various production angles. On the other hand, since Equation 4.23 considers the angle of the nucleation site, it follows the characteristics on the horizontal tube well. Through these results, the departure diameter of the mechanistic heat partitioning model of the horizontal tube must consider the angle of the nucleation site, and Equation 4.23 is validated.

4.3.3 Development of bubble departure time

Bubble departure time means the time required for the bubble diameter to reach the departure diameter. In the existing mechanistic heat partitioning model of Sateesh, the bubble growth model of Benjamin & Balakrishnan (1996) becomes

equal to Equation 4.25 was determined as bubble departure time. The formula is as follows.

Benjamin & Balakrishnan (1996)

$$D(t) = BAr^{0.135}\left(\frac{Ja_{sup}k_f}{\rho_v c_{pl}}\mathrm{t}\right)^{0.5} \tag{4.27}$$

Therefore, bubble departure time is

Bubble departure time, Sateesh et al.

$$t_d = \frac{12N\sigma c_{pl}}{MgJa_{sup}B^2Ar^{0.27}k_f} \tag{4.28}$$

Where,

$$Ar = \left(\frac{g}{\nu_f^2}\right)\left(\frac{\sigma}{\rho_f g}\right)^{3/2}$$

B=1.55 (4.29)

In the existing mechanistic heat partitioning model of Basu et al., the departure time was determined empirically based on the experimental results of Maity. The formula is as follows.

Bubble departure time, Basu et al.

$$\frac{D_d^2}{\alpha_l Ja_{sup}t_g} = 45exp(-0.02Ja_{sub}) \tag{4.30}$$

In this study, in section 4.3.2 above, the departure diameter was developed using the force balance model, and the time for the bubble to reach this diameter was

obtained with the bubble radius model of Zuber, which is effective for use in horizontal tubes. The departure time equation for the induced bubble is as follows:

$$R(t) = \frac{2bc_{p,l}\rho_l(T_{wall}-T_{sat})}{h_{fg}\rho_v}\sqrt{\frac{\alpha_l}{\pi}t} \qquad \text{(Eqn. 4.7)}$$

Where,

$$\mathrm{b} = \frac{\pi}{2}$$

The time that $R(t)$ in Equation 4.7 reaches 4.23 is departure time:

Bubble departure time

$$t_d = \frac{R_d^2}{Ja^2\pi\alpha_l} \qquad (4.31)$$

Therefore,

Nondimensionalized bubble departure time

$$\frac{{t_d}^{0.5}}{l_c}\sqrt{\alpha_l} = \frac{1}{\mathrm{Ja}\cdot\sqrt{\pi}\sin\theta_b}\left(-\frac{3C_dFr^2}{16}+\frac{3}{8}\sqrt{\frac{{C_d}^2Fr^4}{4}+\frac{16}{3}\sin\theta_m(1-\cos\theta_m)\sin\theta_b}\right) \qquad (4.32)$$

4.4 Closure of the bubble frequency model

The detailed description of the bubble frequency and the experimental results are given in Section 3.2. In this study, bubble frequency was acquired experimentally. However, this experiment was carried out on a thin heating surface, and due to these characteristics, the thermal properties and boiling phenomena may be slightly different from those on a wide heating surface. In the experimental results, the tendency of frequency by each variable was clear, but it was smaller than the predicted value of the existing frequency model as Figure 4. 20.

Therefore, in this study, no new frequency model was proposed based on the experimental results. In order to avoid a new model that can show a difference from the existing frequency model and the final calculated wall heat flux, which is a significant difference from the existing boiling study, a model that has been sufficiently validated under various thermal and hydraulic conditions was used.

Representative existing frequency models include Cole (1967), Ivey (1967), Stephan (1992), and Jakob (1949). The equation of each model is as follows.

Bubble frequency model, Cole

$$f = \sqrt{\frac{4}{3}\frac{g(\rho_l-\rho_v)}{D_d\rho_l}} \tag{4.33}$$

Bubble frequency model, Ivey

$$f = 0.9\sqrt{\frac{g}{D_d}} \tag{4.34}$$

Bubble frequency model, Stephan

$$f = \frac{1}{\pi}\sqrt{\frac{g}{2}\left(D_d + \frac{4\sigma}{\rho_l g D_d}\right)} \tag{4.35}$$

Bubble frequency model, Jakob

$$f = 0.59\left[\frac{\sigma g(\rho_l - \rho_v)}{\rho_l{}^2 D_d{}^2}\right]^{0.25} \tag{4.36}$$

Of these models, the model of Cole has been cited and validated by various researchers so far and is widely used in commercial CFD codes such as STAR-CCM+ (2013) and CFX (1997). Therefore, this study used Cole's model to maintain consistency with existing studies.

4.5 Variables that require numerical modeling-

In this study, the sliding distance of the bubble, the sliding area, lift-off diameter, and merger was obtained through numerical modeling. On the lower part of the horizontal tube or downward heating surface, even if the bubble has sufficient force to lift-off, the bubble does not fall off the surface due to the upper structure that physically suppresses the lift-off of the bubble. And bubble lift-offs when it approaches near the 90° of horizontal tube. In the upper part of the horizontal tube, bubbles don't slide but continue to grow at the nucleation site, and when they reach a certain size, lift-off diameter, they detached from the surface. In conclusion, in the upper half of the horizontal tube, the lift-off can be predicted or the lift-off diameter can be predicted by calculating the force balance in the same way as the existing horizontal and vertical planes. On the other hand, in the lower half of the horizontal tube, the bubble does not lift-off from the surface until it reaches around 90°, so it

slides up to this angle and the increased final size becomes the lift-off diameter. Bubbles do not lift-off from the surface during the slide, so the bubble size increases continuously. In addition, since the total force on the bubble varies depending on the bubble growth rate, the bubble velocity also changes. It is also very likely to collide with other bubbles created at different nucleation sites during the sliding. Therefore, in order to accurately predict the lift-off diameter, the number of nucleation sites located in the sliding path of the bubble and the bubbles generated at the sites must be taken into consideration while the bubble is sliding. In addition, for accurate calculation, it is necessary to consider even having different bubble departure frequencies for each site. On the lower half of the horizontal tube, the departure diameter is different depending on the angle of sites because the buoyancy is different depending on the angle at which the nucleation site is located. Considering that the bubble departure frequency is inversely proportional to the departure diameter, the bubble departure frequency is different depending on the angle at which the nucleation site is located. Therefore, as a characteristic of the complex boiling phenomenon under the horizontal tube, the mechanism of bubble generation and merging is very complex, and it is impossible to mathematically predict precisely. Therefore, the lift-off diameter at the lower part of the horizontal tube is appropriate through a numerical simulation that considers the bubble growth model, velocity model, departure diameter model, and frequency model that reflect the surface information well, rather than providing an analytic prediction model.

Table 4. 1 Forces acting in the θ direction (Kim et al., 2017)

Force	Equation		Remarks
Buoyancy force	$F_{b\theta} = (\rho_l - \rho_v)\mathrm{g}V_b sin\theta_b$	(1)	
Quasi-steady drag force	$F_{qs\theta} = -\frac{1}{2}C_D\rho_l(U_b - U_l)\lvert(U_b - U_l)\rvert A$ $A = \left(\frac{3}{4}\pi^{1/2}V_b\right)^{2/3}$	(2)	$C_D = 0.44$ (1997), where A was calculated assuming a spherical bubble shape
Surface tension force	$F_{s\theta} = -\int_0^{\pi} d_w\sigma cos\gamma cos\phi d\phi$ $\sim d_w\sigma\frac{\pi(\alpha-\beta)}{\pi^2-(\alpha-\beta)^2}(sin\alpha + sin\beta)$	(3)	Mean values of the experimental dynamic contact angle; α = 45°, β = 30°
Added mass force	$F_{am\theta} = -\frac{1}{2}V_b\rho_l\alpha_\theta - 2A\rho_l(U_b - U_l)\dot{r_b}$	(4)	

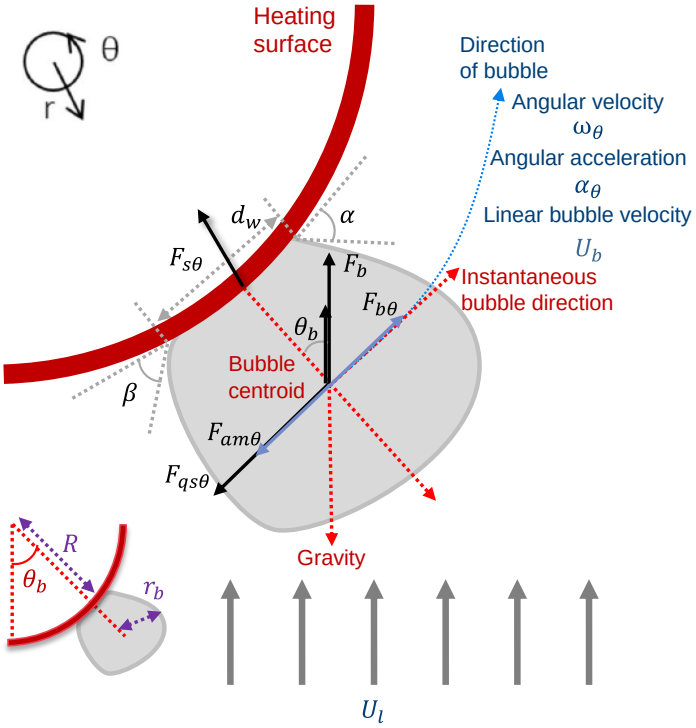

Figure 4. 1 Acting forces on the bubble in the θ direction.

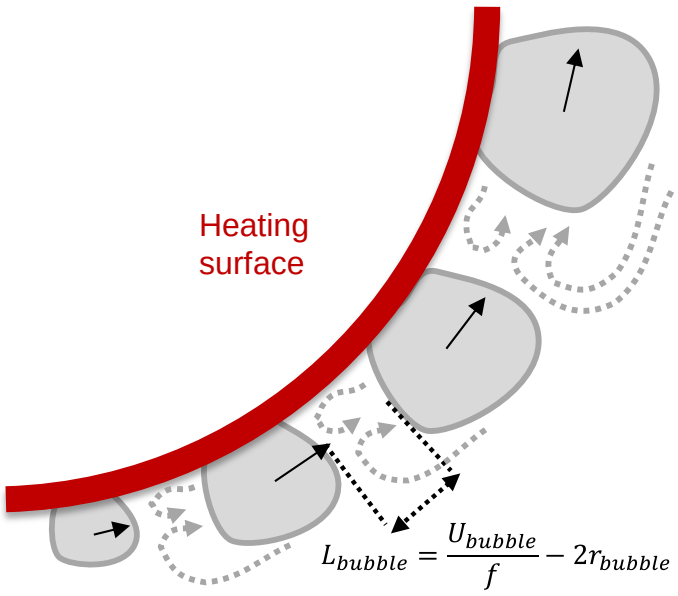

Figure 4. 2 Increase in the local liquid velocity with continuous bubbles.

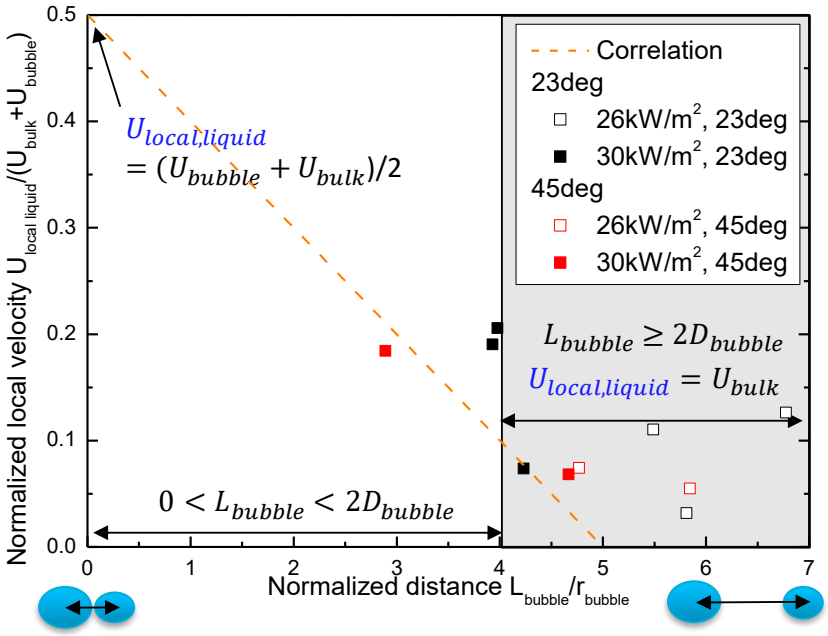

Figure 4. 3 Bubble distance and liquid velocity correlation

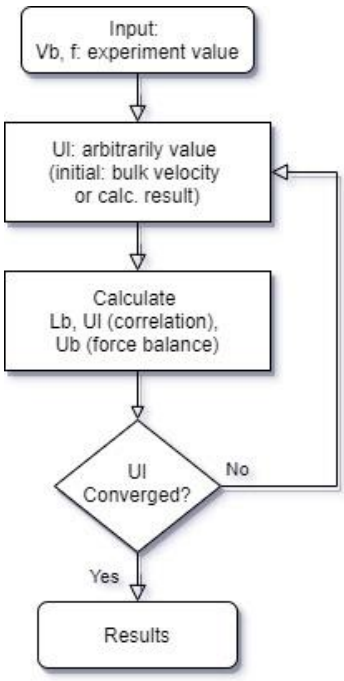

Figure 4. 4 Calculation procedure of bubble velocity

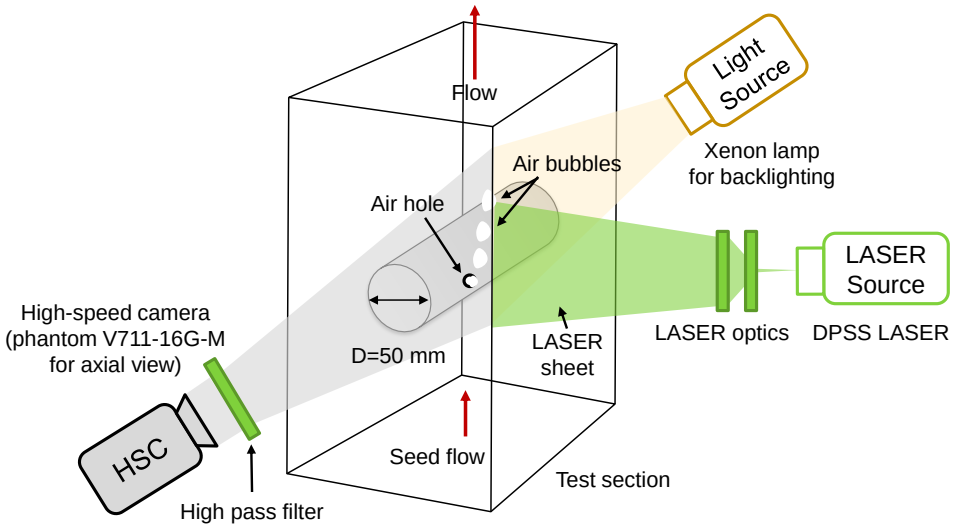

Figure 4. 5 Schematic diagram of the test section and set up for the PIV, PTV visualization system.

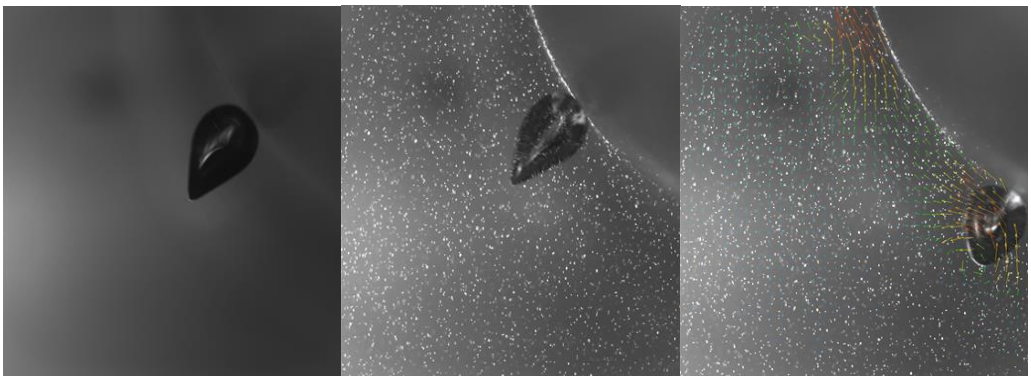

Figure 4. 6 Image samples of: (a) Bubble image, (b) Bubble image with laser, (c) PIV analysis result

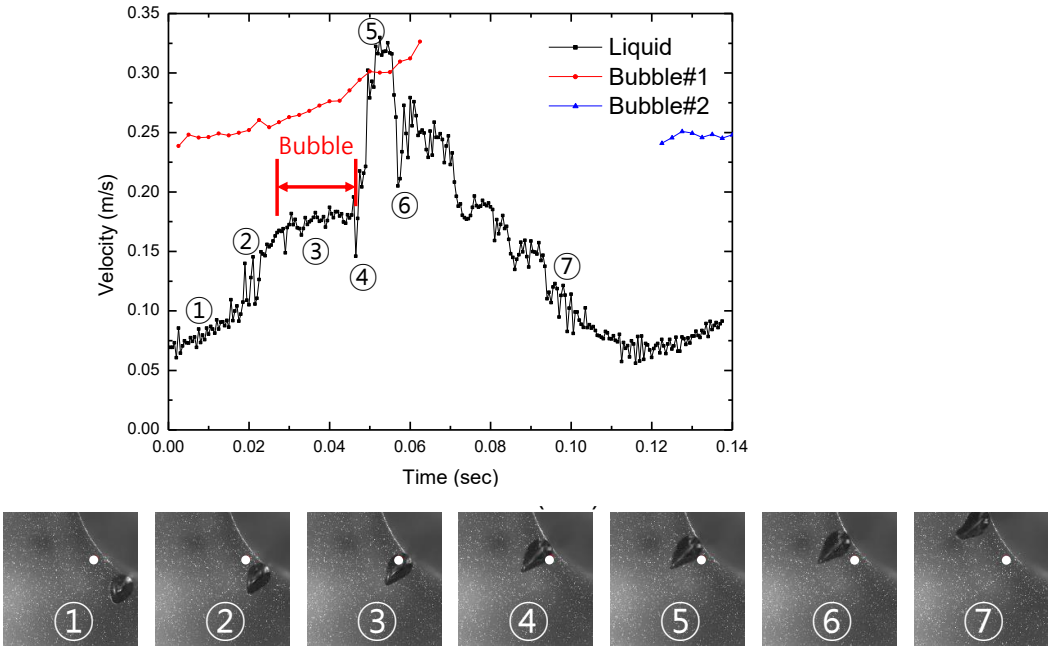

Figure 4. 7 Local liquid velocity and bubble velocity at the measuring point

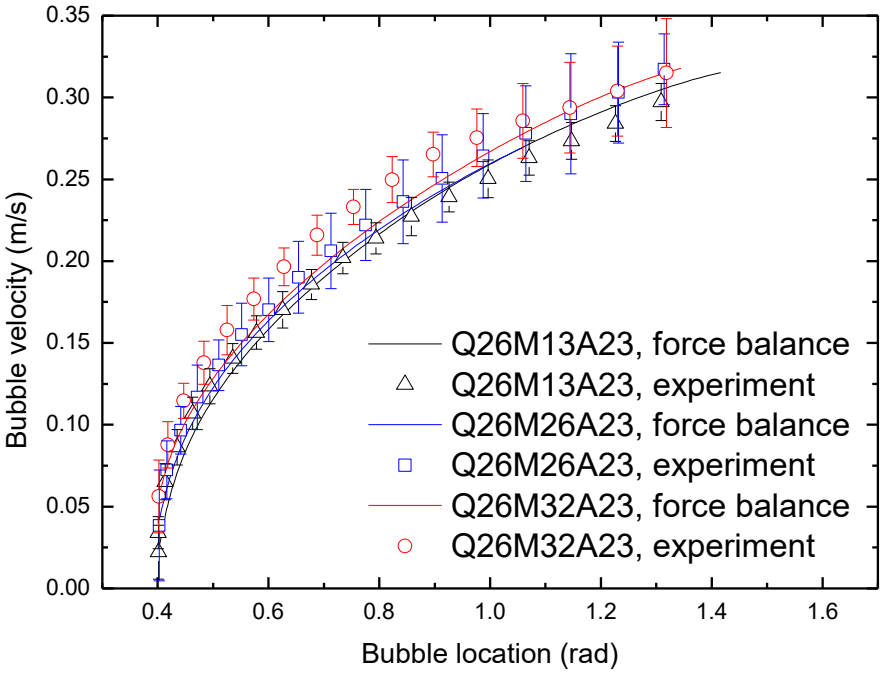

Figure 4. 8 Bubble velocity along the circumference: Q26A23

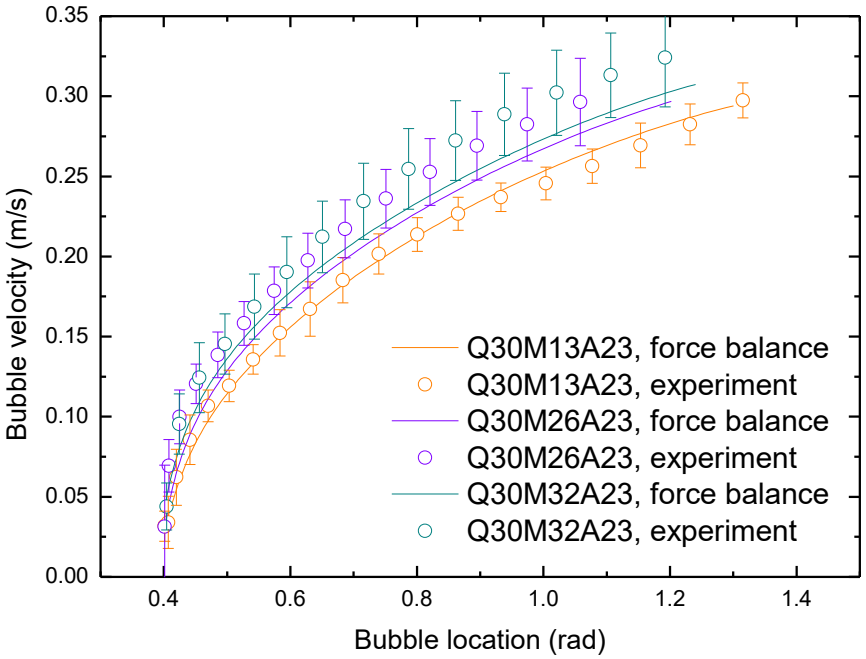

Figure 4. 9 Bubble velocity along the circumference: Q30A23

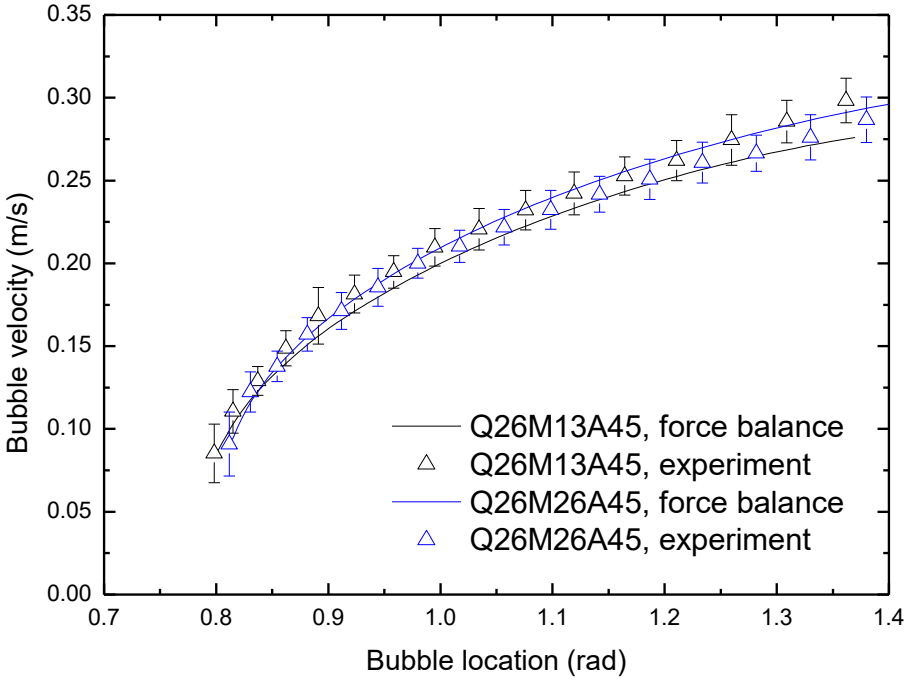

Figure 4. 10 Bubble velocity along the circumference: Q26A45

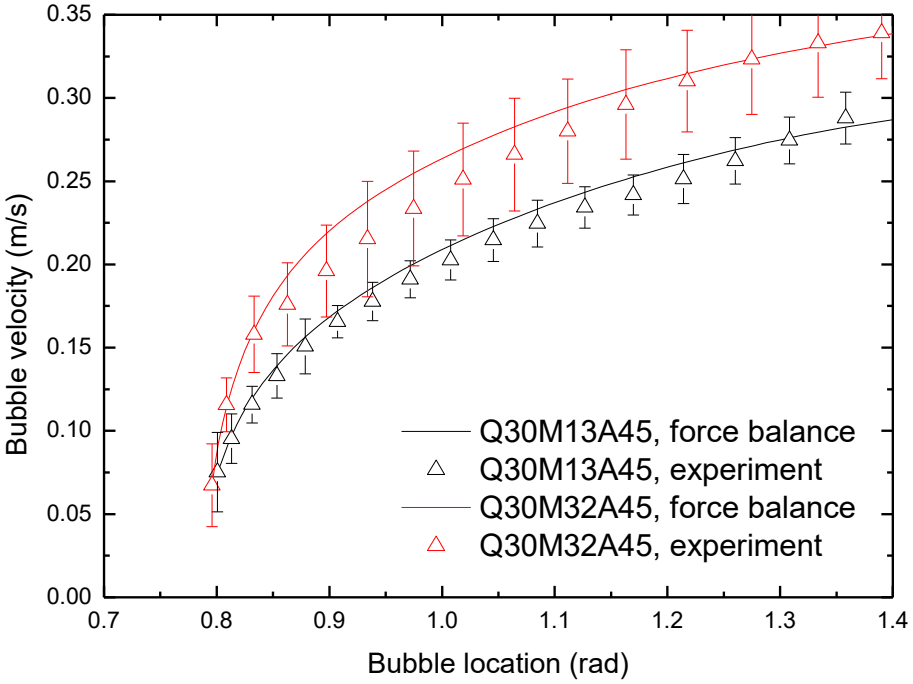

Figure 4. 11 Bubble velocity along the circumference: Q30A45

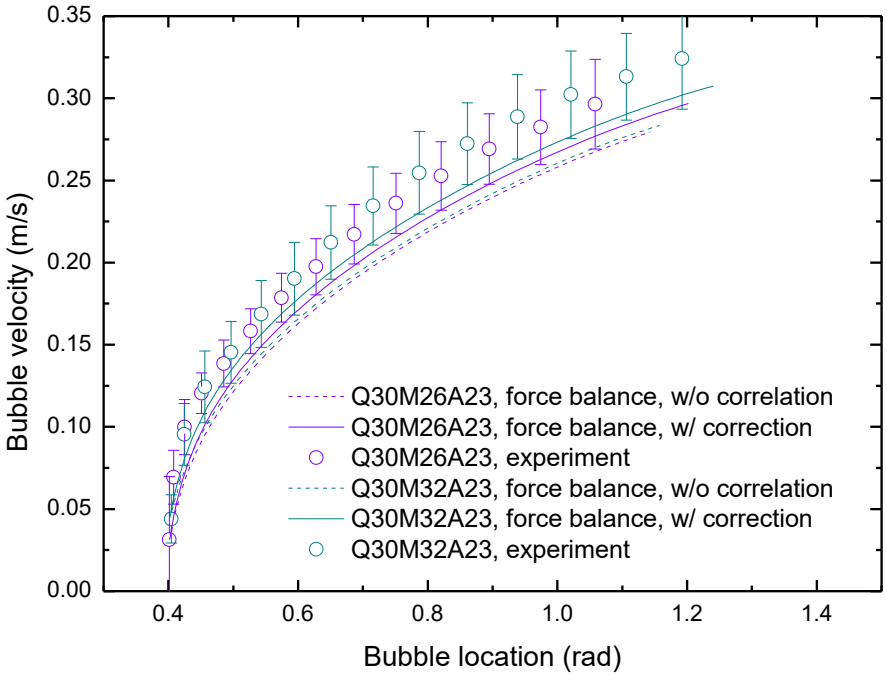

Figure 4. 12 Bubble velocity along the circumference before and after liquid velocity correction: Q30A23

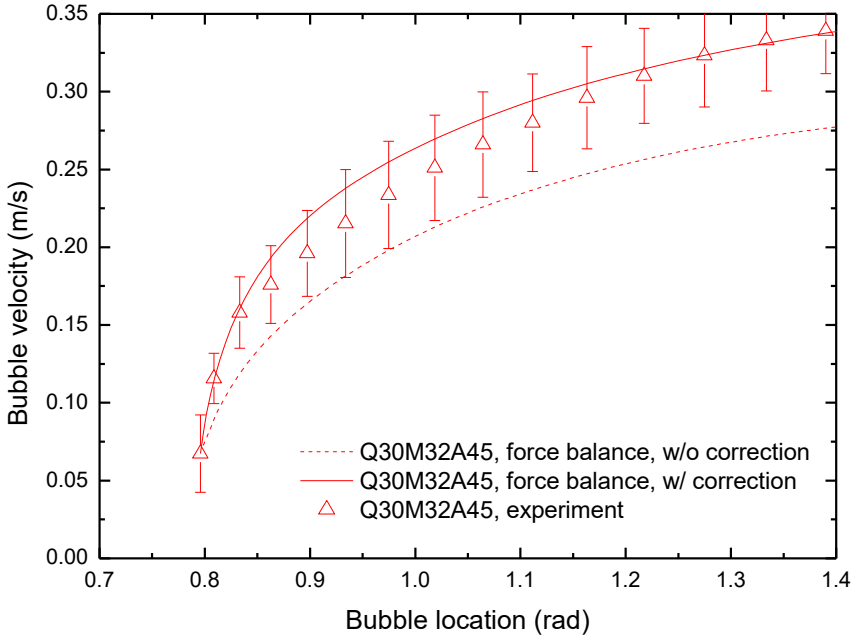

Figure 4. 13 Bubble velocity along the circumference before and after liquid velocity correction: Q30A45

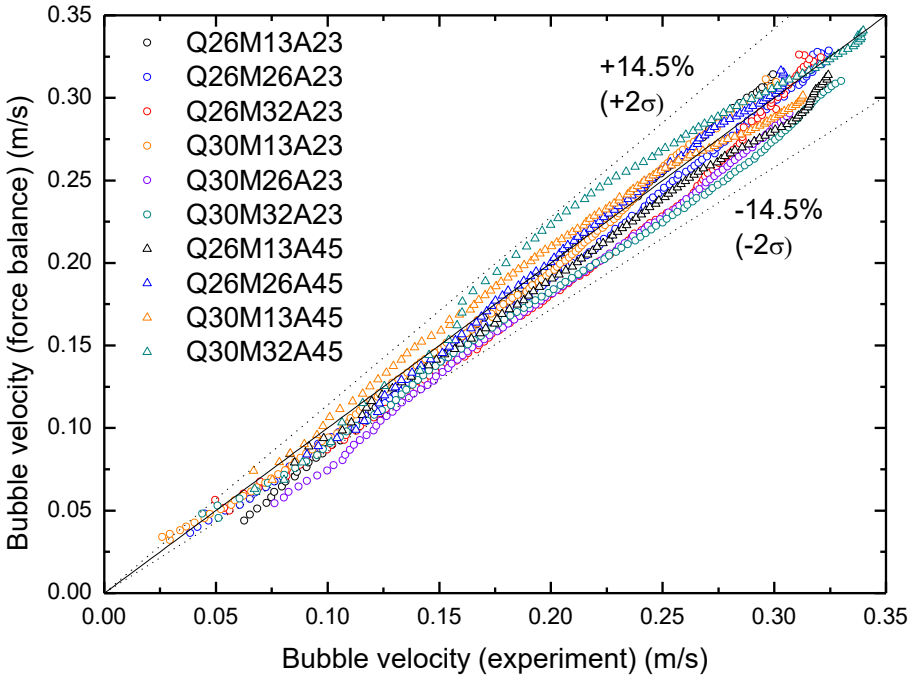

Figure 4. 14 Estimated bubble velocity.

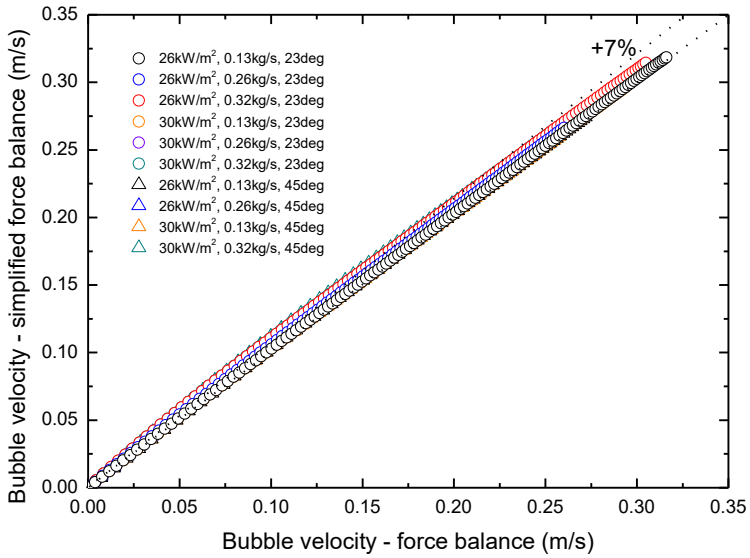

Figure 4. 15 Simplified force balance calculation results (only buoyancy and drag

force)

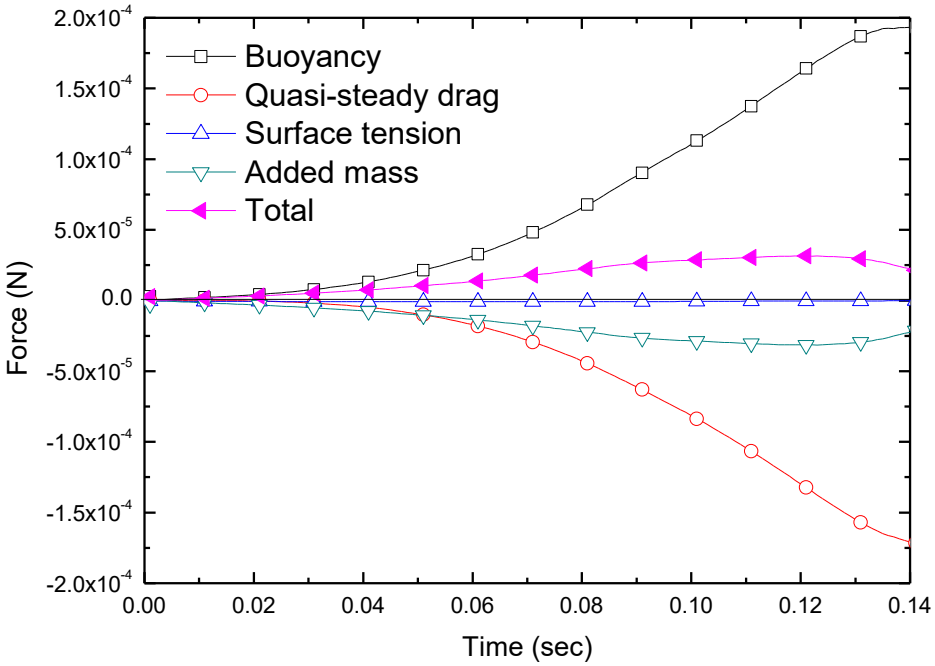

Figure 4. 16 Force balance analysis results: Q26M13A23

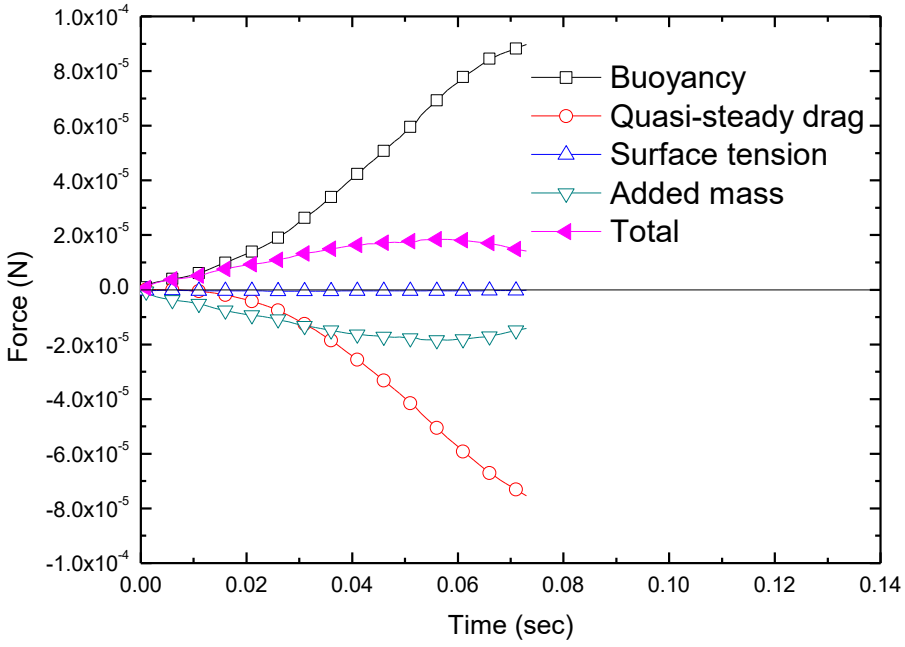

Figure 4. 17 Force balance analysis results: Q26M13A45.

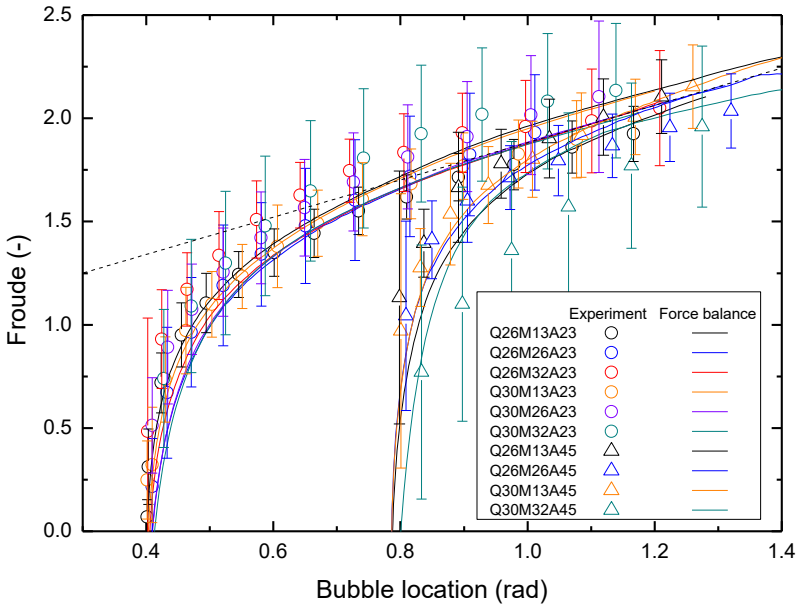

Figure 4. 18 Froude number according to the bubble position

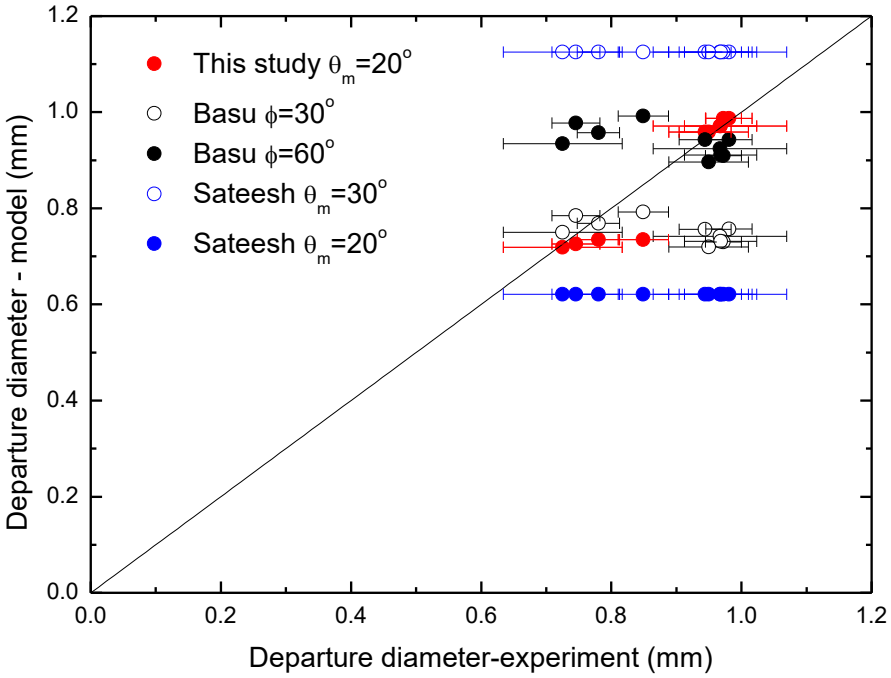

Figure 4. 19 Assessment of bubble departure model

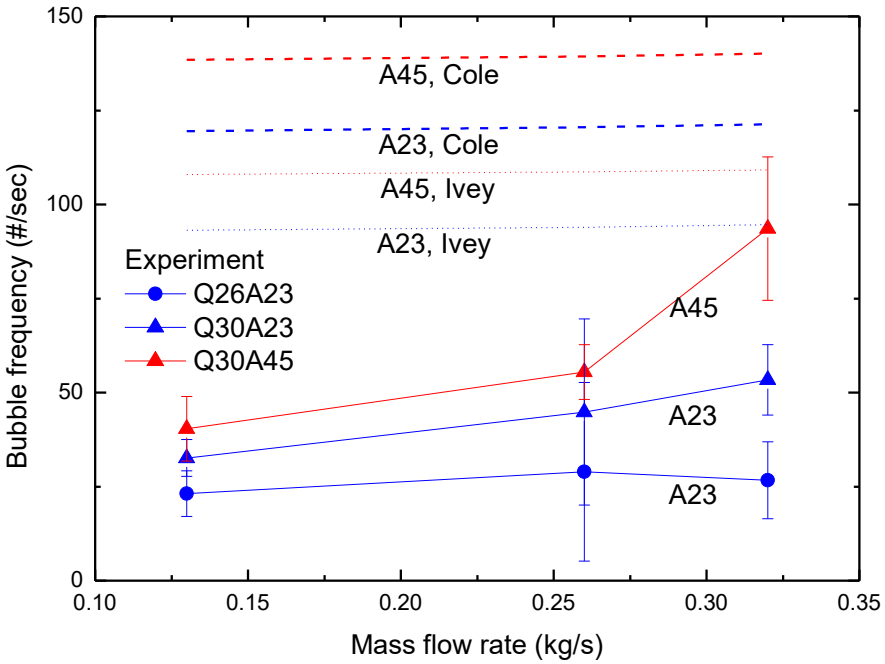

Figure 4. 20 Comparison of experimental results with the existing frequency model

Chapter 5

Numerical modeling of bubble tracking, merger, and wall heat partitioning

5.1 Concepts of numerical modeling

In this study, a numerical bubble tracking and merging model using the

experimental results were developed and the developed sub-models were introduced in previous chapters 3 and 4. Previously, existing models simplified complex phenomena such as bubble formation and merging with average behavior. However, the actual boiling phenomenon is very complex as introduced in Section 4.5, so the analytic approach can be different from the actual phenomenon. In addition, the analytic approach has the limitation of simplifying the boiling phenomenon excessively or not accurately reflecting the actual physical phenomenon even though it is a mechanistic model.

Therefore, in this study, through the developed sub-models, individual bubbles have physically reasonable sliding behavior, and numerical modeling to track their sliding and merging was developed to complete the mechanistic boiling heat transfer model of the horizontal tube. The computational area is an unfolded heating surface of the horizontal tube, with a square area corresponding to the area of a quarter arc length of the tube. For example, in the case of 50mm diameter, it has an unfolded arc length of about 3.9cm and a square (3.927cm X 3.927cm) calculation area. Nucleation sites are distributed according to options within unfolded area. As an option, the user can choose to have a uniform, random or Latin hypercube distribution of sites. Examples of both options are shown in Figure 5. 1. The uniform option is to distribute the nucleation site's position in a uniform grid. This approach corresponds to the assumptions made for the simplification of the problem in other previous studies. The random option is to position the nucleation site completely randomly over the entire heating area. Lastly, the Latin hypercube is to divide the heating area into a uniform grid form equal to the number of sites, and then randomly arrange each site within the area. The random and Latin hypercube methods are very similar to the characteristics of the actual boiling heating surface.

In the case of random and Latin hypercube site distribution, different results values are derived depending on the combination of site distribution. In addition, the site was randomly distributed within the area using the Monte-Carlo method, and it was calculated by repeated several times with randomly distributing each time. When the random distribution option is used, MATLAB's 'RAND' function is used (2019), and the distribution at this time follows the uniform random distribution. Through the Monte-Carlo method, it is possible to know the range (high and low limit) and average value of results that can occur for each sites distribution combination. In the calculation, the user can determine the number of calculations to repeat. Besides, calculations were made to select the upper and lower half of horizontal tubes. For the total calculation time and its time step can be set. The results include heat flux for each heat transfer mechanism, time and area averaged heat transfer area ratio, bubble lift-off diameter, and transient conduction index. The model was developed using a commercial MATLAB code with the R2019b version. The source code attached in the appendix. For optimization of computational speed, vectorization and pre-allocation of matrix were adopted and the parallel computing was applied using MATLAB Parallel Computing Toolbox™.

5.2 Sub-models application on numerical model

The applied sub-models are shown in Table 5. 1 and Table 5. 2. The sub-model developed in this study is shown in Table 5. 1, and the types are divided into mechanistic modeling, numerical modeling, and experimental observation results. Likewise, Table 5. 2 shows the applied existing models of other researchers.

5.2.1 Single-phase convection model

Single-phase convection occurs in the rest of the heating surface where microlayer evaporation or transient conduction does not occur. This study targeted pool boiling or natural convection conditions of PAFS at low flow rates of 0.028 m/s or less. When the PAFS starts to operate, the temperature of the water tank is very low at room temperature conditions of around 300 K. In this case, in order to accurately predict the heat transfer in the heat exchanger during the entire operating time, the heat transfer model must be extended to the range of natural convection with high subcooling. Therefore, Jeon et al. (2015) developed a natural convection model at high subcooling for a U-shaped heat exchanger submerged in a water tank. The model is as follows:

Single-phase natural convective heat transfer model, Jeon et al.

$$Nu_{lower} = 0.0117 Ra_D^{0.514} \quad (5.1)$$

5.2.2 Nucleation site density

The number of nucleation sites on the heated surface depends on a variety of properties, such as the material and the surface properties, and the surface finish or scratches. Under the same surface condition, the number of nucleation sites increases exponentially with increasing superheat. The number of nucleation sites on the surface follows the Poisson distribution (Sultan. M. & Judd. R. L., 1978). The Poisson distribution is a discrete probability distribution function, which is effective when events that occur are independent of each other and do not affect other events. Sites are randomly present on the surface.

In this numerical model, nucleation site density is calculated using the wall superheat. In this study, Hibiki-Ishii (2003) model is used. This model is known to have good predictive results over a wide range of thermal and hydrodynamic conditions. The calculation result according to the pressure is shown in Figure 5. 2. The equation is as follows:

Hibiki-Ishii nucleation site model

$$N_a = \overline{N_a}\left[1 - exp\left(-\frac{\theta^2}{8\mu^2}\right)\right]\left[exp\left(f(\rho^+)\frac{\lambda'}{R_c}\right) - 1\right] \quad (5.2)$$

Where,

Minimum cavity radius

$$R_c = \frac{2\sigma[1+(\rho_v/\rho_l)]/P}{exp[h_{fg}(\Delta T_{sup})/(R_g T_w T_{sat})]-1} \quad (5.3)$$

Density function

$$f(\rho^+) = -0.01064 + 0.48246\rho^+ - 0.22712{\rho^+}^2 + 0.05468{\rho^+}^3 \quad (5.4)$$

$$\rho^+ = log_{10}\left(\frac{\rho_l-\rho_v}{\rho_v}\right) \quad (5.5)$$

$$\overline{N_a} = 4.72 \times 10^5 sites/m^2 \quad (5.6)$$

$$\mu = 0.722\, rad \quad (5.7)$$

Cavity length scale

$$\lambda' = 2.50 \times 10^{-6} m \quad (5.8)$$

5.2.3 Bubble growth model

Bubble growth is determined by the sum of heat transfer by microlayer evaporation at the bubble base, heat transfer of the evaporation of the superheated layer around the bubble, and condensation heat transfer in the subcooled layer. The detailed description of the existing model is described in Section 4.2. In this study, the model of Yoo et al., which reflects both superheat and subcooling, was used as a model for bubble growth. The model has been validated up to 13.5K subcooling. In this study, the effective subcooling range of the entire heat transfer model is determined by the bubble growth model.

5.2.4 Bubble velocity model

The bubble velocity is obtained using the force balance model and bubble velocity model obtained in Section 4.1. Using the bubble growth model, the volume of the bubble is obtained, and then the force applied to the bubble is calculated using time marching. In addition, the bubble velocity model developed in this study considers the wake effect according to frequency. Therefore, even if all the hydraulic conditions except the frequency are the same, as the frequency increases, the local liquid velocity increases, thereby increasing bubble velocity. The calculation results are shown in Figure 5. 3, and it can be seen that the characteristics by frequency are well represented.

5.2.5 Bubble frequency model

Cole's model is used as the bubble frequency model, it has been sufficiently validated by several researchers, and, which is still widely used in CFD. As the departure diameter is required in this model, the horizontal tube departure diameter model developed in this study was used. Therefore, the frequency is slightly different depending on the angle of the bubble generation point.

5.2.6 Area of influence

Area of influence, K, refers to the area under which transient conduction occurs and heat transfer is enhanced by a bubble. As the bubbles lift-off or slide the walls, the wake and vortex induced by the bubbles disturb the surrounding superheated layer. As a result, the surrounding fluid is filled into the place where the bubbles pass, and heat transfer is temporally enhanced. For the influenced area calculation, it was generally used to multiply constant the area of influence K on the projection of the sliding area. Judd and Hwang (1976) proposed this value to be 1.8 based on fitting the experimental value, and Han and Griffith (1962) proposed 4.0 through an experiment using chalk powder. With the development of technology and experimental methodology, the K values obtained through more advanced experimental methods have been continuously proposed. Kenning and Yan (1996) proposed K=1 through liquid crystal experiments, and Demiray and Kim (2004) proposed K=0.25. In addition, Golobic (2009) proposed K<1.0 based on experiments using an IR thermometer. Recently, Amidu et al. (2018) suggested the K value of the sliding bubble to be 0.5 through experiments using both ITO heater,

IR thermometry, and a high-speed camera. In this study, it was judged that the methodology and results of this experiment reflected the K value of the sliding bubble well, and a value of 0.5 of Amidu et al.'s was adopted for analysis.

5.2.7 Contact diameter

For the upper half of the horizontal heater, based on Jung et al. (2015) the contact diameter was assumed to be 0.5 times of the total bubble diameter. Based on the results of this experiment, For the lower half of the tube was assumed to be about 0.35 times the total bubble size. This is because the average contact diameter ratio averaged for each condition in the entire case was 0.3 - 0.4 in the experiment (Figure 3. 10 - Figure 3. 13). The contact area gradually decreases as the bubbles slide. This has been reported not only in the experiments of this study but also in the studies of other researchers, including Yoo et al. (2018)

5.3 Assumptions of the numerical model

In the model, it is assumed that the bubble is always spherical shape, and if the distance between the center points of the bubble is less than the sum of the radius of both bubbles, the bubbles are merged into one bubble that preserves mass and momentum.

The numerical model checks for collisions by calculating the distance between all bubbles in the area according to the timestep. At this time, it was assumed that if the distance between the two bubbles is equal or shorter than the sum of the radius of both bubbles, they are merged into one spherical bubble. At this time, the mass

and momentum of both bubbles before merging are preserved after the merger. The formula for calculating the distance between bubbles is shown below and a schematic drawing is shown in Figure 5. 4.

Bubble radial distance

$$dist_{radial} = \left({l_1}^2 + {l_2}^2 - 2l_1 l_2 \cos\alpha\right) \tag{5.9}$$

Merge when:

$$R_1 + R_2 \geq \sqrt{{dist_{axial}}^2 + {dist_{radial}}^2} \tag{5.10}$$

5.3.1 Model application of lower half of horizontal tube

Based on the experimental results, the bubbles generated at the lower half of the tube continue to grow and slide until reach the 90-degree angle without lift-off from the surface. As described in Section 5.2.7, the contact diameter was considered to be on average 35% of the bubble diameter. In this case, the heat is transferred from the wall to the surrounding superheated layer using transient conduction and single-phase convection, and the heat transfer to the bubble is caused by microlayer evaporation. In addition, heat transferred by the evaporation of the superheated layer and the effect of condensation by subcooling are additionally considered for bubble growth.

5.3.2 Model application of upper half of horizontal tube

Through the experiment of this study, it was confirmed that the bubbles generated at the upper half of the tube did not slide, but immediately lift-off when they reached a certain size called lift-off diameter. Therefore, in this numerical modeling, Basu's experimental bubble lift-off model was used, which was considered to lift-off immediately from the computational domain if the bubble reached this size. When leaving, the bubble's projected area to heater surface multiplied by the area of influence K is affected by the transient conduction.

5.4 Description of the calculation procedure

The calculation flow chart of the code is shown in Figure 5. 5. The calculation procedure is divided into 1. bubble initial information calculation, 2. bubble merger calculation, and 3. transient conduction calculation.

5.4.1 Step 1. Bubble initial information calculation

The code calculates the nucleation site density ($\#/cm^2$) under the given wall superheat. Nucleation site density is multiplied by the area of the unfolded surface to obtain the total number of sites in the calculated area. Then, according to the options, the sites are distributed in an area randomly or uniformly. Bubbles are generated at each of these sites until the calculation is completed, and the x-axis position, theta-axis position, bubble velocity, and bubble radius information for the bubble are stored in each matrix. Each variable has its matrix of information, which represents the time in rows and each unique bubble in columns, as shown in Figure 5. 6. Therefore, the total number of rows is the calculation time divided by the time

step interval (ex, 0.3 sec calculation, 0.001 sec timestep: 300 rows). In addition, the column is the number of total nucleation sites multiplied by the frequency and the calculation time (ex, 1,000 sites, 100#/sec frequency, 0.3sec calculation: 1,000 X 100 X 0.3 = 30,000 columns). Elements that do not contain bubble information are treated as NaN. The bubble information stored in Step 1 has independent location and size information without considering the interaction between each other.

5.4.2 Step 2. Bubble merger calculation

In Step 2, the bubble information matrix is marched over time, and the distance between the bubbles is checked to calculate the merging of bubbles. The bubble distance equation is shown in Equation 5.10. The distance between bubbles in the current timestep (row) is calculated through the x-axis and theta-axis location matrix of bubbles. If there are m columns exist, the maximum number of calculations in the current timestep is theoretically m-1 + m-2 + m-3… +1. However, elements that do not contain bubble information are treated as NaN, and in the case of NaN, the distance is skipped without calculating the distance to reduce computational cost. The merged new bubble is updated by calculating the velocity of the new single bubble series, with the initial condition of the sum of the mass and momentum of the bubble before the merger. Information about the new bubble occupy one of the two bubbles information columns before the merger, and the information after the merger of the other bubble is filled with NaN. After checking the distance between all the bubbles in this row and calculating the merger, it is finished and time marches to the next timestep.

5.4.3 Step 3. Transient conduction calculation

In this step, the code calculates the transient conduction using the location and radius information of the bubble. The transient conduction matrix is a matrix that contains the degree of transient conduction for the area. The size of this matrix can be determined according to the calculation settings. In this study, the size of the matrix was set to $1{,}024 \times 1{,}024$. In the case of a 50 mm tube diameter, the area to be calculated is 3.927cm X 3.927cm, and if it corresponds to 1,024 pixels, it has a resolution of $0.038mm \times 0.038mm$ per each pixel. Also, the time step of the calculation was 1 ms, and it was judged that the bubble growth model had sufficient resolution for the increment over 1 ms. The result is saved for total calculation time, that is, a transient conduction matrix having a size of $1{,}024 \times 1{,}024 \times timesteps$.

Since steps 1 and 2 know the location and radius of the bubble over time, the code multiplies the radius of the bubble from the center point of the bubble location and the area of influence constant $\sqrt{K}$ indicating the area where transient conduction occurs. Then, it fills the transient conduction matrix corresponding to the area inside the drawn circle with $t^* - 1$, one less than the transient time t^*. The methodology is shown in Figure 5. 7.

In addition, in order to obtain a region contributing to microlayer evaporation, the region inside the size multiplied by the d_w/d_b constant representing the ratio of the bubble diameter to the contact diameter is filled with t^* corresponding to the transient time. This pixel is not an area corresponding to transient conduction, but the area where microlayer evaporation occurs.

In order to calculate the transient conduction area where the bubble has passed, if the pixel value is non-zero and not the area filled by a bubble in this timestep,

subtract 1 from the pixel value. This allows transient conduction to decay over and it is stored in the form of the transient conduction time. Figure 5. 8 shows the still shot of the bubble and the corresponding transient conduction matrix.

5.4.4 Calculation result analysis

After all, calculations are completed, the pixel stored as t^* in the final result is judged as the area of microlayer evaporation, and the pixel with the value in the range from 1 to $t^* - 1$ is judged as an area of transient conduction. Lastly, the pixel with the zero stored, it is determined as the area that single-phase convection has occurred. The number of pixels can be averaged over the entire time and area to obtain a ratio of heat transfer regions for each mechanism. In particular, in the case of a pixel in which transient conduction has occurred, the value of the time index averaged over the entire transient conduction area can be calculated by averaging the value, which is defined as a transient conduction time index I_{tc}. This is illustrated in Figure 5. 9.

In the calculation result, bubbles repeat generation, slide, and merge, and converge to a state that seems to have a cycle over a period of time. From this time, the number of bubbles existing in the calculation area and the number of merged bubbles shows a periodicity having a specific range. Using this, the time average of the final result is given as a multiple of the cycle that includes the result of the total calculation time as much as possible. The instantaneous behavior of the bubbles and the transient matrix averaged over the entire time, in this case, are shown in Figure 5. 10.

Finally, the calculated results are obtained for each heat transfer by the

mechanism through the following equations:

Microlayer evaporation heat flux equation

$$q_{ev}" = \frac{A_{ml}}{A_{tot}} \delta_{ml} \rho_f h_{fg} \frac{1}{t_{tot}} \tag{5.11}$$

Transient conduction heat flux equation

$$q_{tc}" = \int \frac{k_l (T_w - T_l)}{\sqrt{\pi \alpha_l t}} dt \tag{5.12}$$

Transient conduction heat flux equation from other studies

$$q_{tc}" = \frac{k_l (T_w - T_l)}{\sqrt{\pi \alpha_l}} 2f \sqrt{t_w} A_s K N_a \tag{5.13}$$

Transient conduction heat flux equation in this study

$$q_{tc}" = \frac{k_l (T_w - T_l)}{\sqrt{\pi \alpha_l}} \frac{1}{t_{calc} A_{T.C.}} \sum_{j=1}^{A_{T.C.}} \sum_{i=1}^{t_{calc.}} \frac{1}{\sqrt{t_i}} \Delta t \Delta A = \frac{k_l (T_w - T_l)}{\sqrt{\pi \alpha_l}} I_{T.C.} \frac{A_{T.C.}}{A_{tot}} \tag{5.14}$$

Where,

Transient conduction time index

$$I_{tc} = \frac{1}{t_{calc} A_{T.C.}} \sum_{j=1}^{A_{T.C.}} \sum_{i=1}^{t_{calc.}} \frac{1}{\sqrt{t_i}} \Delta t \Delta A \tag{5.15}$$

Single-phase convection heat flux

$$q_{sc}" = h_{sc} (T_w - T_l) \frac{A_{sc}}{A_{tot}} \tag{5.16}$$

Total wall heat flux

$$q_w" = \frac{A_{sc}}{A_{tot}} h_{sc}(T_w - T_l) + \frac{A_{tc}}{A_{tot}} I_{tc} \frac{k_l(T_w - T_l)}{\sqrt{\pi \alpha_l}} + \frac{A_{ml}}{A_{tot}} \delta_{ml} \rho_f h_{fg} \frac{1}{t_{tot}} \quad (5.17)$$

5.4.5 Monte-Carlo method

Figure 5. 11 to Figure 5. 14 are the result of the calculation code displayed using the 3D option. When comparing Figure 5. 12 and Figure 5. 13, the arrangement of the uniform site is somewhat different from the actual boiling phenomenon. Conversely, the randomly arranged site looks similar to the actual boiling phenomenon. For the randomly distributed sites, the results were averaged after repeating the calculation several times using the Monte-Carlo method. The result is shown in the range of possible result values as shown in Figure 5. 15. In addition, the I_{tc} and A_{sc}/A_{tot} of Monte-Carlo calculation allows comparative evaluation of existing researchers' uniform distribution assumptions.

In the case of random distribution, the number of repetitions for Monte-Carlo method can be specified by the user. Figure 5. 16 is a transient conduction matrix when one calculation is performed using the random option. In addition, Figure 5. 17 shows the average result after calculating 3,000 iterations of random calculation. The higher intensity of transient conduction occurs in the upper part than in the lower part, and this tendency is uniformly distributed in the entire area. This is because bubbles slide and pass through the upper area for most of the time, so it is higher than the probability that the bubbles are in the lower part.

In consideration of the calculation time and accuracy, the number of repetitions was set to 500 to 3,000 repetitions. After calculation, the area occupied by each heat transfer mechanism was tested to follow the normal distribution or the chi-square distribution. The overall result can be analyzed using the average of the repeated

calculations and the maximum, minimum, or 2-sigma range data.

5.4.6 Normal distribution test and Chi-square test

Kolmogorov-Smirnov test was performed using the ‘kstest’ function built into MATLAB's statistics and machine learning toolbox to confirm that the calculated results are normally distributed. If the test result rejects the null hypothesis at the 5% significance level, it can be said that it does not follow the normal distribution. In the case of Monte-Carlo calculation, the results were used for analysis after confirming that the repeated results follow the normal distribution.

In addition, a chi-square test was performed using the ‘chi2gof’ function built into MATLAB to confirm that the calculated result conforms to the chi-square distribution. Similarly, if the test result rejects the null hypothesis at a significance level of 5%, it can be said that the chi-square distribution is not followed.

Table 5. 1 Sub-models used in the numerical modeling (Developed in this study)

Type	Sub-models	Description
Mechanistic modeling	Bubble velocity model	A mechanistic model based on the modified force balance model
	Departure diameter	A mechanistic model based on the modified force balance model
Numerical modeling	Bubble merger	Numerically solved
	Nucleation site distribution	Numerically distributed using the Monte-Carlo method
Experimental observation	Contact diameter	Based on Exp. Results, $d_w = 0.35D_b$
	Contact angle	Based on Exp. Results, α=20º, β=15º
	Bubble wake effect	Based on PIV Exp. Results, $L_{bubble} < 2D_b$

Table 5. 2 Sub-models used in the numerical modeling (closure models)

Mechanism	Sub-models	Authors	Description
Single-phase convection	Heat transfer coefficient	Jeon et al. (2015)	$T_{sub} < 40K$
Transient conduction	Area of influence	Amidu et al. (2018)	$K = 0.5$
Evaporation	Nucleation site density	Hibiki & Ishii (2003)	$P < 19.8MPa$
	Bubble growth	Yoo et al. (2018)	Mechanistic model, $T_{sub} < 13.5K$
	Bubble frequency	Cole (1967)	Requires departure diameter
	Bubble shape	Assumption	Always spherical
	Lift-off diameter	Basu et al. (2005)	$T_{sub} < 60K$
Bubble sliding	Drag coefficient	Newtons' Law (1997)	$C_d = 0.44$

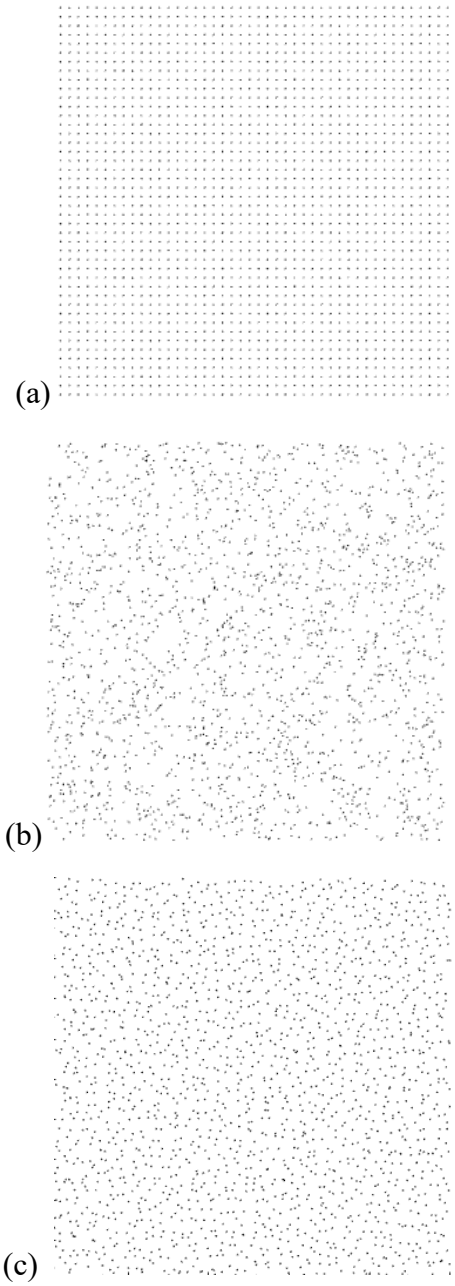

Figure 5. 1 Site distribution for D=50mm, 2,000 sites
(a) uniform (b) random (c) Latin hypercube

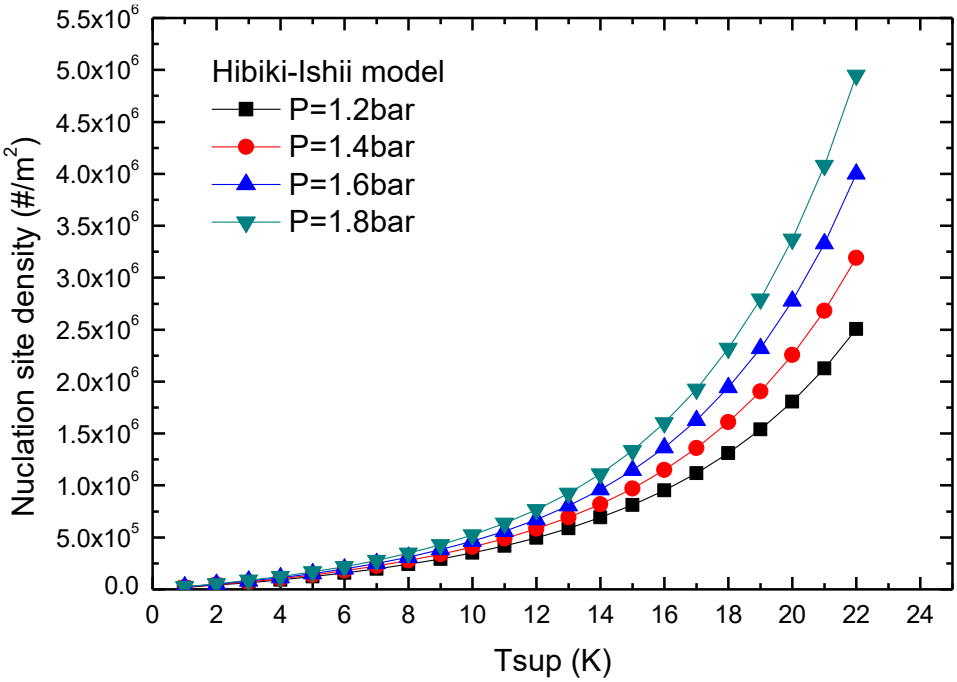

Figure 5. 2 Nucleation site density by surface superheat

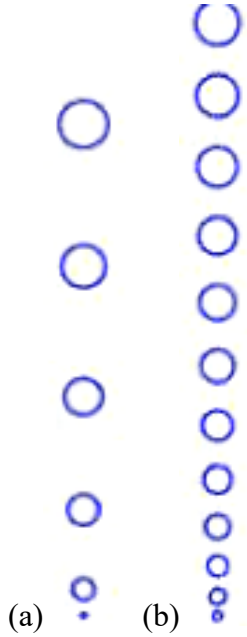

Figure 5. 3 Bubble generation for each nucleation site: (a) f=150#/s (b) f=300#/s

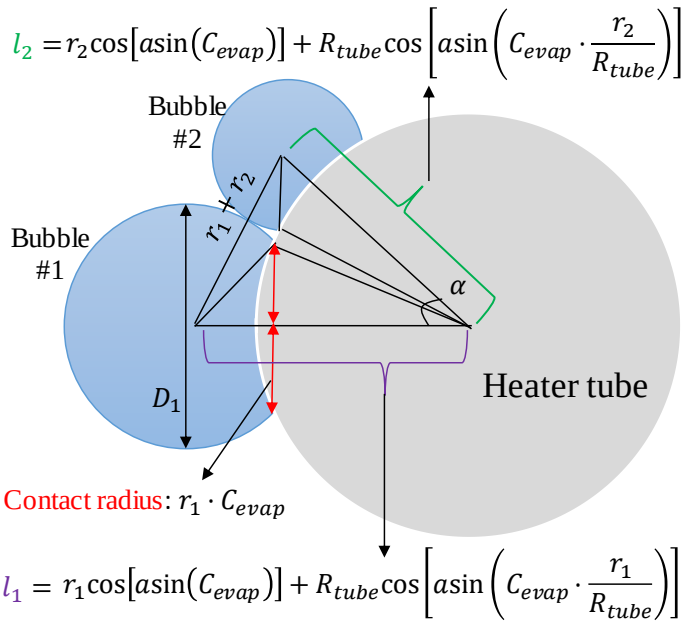

Figure 5. 4 Radial distance between bubbles

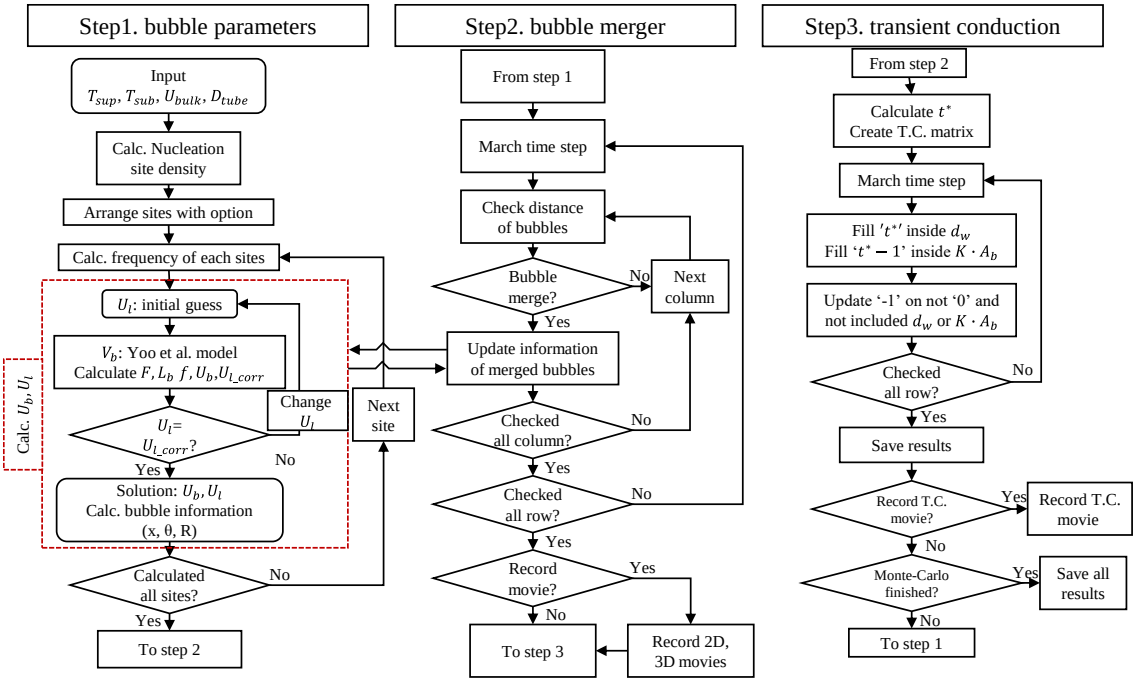

Figure 5. 5 Calculation process flowchart

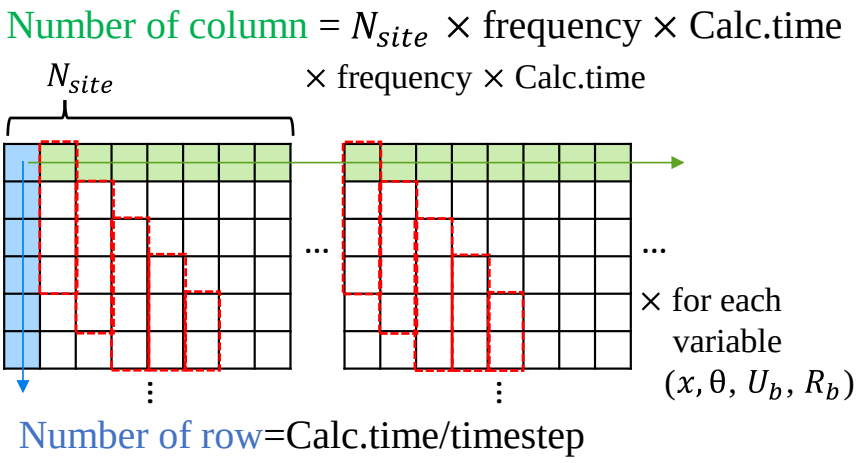

Figure 5. 6 Composition of the information matrix

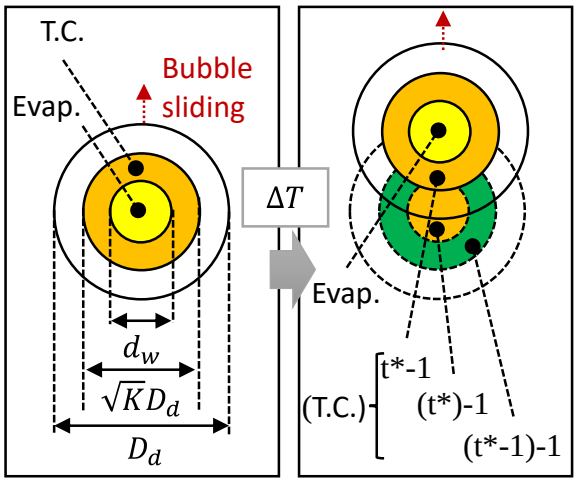

Figure 5. 7 Concept of transient conduction index

(a)

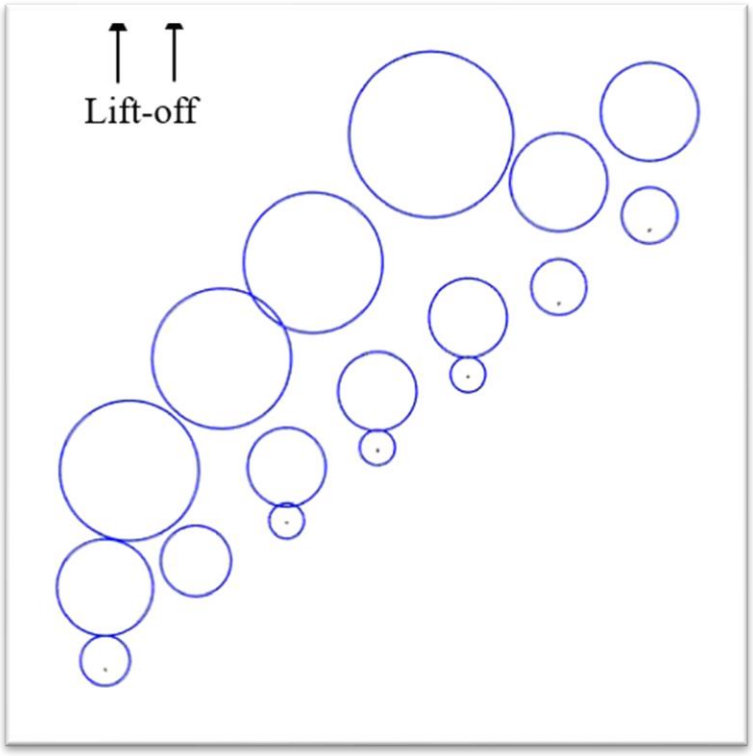

(b)

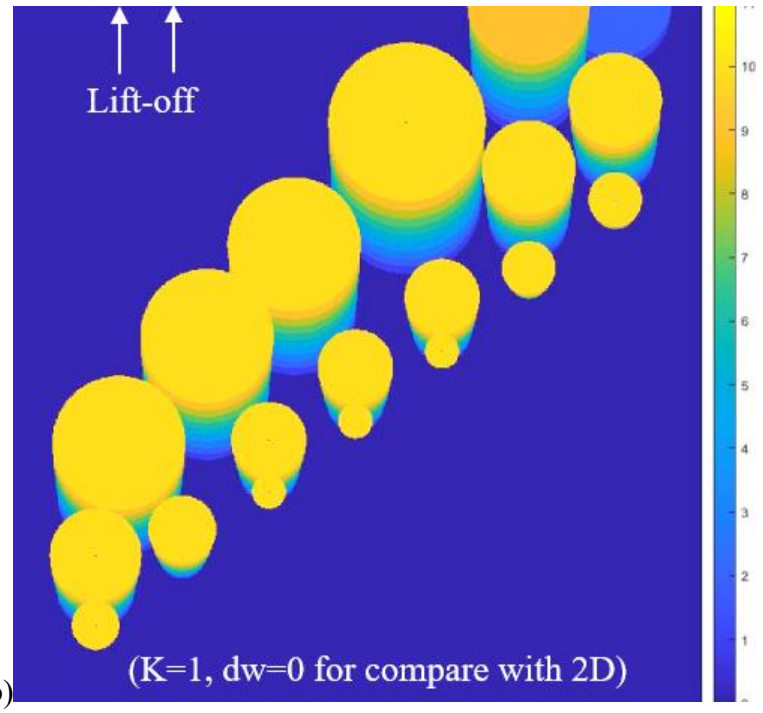

Figure 5. 8 Still image for (a) bubble information and (b) transient time matrix

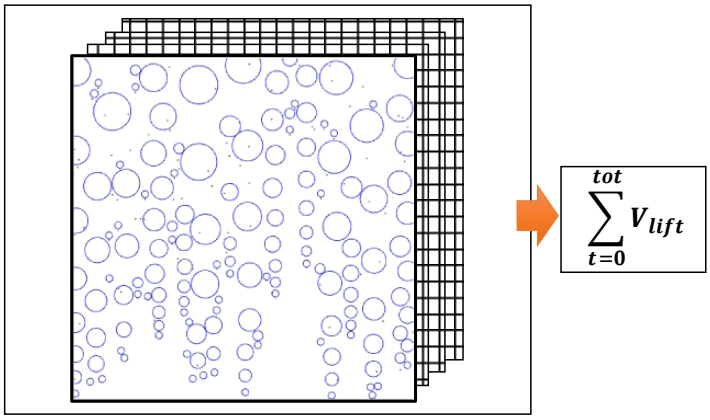

Bubble information x(t),y(t),r(t),U(t)

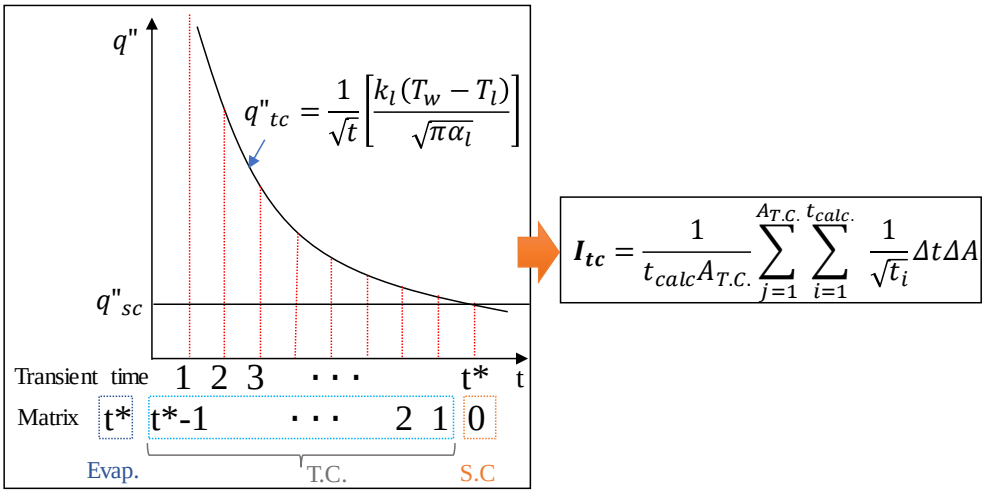

Calculate transient conduction intensity on transient conduction matrix

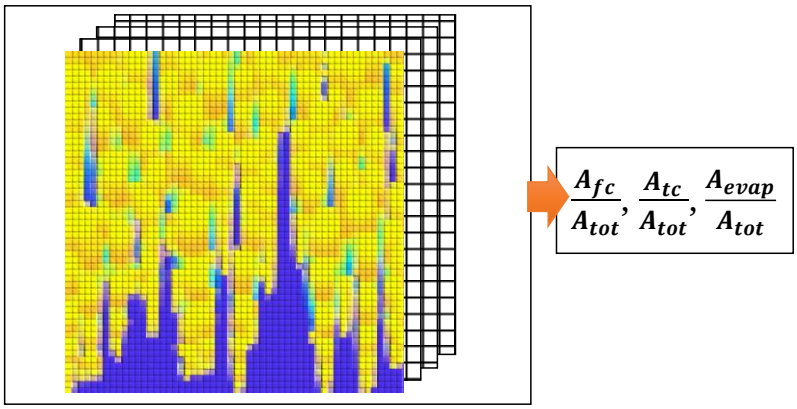

Transient conduction matrix

Figure 5. 9 Heat flux calculation element extraction

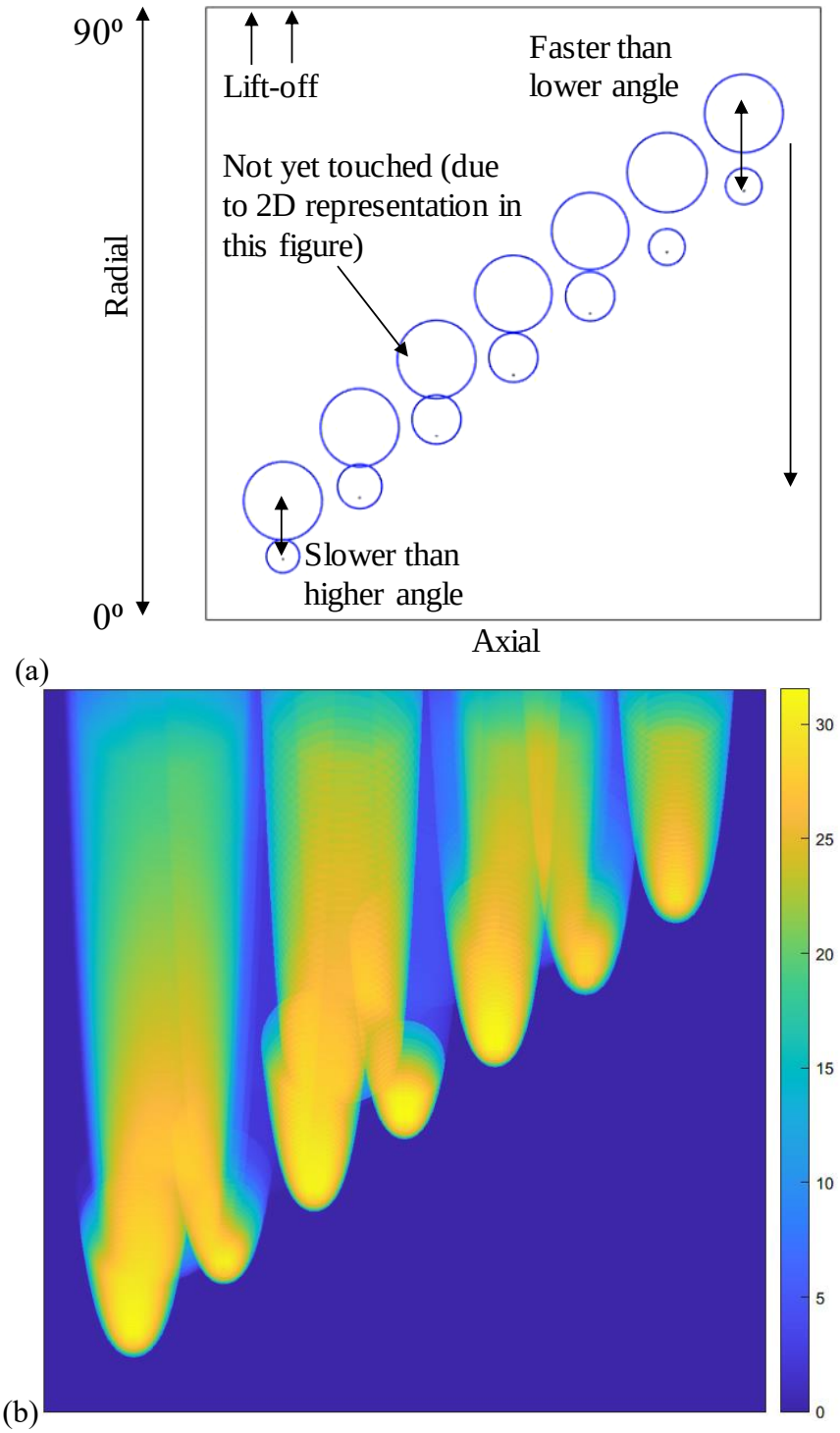

Figure 5. 10 (a) Still image of bubble tracking example and (b) time-averaged T.C. time matrix

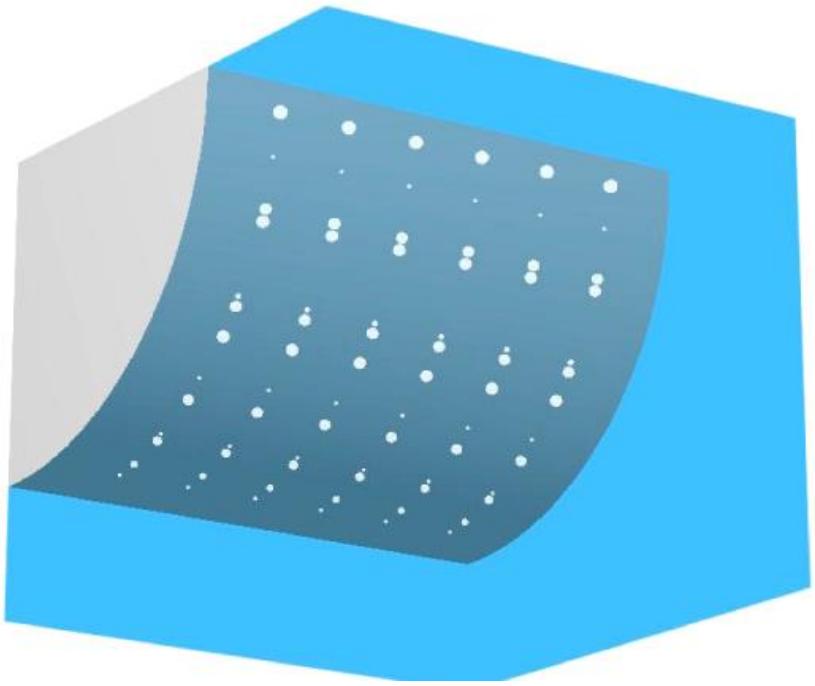

Figure 5. 11 3D results for lower side, Tsup=1K, Tsub=15K, uniform distribution

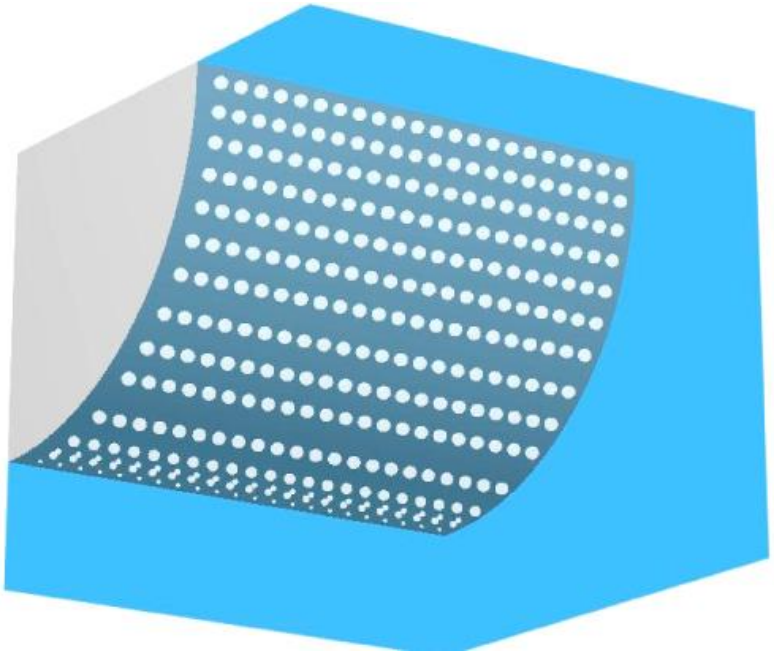

Figure 5. 12 3D results for lower side, Tsup=8K, Tsub=15K, uniform distribution

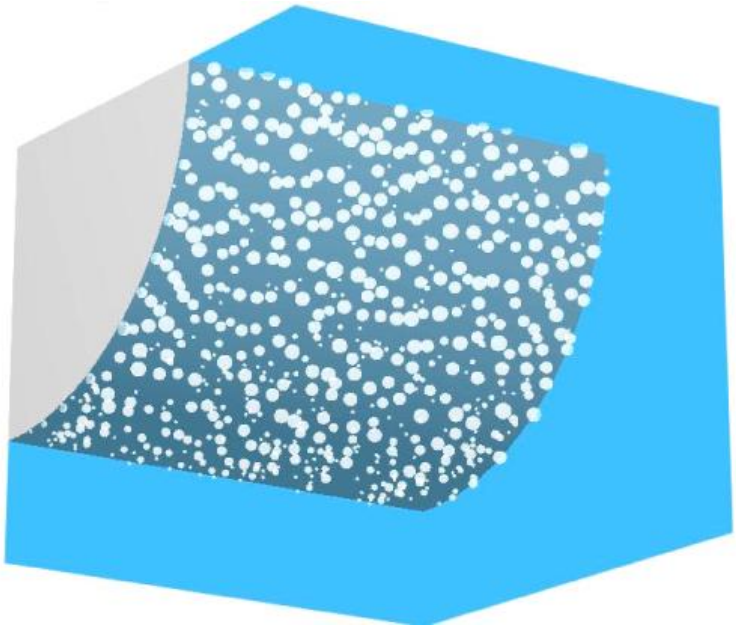

Figure 5. 13 3D results for lower side, Tsup=8K, Tsub=15K, random distribution

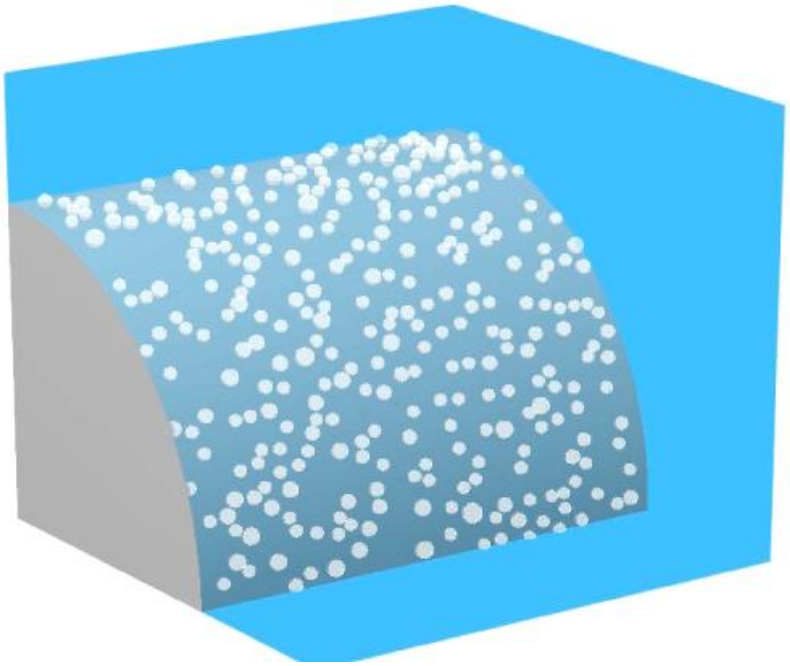

Figure 5. 14 3D results for upper side, Tsup=8K, Tsub=15K, random distribution

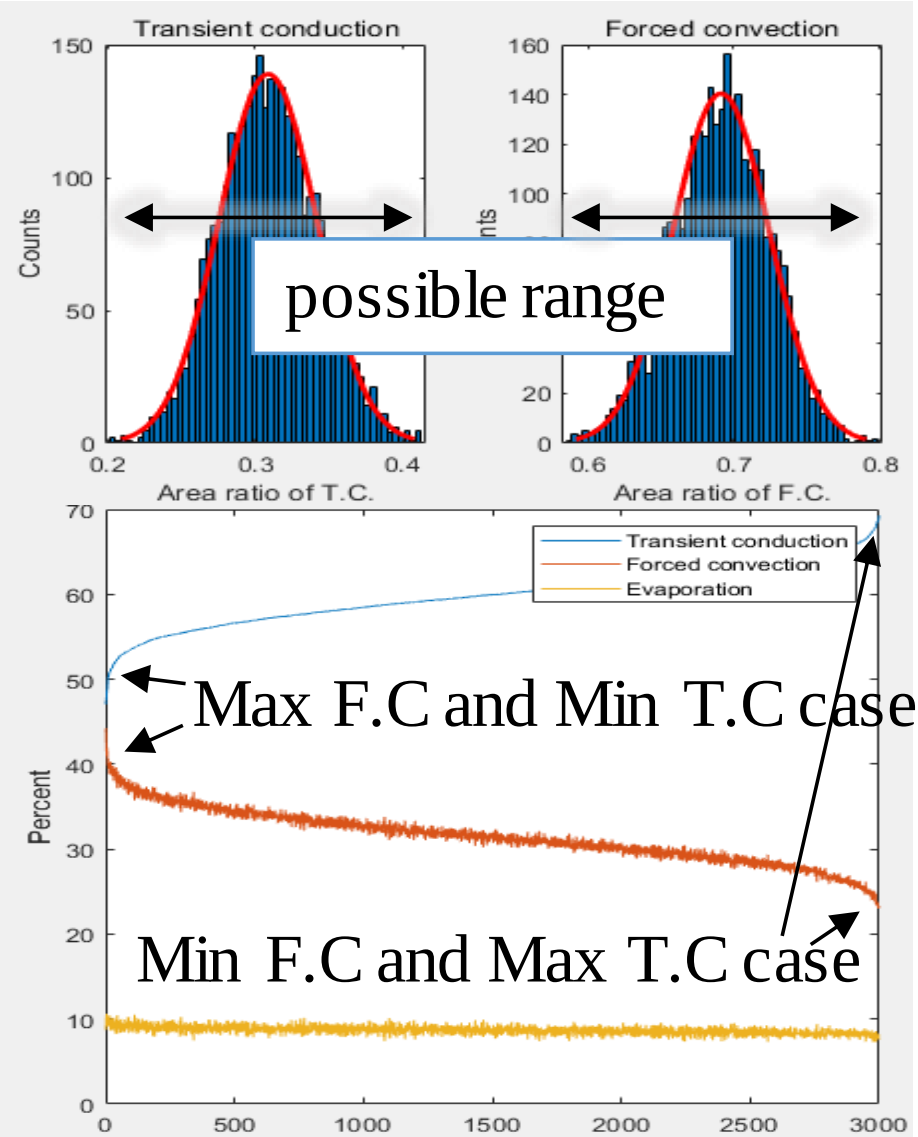

Figure 5. 15 Monte-Carlo simulation results (X 3,000 times)

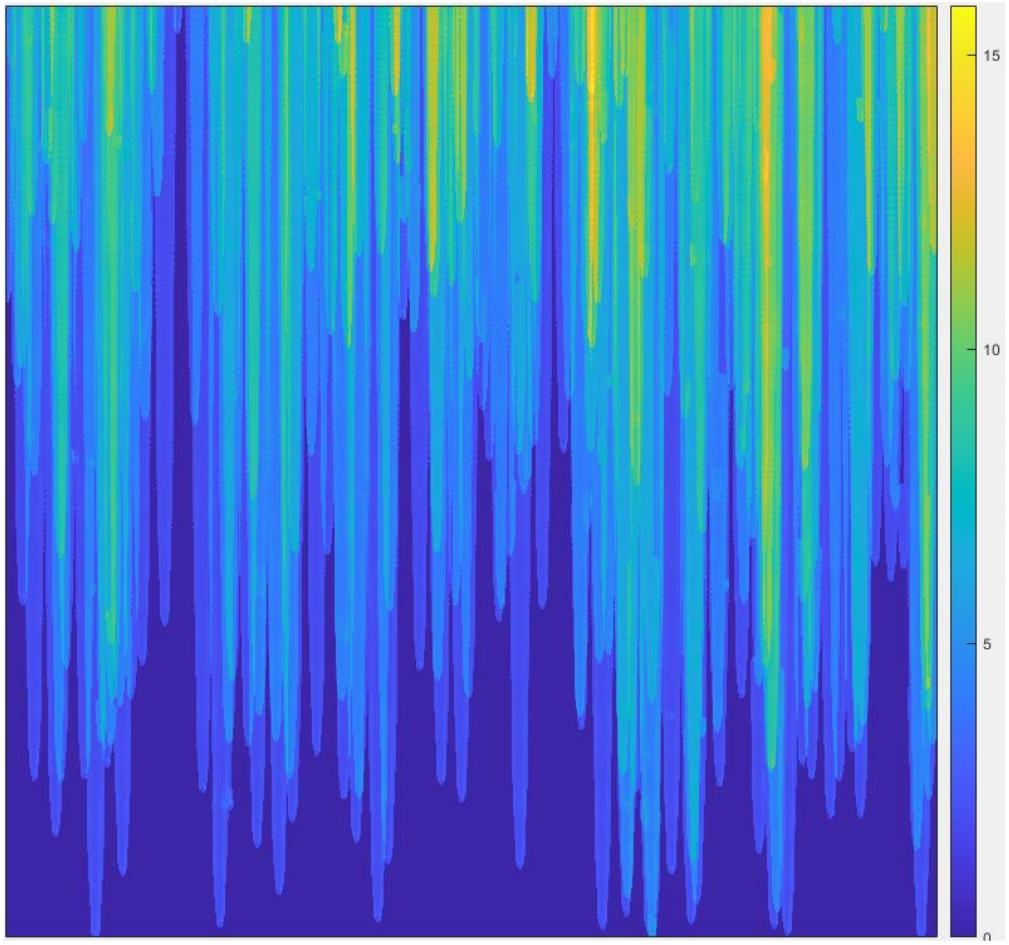

Figure 5. 16 Single random distribution calculation results of transient conduction time index

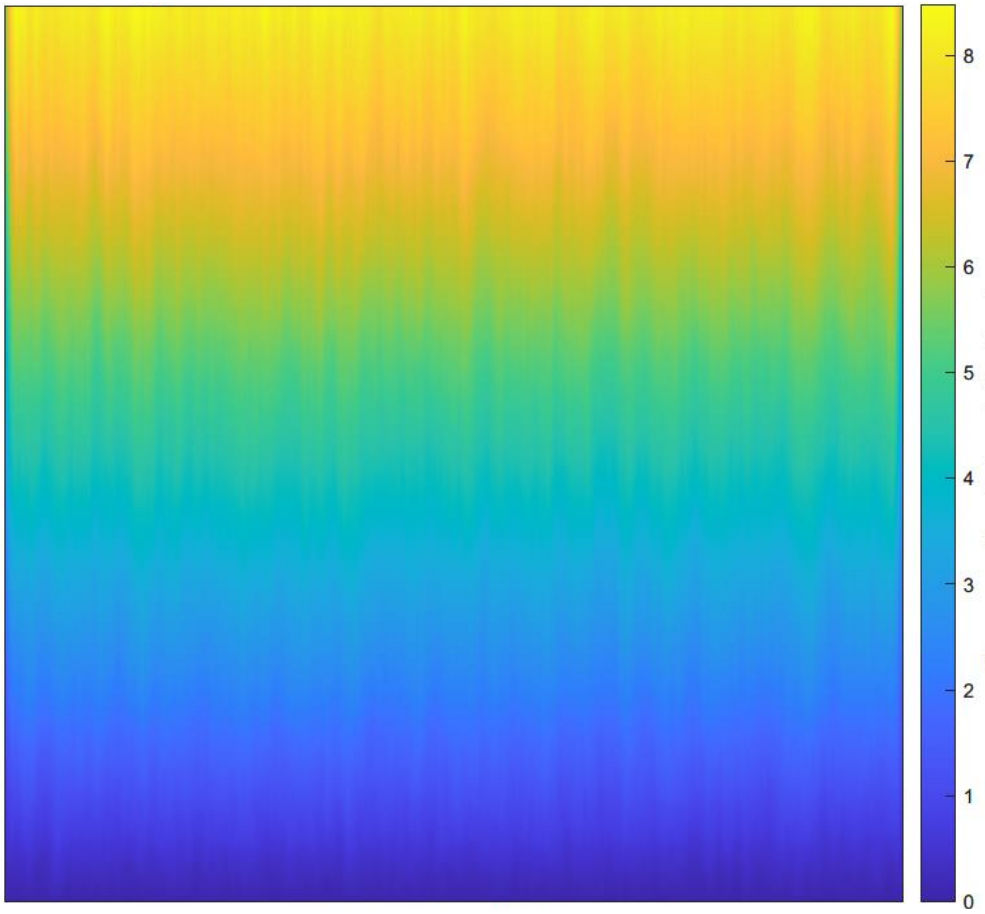

Figure 5. 17 Random distribution calculation results of transient conduction time index for 2,000 times averaged

Chapter 6

Calculation results and validation

6.1 Difference in calculation results according to site distribution

Figure 6. 1 and Figure 6. 2 are the calculation results of the distribution of the site using the (a) uniform and (b) random options, at Tsup=1K and Tsup=13K, respectively, with all other conditions equal. In the case of uniform distribution, since the sites are placed in a straight line where the bubbles slide up, it can be seen that transient conduction is concentrated and distributed only around this line. On the contrary, in the case of random distribution, it can be seen that the probability of sites is uniform in the entire area, and the degree is lower than that of the uniform case. Bubbles slide and rise upwards, so the upper part has greater transient conduction than the lower part. Figure 6. 3 shows one of the calculation results using each option. This case is calculated in the conditions D=33mm, saturation temperature and atmospheric pressure. Solid symbols represent the results from the random case, and hollow symbols are used for the uniform case. For all wall superheats, the random case has a slightly higher heat flux than the uniform case, and this trend is reversed as Tsup=16K. In the uniform case, the site is placed on the path that slides up, and the transient conduction is limited in a relatively small area compared to the random case, and the degree of transient conduction is relatively high because it occurs overlapping within this area. The degrees of

transient conduction are compared in Figure 6. 4. In the results, the total wall heat flux shows a difference of 0-50% $\pm$ 30% depending on the wall superheat. This difference is largely due to the difference in transient conduction. As shown in the figure, in the case of transient conduction, the degree of the random case is larger up to 80% $\pm$ 80% at Tsup=1K, and the difference gradually decreases as the wall superheat increases. This result is an average value of the results of 500 iterations, and it can be seen that, when Tsup=1K during 500 calculations, the difference between the maximum value of 160% and the minimum value of -10% varies depending on the case. This is because it depends on how the site is distributed, and in low heat flux cases, only a small number of sites exist on the heating area, so the value may vary greatly depending on the site distribution. On the other hand, in high heat flux, the number of sites is relatively large, and the area overlaps due to the large number of bubbles generated at each site, and there is not much room for change by arrangement.

Figure 6. 5 shows the ratio of the area occupied in the area according to the mechanisms in the total area. When this ratio is unity, heat transfer occurs by the corresponding mechanism in the entire area. Figure 6. 6 shows the transient conduction time index. This is the value of the transient conduction time term that occurs on the average in the area where the transient conduction occurs. If the value is large, a greater degree of transient conduction occurs in the same area. The theoretical maximum of this value is $1/\sqrt{timestep}$. Since the timestep is set to 0.001 second in this study, it is assumed that the bubble continues to pass in the area and the transient conduction continues to occur at the maximum value, which is the maximum value of 31.62. As shown in the figure, the random case has a lower I_{TC} value than the uniform case. This is because the site of the random case is spread

more evenly than the uniform case, so there is less overlapping transient conduction, and the random case has a smaller I_{TC} and a larger area.

Lastly, the Latin hypercube distribution has the advantage of being able to obtain heat flux results similar to random calculations with a small number of iterations, such as uniforms. In Figure 6. 7, Latin hypercube has almost the same ratio of each heat flux ratio and the total heat flux calculation as the random case. Also, as shown in Figure 6. 8, it was confirmed that the calculated result is almost the same as the random distribution's, and the range of results according to the randomness appears at half the level of the random case. This is because the Latin hypercube distribution is similar to the actual distribution, and at the same time, by placing the sites in a uniform grid, the randomness of the distribution is limited to the case where the overlapping is not extremely overlapping.

6.2 Validation of PASCAL experiment

The Korea Atomic Energy Research Institute evaluated the cooling performance of PAFS by performing an experiment using a PASCAL experiment (Figure 6. 9, Bae et al., 2012, Kang et al., 2012). The geometry and experimental conditions of the PASCAL experiment are shown in Table 6. 1. PASCAL simulated one U-shaped tube among the many U-tubes submerged in the PCCT as shown in Figure 6. 10. A thermocouple is installed inside the U-shaped tube as shown in the figure, and the nucleate boiling heat transfer amount and local heat transfer coefficient are experimentally derived. The experiment was conducted while maintaining a quasi-steady state at various subcooling temperatures and pressures. As shown in Figure 6. 11, the water surface rises due to the increase in temperature at the beginning of

heating, so the pressure and the temperature of PCCT gradually increase, and then nucleate boiling occurs. The pressure gradually decreases and the degree of subcooling continues to decrease until before the U-shaped tube reaches the surface.

Validation data was limited to only the results of measurement point 7 in the U-shape of the PASCAL experiment. As shown in Figure 6. 9, the PASCAL experiment has a U-tube located at the bottom of a water tank with a large area and a thin thickness. As the temperature of the water tank increases, natural convection occurs inside the water tank. However, the flow velocity distribution has not been measured in the experiment. Therefore, the measurement locations where natural convection can be minimized are 5 and 7 located in the center of the water tank, and the measurement location 5 is affected by the accelerated fluid due to the boiling bubbles and heating generated at the location 7. Therefore, only the result measured at position 7 of the U-shaped measurement location was used. The heat transfer prediction at the remaining measurement points can be compared by estimating the local fluid velocity through computation using CFD or multidimensional system codes. However, due to the mechanistic characteristics of this study, it is determined that the error due to the uncertain fluid velocity is very large compared to the error of the entire model, and the evaluation of predictive performance at these measurement points is excluded.

Figure 6. 12 to Figure 6. 15 show the results of the validation of the PASCAL experiment through the developed model in this study. Each figure shows the heat flux according to the mechanism and the total heat flux. Although the wall superheats of the PASCAL experiment were limited to a rather small range, it was confirmed that the model predicts the overall heat flux well despite the complicated phenomenon of simultaneously decreasing pressure and subcooling. The overall

heat transfer prediction performance of the PASCAL experiment was evaluated in Figure 6. 14, and it was confirmed that all the predicted values were within ±12%.

6.3 Validation of various tube diameters through other studies

Table 6. 2 shows the characteristics of horizontal tube boiling experiments for validation. These experiments were carried out using a horizontal tube at saturation temperature and atmospheric pressure, and each experiment differs somewhat in surface material and surface roughness.

The experiment by Cieslinski & Kaczmarczyk (2015) was conducted in a horizontal tube with a diameter of 10.67 mm. This study deals with pool boiling of water–Al2O3and water–Cu nanofluids on porous coated, horizontal tubes. Tubes were commercially available stainless-steel tubes and polished with the abrasive compound. So, the surface roughness was estimated as $R_a = 0.06\mu m$ by use of a PGM-1 surface analyzer.

The experiment by Shoghl & Bahrami (2013) was conducted in a horizontal tube with a diameter of 10.67 mm. The experimental investigation has been performed with different heat flux and concentrations of nanoparticles and surfactants. CuO and ZnO water-based nanofluids are used and sodium dodecyl sulfate (SDS) is used as a surfactant. Surface roughness was estimated as $R_a = 0.15 - 0.19\mu m$ by use of an Atomic Force Microscopy (AFM).

Sayahi et al. (2015) was conducted on a SUS heater with a diameter of 10.67 mm. The experimental investigation has been performed by the addition of nanoparticles and surfactants to the base fluid which are potential methods for

enhancing the pool boiling heat transfer coefficient. the surface roughness of the test heater is determined to be $R_a = 0.15\mu m$ by AFM method.

Qiu & Liu (2004) was conducted on a copper heater with a diameter of 18 mm. This study experimentally investigated the effects of tube spacing, positions of tubes, and test pressures on the boiling heat transfer of water in restricted spaces of the compact staggered bundles consisting of smooth horizontal tubes. The test tubes are copper tubes with an outside diameter of 18 mm, an inside diameter of 12 mm and a length of 100 mm (actual effective heating length is also 100 mm) and it was heated with a cartridge electric heater located inside the tube.

Nelson & Burnside (1985) was conducted on an aluminum alloy heater with a diameter of 19 mm. This study describes a study of boiling from a bundle of tubes in the n-nonane/water system. The bundle consists of 12 x 56 mm tubes, 19mm in diameter, on a 25.4 mm square pitch. The boiler tubes and shell were made of aluminum alloy construction.

Gupta et al. (1995) was conducted on a SUS (AISI 304) heater with a diameter of 19.05 mm. An experimental investigation has been carried out to determine the local forced convective boiling heat transfer coefficient in small tube bundles consisting of horizontal tubes in a vertical column arranged in a large channel under low cross-flow velocities in saturated distilled water at atmospheric pressure.

Das et al. (2003) was conducted on a SUS heater with a diameter of 20 mm. This study focuses on an experimental study of pool boiling in water–Al2O3 nano-fluids on horizontal tubes. In this experiment, surface machine drawn stainless steel heaters of different diameters have used. The surface characteristics of the heater were measured using a profilometer having a diameter tip of $2\mu m$ and a sensitivity of $0.02\mu m$. The major parameter for characterisation of surface roughness is Ra

and the measured value is $R_a = 0.37 - 0.45\mu m$.

Shakir (1987) was conducted on a SUS heater with a diameter of 22.2 mm. In this study, a comprehensive experimental study in nucleate pool boiling of binary mixtures was carried out to investigate the effects of mixture composition on boiling incipient, deactivation superheats and heat transfer coefficients. Binary mixture systems, i.e. methanol-water, ethanol-water, propanol-water, and ethanol-benzene were tested on this heater surface. Before the experiment, the surface was treated with a 320-grade emery paper.

Hsieh & Weng (1997) was conducted on a copper heater with a diameter of 27 mm. In this study, measurements of pool-boiling heat transfer coefficients in distilled water and R-134a/oil mixtures are extensively studied for a smooth tube.

Rajulu et al. (2004) was conducted on a SUS heater with a diameter of 33 mm. In this study, the pool boiling of acetone, isopropanol, ethanol, and water at atmospheric pressure was carried out on a plain tube, and five different reentrant cavity (REC) heating tubes.

From Figure 6. 18 to Figure 6. 24, the verification results of the above-mentioned experiments are shown according to the heater diameter. Results predicted using the model of Sateesh, another mechanistic wall heat transfer model, confirmed that the heat flux was relatively overestimated. This is because the sub-models and assumptions in Sateesh's model are somewhat different from the actual phenomenon. The evaluation results for the entire experiment are shown in Figure 6. 25. In this study, the predicted performance of the calculation results uniformly underestimated the heat flux with an error of -8% on average, and ranged from -37% to +21% with 2-sigma. In addition, the predicted performance of the randomized calculation results slightly overestimated the heat flux with an error of +5% on

average and ranged from -32% to 44% with 2-sigma. Lastly, when predicting with Sateesh's model, on average, the heat flux was overestimated by 92% or more, and it was greatly overestimated that the range of 2-sigma reached +245%. The reason why Sateesh's model overestimates is that the total amount of transient conduction is overestimated while using the area of influence K value of 1.8.

Through these results, it was confirmed that the horizontal tube heat transfer model developed in this study can predict heat transfer better than conventional approaches or models.

6.4 Sensitivity studies

The sensitivity of the calculated wall heat flux by the change of each major sub-model was studied. In this study, the wall heat transfer prediction model was completed using the sub-models shown in Table 5. 1 and Table 5. 2. However, the difference in the predicted values of the model that may occur depending on the difference of the sub-models. In this chapter, the sensitivity of the developed model, and the prediction range according to sub-models was confirmed.

6.4.1 Bubble frequency

As shown in Figure 6. 28, the predicted wall heat flux does not depend greatly on the bubble frequency. The reason for this is that even if new bubbles are continuously generated in a short time interval since they are merged with the earlier generated bubble, the effect does not appear significantly. The wall heat flux increases slightly with increasing bubble frequency, and the difference is greater at

high wall superheat. This is because the effect of mitigation is reduced because, at high wall superheat, the preceding bubble is rapidly departed from the nucleation site and slides faster due to the increase in bubble growth rate. This is a result that can be reflected due to numerical modeling, unlike conventional analytical methods that simply multiply the bubble frequency.

6.4.2 Area of influence

Figure 6. 29 shows the change in the predicted wall heat flux by the area of influence, K. The K value represents the area ratio of heat transfer enhancement which occurs due to the sliding of the bubbles. As a result of sensitivity analysis, it was confirmed that the predicted heat flux was greatly influenced by the K value. As an extreme comparison case, the K value was set to 100 so that even with a small number of bubbles, the entire heat transfer area was affected by transient conduction. In particular, it was confirmed that the effect is greater at a low wall superheat, and the difference decreases as it goes to a high wall superheat. At a high wall superheat, there is a relatively small difference in the change of the K value since the heat transfer enhancement by the transient conduction is occurring in the entire wall surface by more bubbles already. Even so, the results showed that the wall heat flux prediction performance was highly dependent on the K value. This is due to the fact that the current transient conduction equation uses the K value as a simple constant. The effects of the bubbles are not simply expressed as a constant. Also, when considering the principle of the transient conduction, the affected area ratio must be influenced by local wall temperature, fluid subcooling, superheated layer formation, and bubble generation frequency. Therefore, it was confirmed that the transient

conduction of the wall needs to be improved by accurately reflecting the actual physical phenomenon in the future.

6.4.3 Contact diameter

In the previous section 3.3.2, experimental results and analysis of the contact diameters are presented. As a result of the experiment, it was confirmed that the ratio of the contact diameter to the bubble diameter starts from about 0.7 to 0.9 immediately after creation and gradually decreases linearly with time. In modeling, the experiment results were averaged over time, and a value of 0.35 times the bubble diameter was used. In order to confirm the difference due to the change of this value, the values were changed with 0.1 times (-70%) and 0.7 times (+100%) to confirm the difference between the predicted values of the total wall heat flux. Figure 6. 30 shows the result of the predicted value according to the change in the contact diameter ratio. As the contact diameter ratio increases, the fraction of the transient conduction decreases over the entire heating surface, and the fraction of microlayer evaporation increases. At this time, since the heat flux used to generate the microlayer evaporation is relatively small compared to the transient conduction, the wall heat flux prediction value decreases.

6.4.4 Coalescence time

In this study, the bubbles were numerically modeled to merge into one bubble as soon as they touched each other. However, in actual bubble merging, there is a time required from the time of contact to merging into a single bubble, and this is

called coalescence time. According to Owoeye (2015), coalescence time is about 6 ms. Also, depending on various conditions, this value may be different. Therefore, the difference in the predicted results of wall heat flux by arbitrarily controlling the coalescence time were examined. As shown in Figure 6. 31, ten nucleation sites were created on the wall, each bubble was changed into five merged bubbles, and coalescence time was given as 0, 6, and 16 ms, respectively, to examine the difference between the predicted wall heat flux and the bubble velocity. To make it easy to compare the results, the wall superheat was set to 20K to increase the size of the bubbles, and calculation was performed under the conditions of saturation temperature. As a result, at 6 ms coalescence time, the wall heat flux increased by 0.0099%, and the bubble velocity decreased by 1.77%. In addition, at 16 ms coalescence time, the wall heat flux increased by 0.0727% and the bubble velocity decreased by 3.88%. This is limited to very large bubble conditions with a superheat of 20K, and on the actual heating wall, the coalescence time is overwhelmed by numerous bubbles. Conversely, at lower wall superheats, the size of bubbles is small, so the effect of coalescence time is not significant.

Table 6. 1 Parameter of the PASCAL Facility (Kang et al., 2012)

Parameter		Values
PCHX	Number of U-tubes	1
	Tube length [m]	8.4
	Tube inner diameter [mm]	44.8
	Tube outer diameter [mm]	50.8
	The inclination of the tube	3°
PCCT	Pool height [m]	8.9
	Pool length [m]	6.7
	Pool width [m]	0.112
	PCCT pressure [MPa]	0.1

Table 6. 2 Description of other studies in various tube diameters

Authors	Tube diameter [mm]	Heated length [mm]	Tube material	Surface roughness (Ra) [μm]	Description
Cieslinski (2015)	10.67	100	SUS	0.06	Pool boiling experiment with water, Al2O3 and copper nanoparticles
Shoghl (2013)	10.67	99.1	SUS	0.15~0.19	Pool boiling experiment with ZnO and CuO water-based nanofluids
Sayahi	10.67	99.1	SUS	0.15	Pool boiling experiment for

(2016)					various nanofluids
Qiu (2004)	18	100	Copper	-	Pool boiling experiment for single tube and tube bundles
Nelson (1985)	19	-	Aluminum alloy	-	Pool boiling experiment for water/n-nonane for tube bundles
Gupta (1995)	19.05	190	SUS (AISI 304)	-	Pool boiling to low velocities forced convective boiling experiment, bundles
Das (2003)	20	-	SUS	0.37-0.45	Pool boiling experiment of various nanofluids
Shakir (1985)	22.2	190	SUS	-	Boiling experiment of methanol-water mixtures
Hsieh (1997)	27	330	Copper	-	Pool boiling experiment of water, R-134a and oil mixtures
Rajulu (2004)	33	218	-	-	Pool boiling of acetone, isopropanol, ethanol, and water

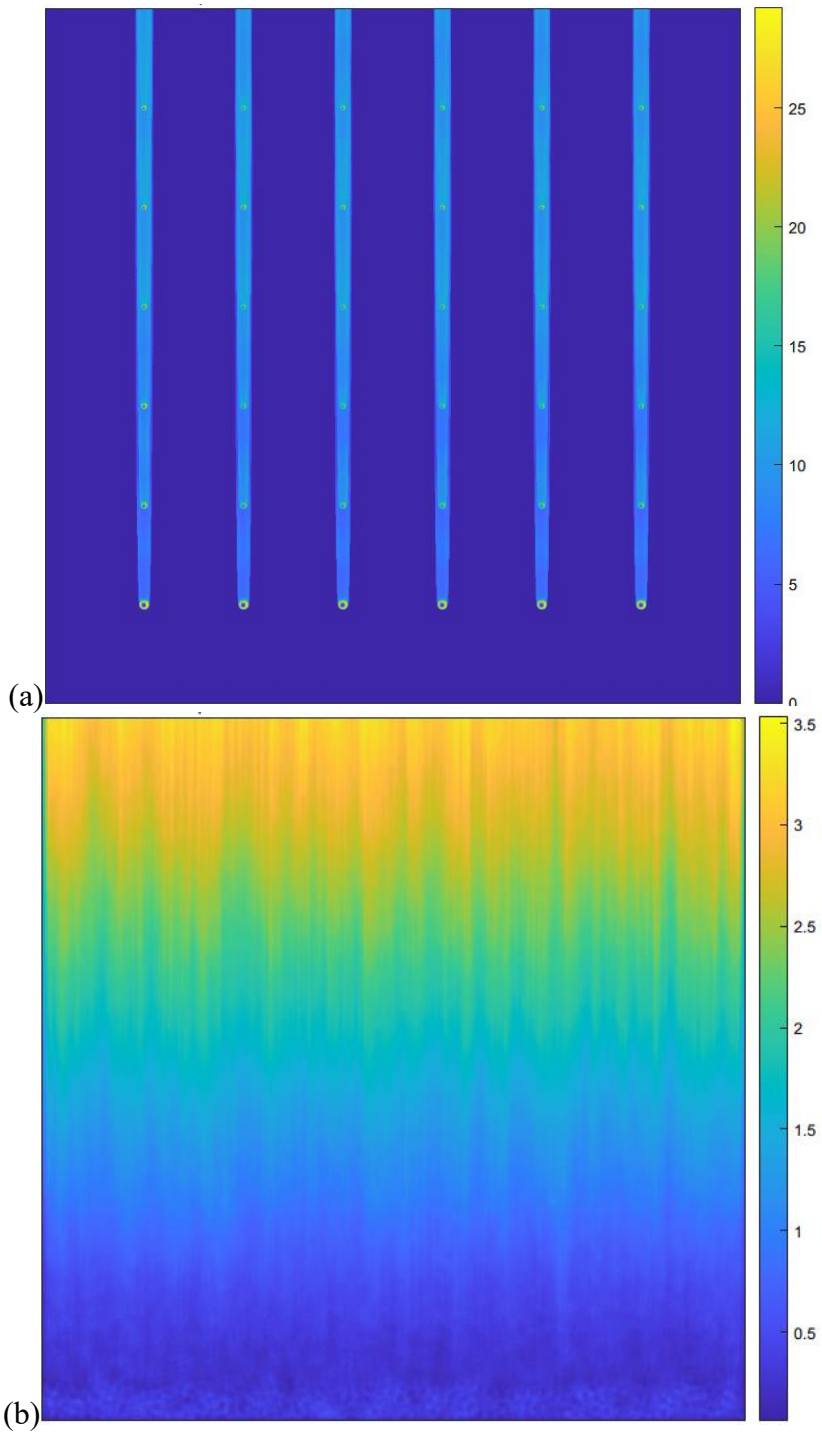

Figure 6. 1 Transient conduction matrix results:
(a) Tsup=1K, uniform, (b) Tsup=1K, random

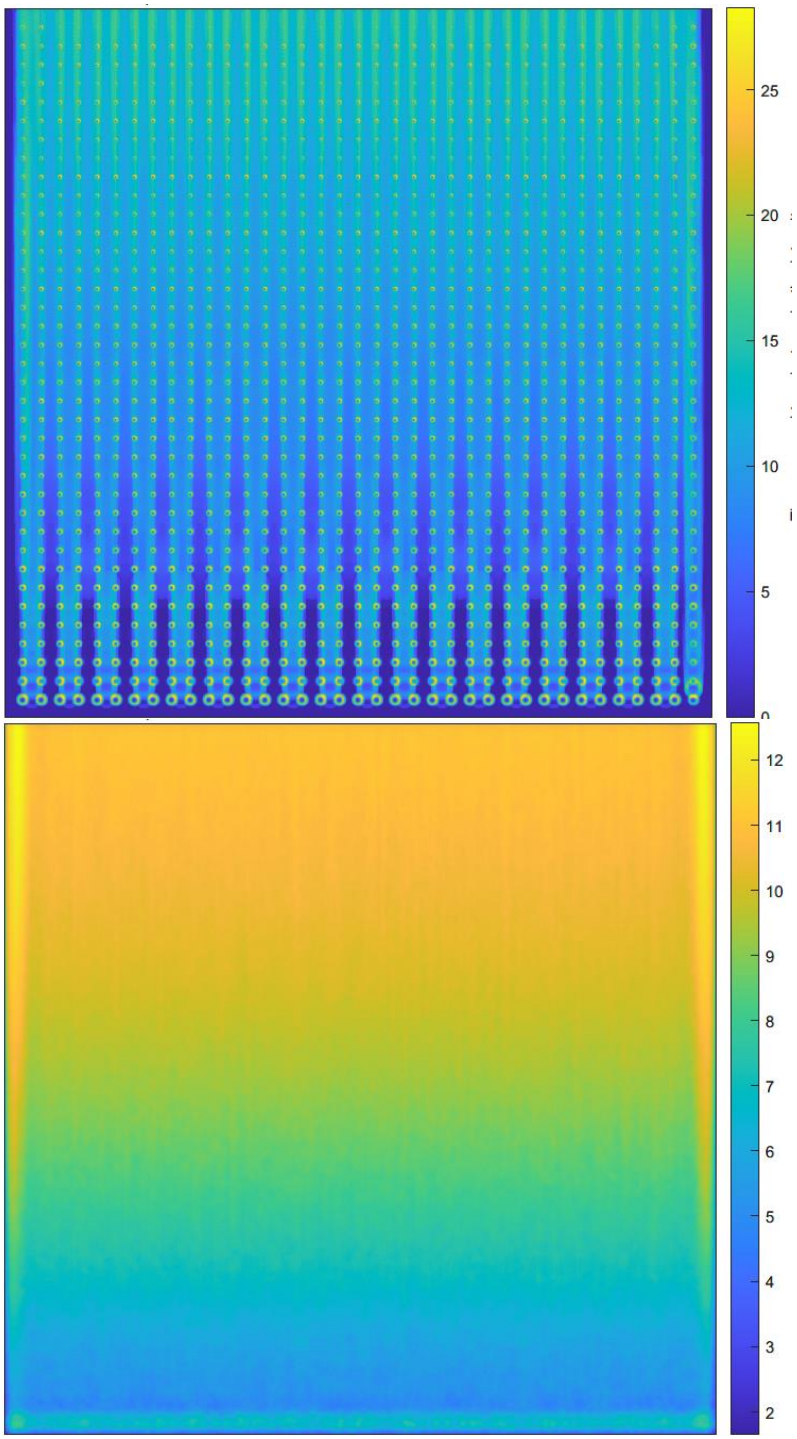

Figure 6. 2 Transient conduction matrix results:
(a) Tsup=13K, uniform, (b) Tsup13K, random

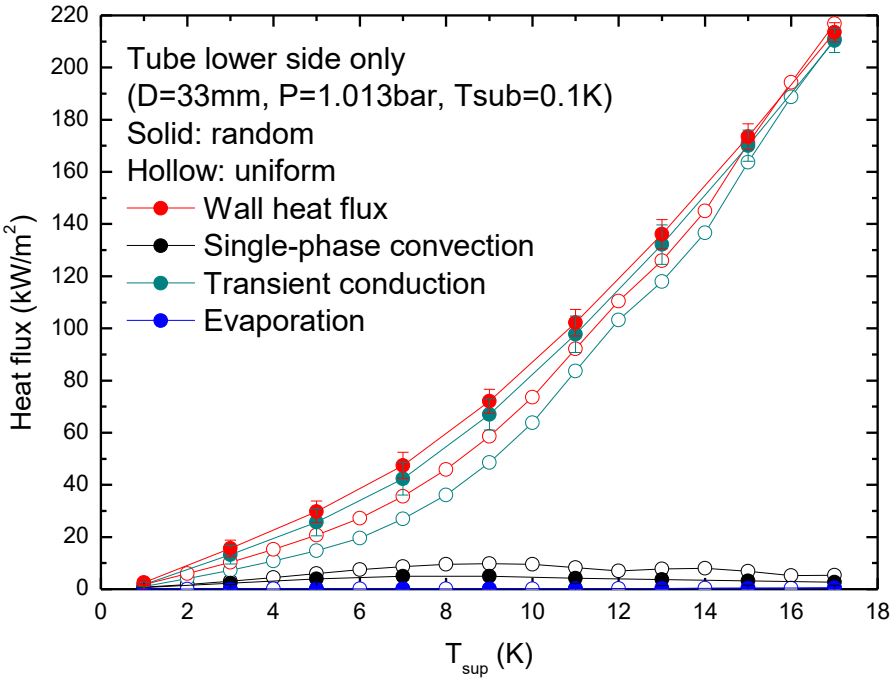

Figure 6. 3 Heat flux calculation results for surface superheat (D=33mm, P=1.013bar, Tsub=0.1K)

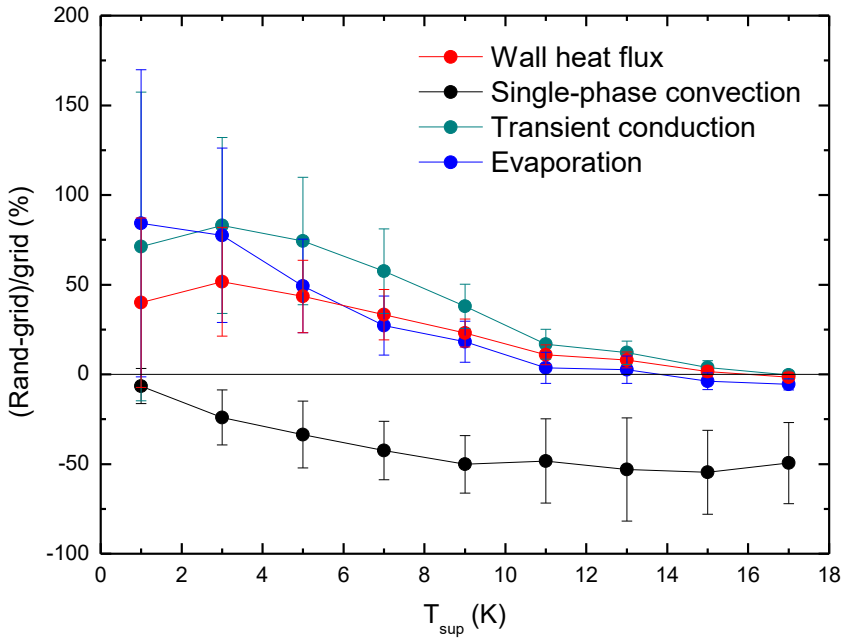

Figure 6. 4 Calculated heat flux ratio of random sites over uniform sites (D=33mm, P=1.013bar, Tsub=0.1K)

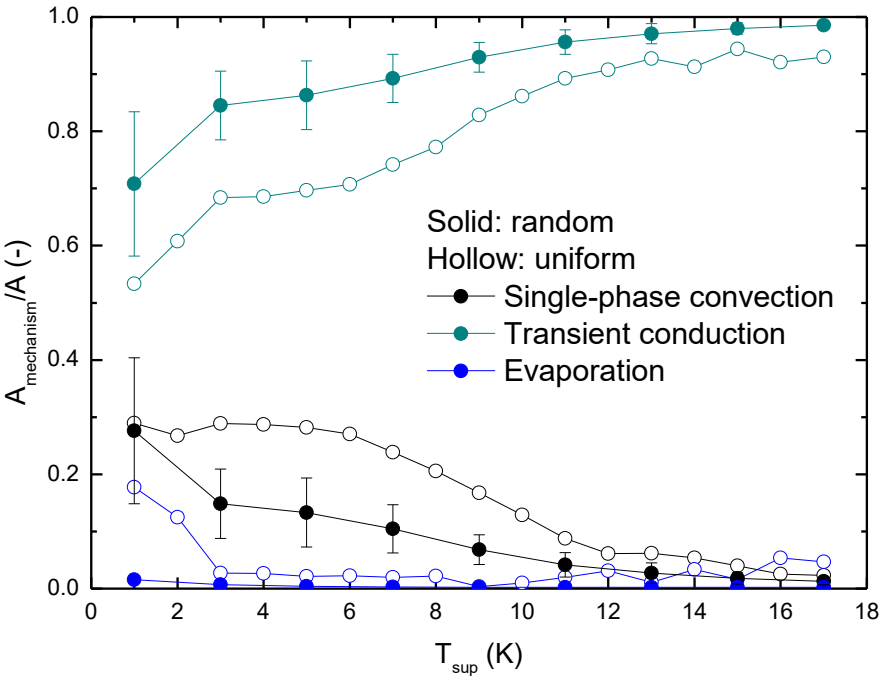

Figure 6. 5 Calculated occupied area ratio for each mechanism (D=33mm, P=1.013bar, Tsub=0.1K)

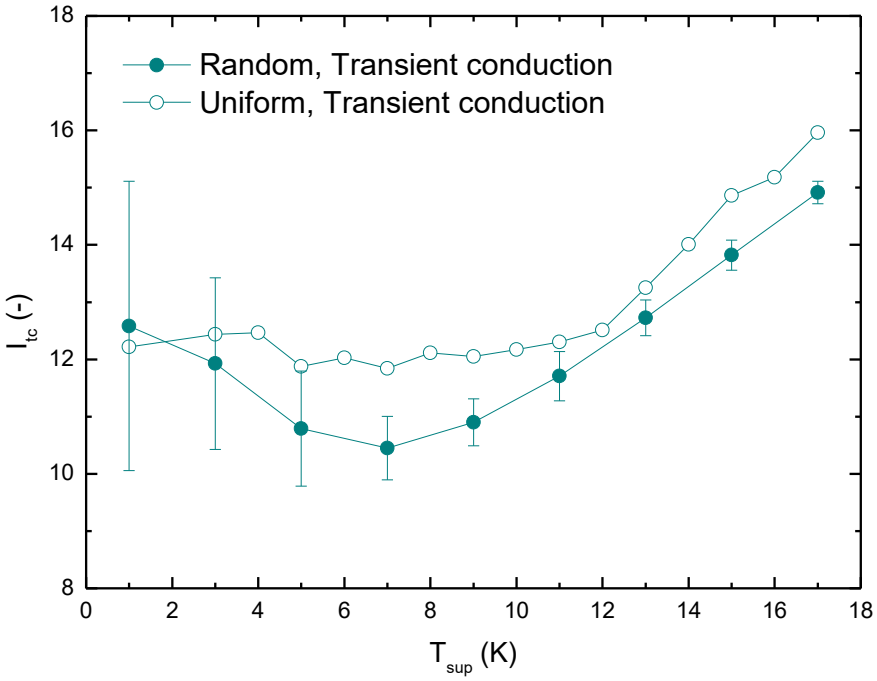

Figure 6. 6 Calculated transient conduction time index (D=33mm, P=1.013bar, Tsub=0.1K)

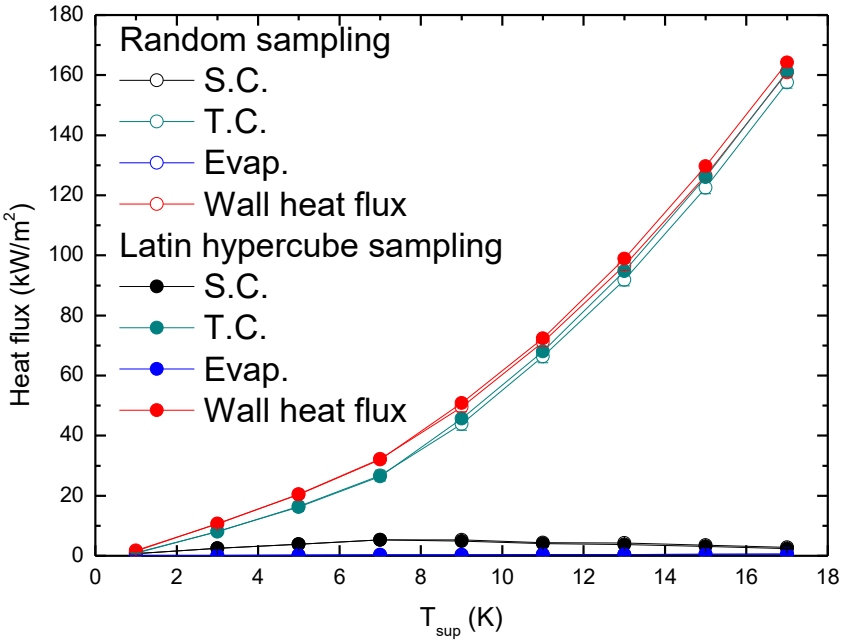

Figure 6. 7 Comparison of the heat flux calculation results of random and Latin hypercube (D=33mm, P=1.013bar, Tsub=0.1K, Lower side only)

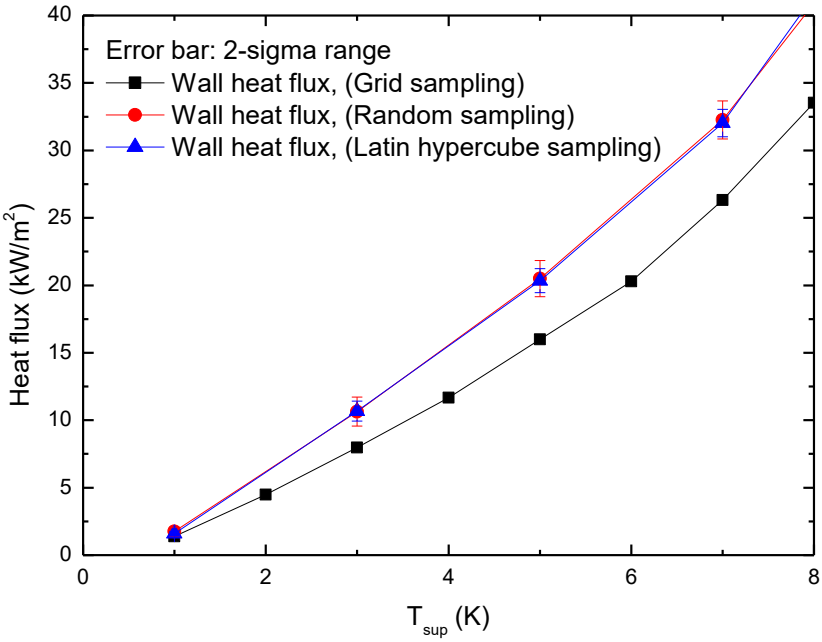

Figure 6. 8 Comparison of the heat flux calculation results of the grid, random and Latin hypercube (D=33mm, P=1.013bar, Tsub=0.1K, Lower side only)

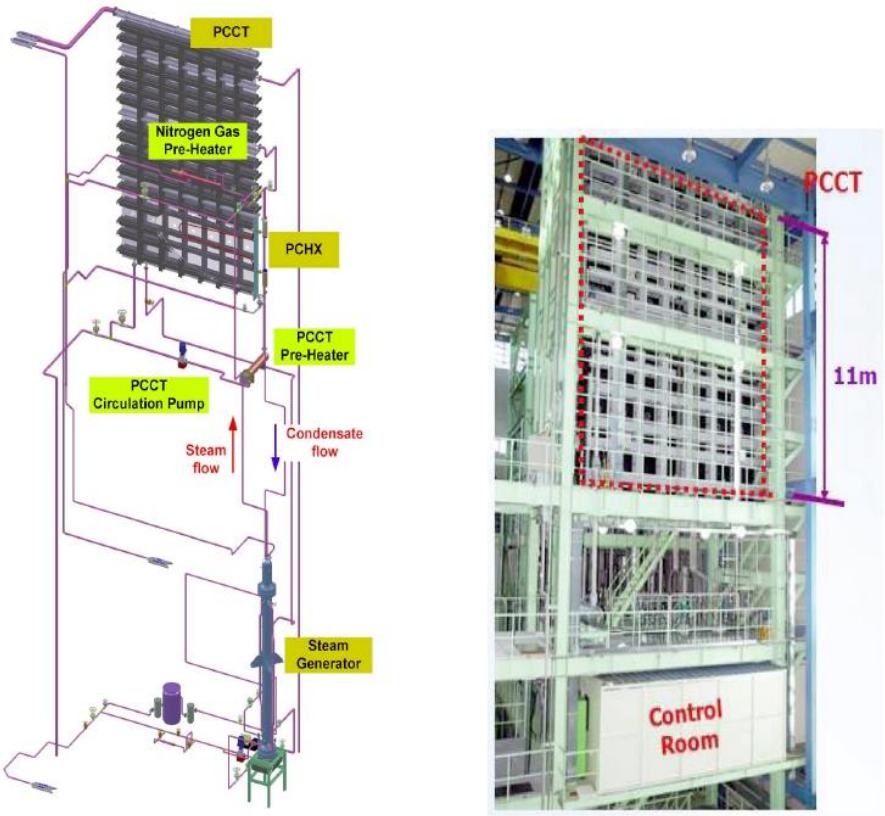

Figure 6. 9 Schematic diagram and photograph of the PASCAL (Kang et al., 2012)

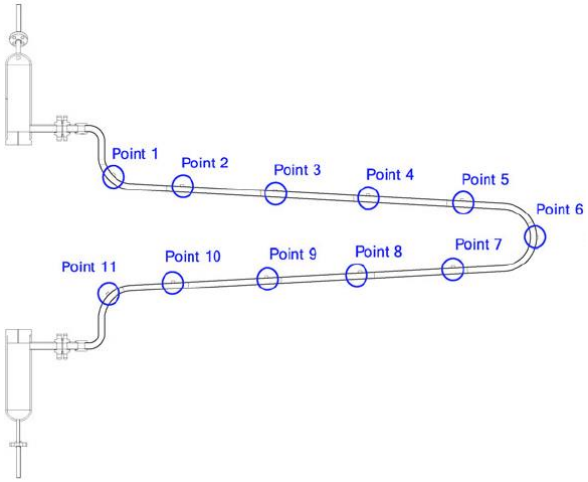

Figure 6. 10 Measuring location along the U-tube in the PASCAL facility (Bae et al., 2012)

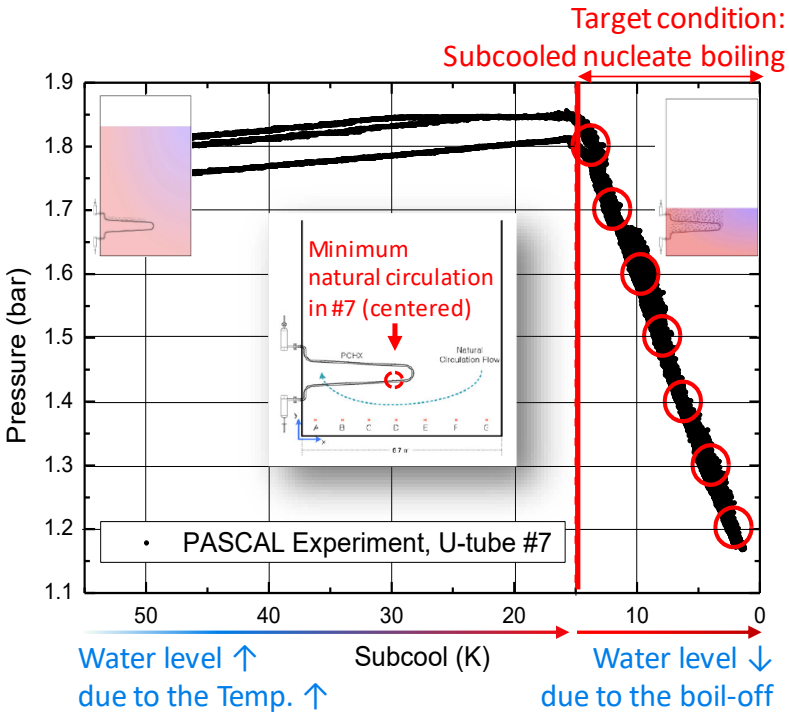

Figure 6. 11 Validation conditions to identify pressure & subcooling effects (PASCAL exp.)

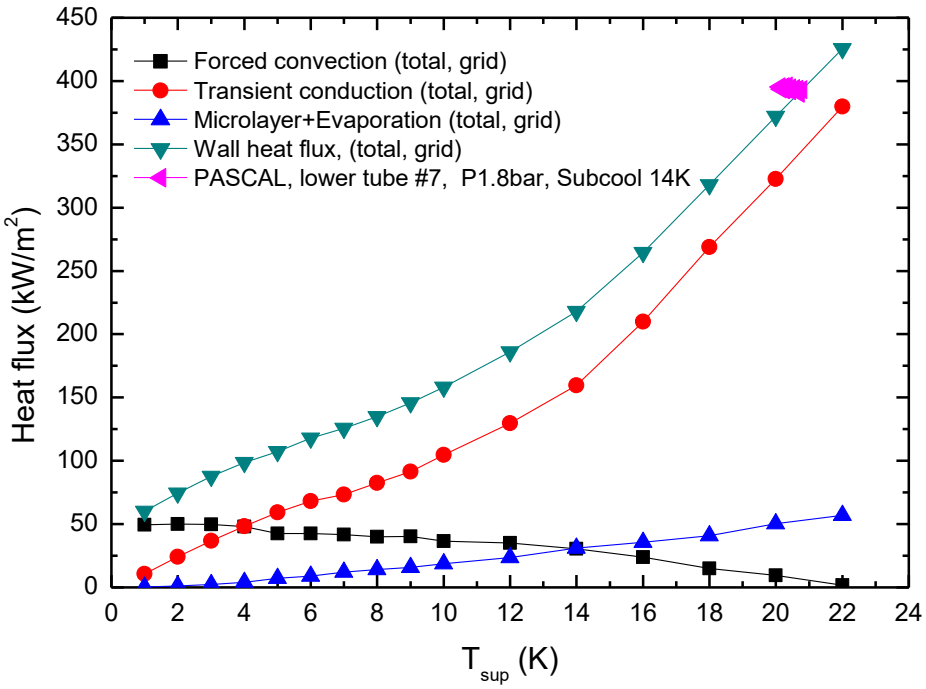

Figure 6. 12 Heat flux vs. wall superheat (P=1.8bar, Tsub=14K)

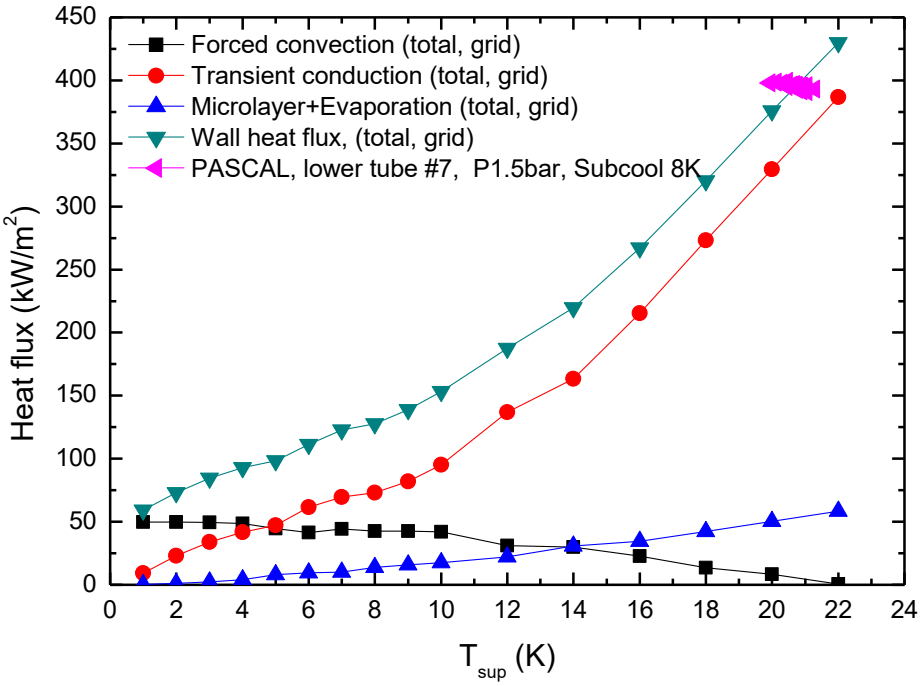

Figure 6. 13 Heat flux vs. wall superheat (P=1.5bar, Tsub=8K)

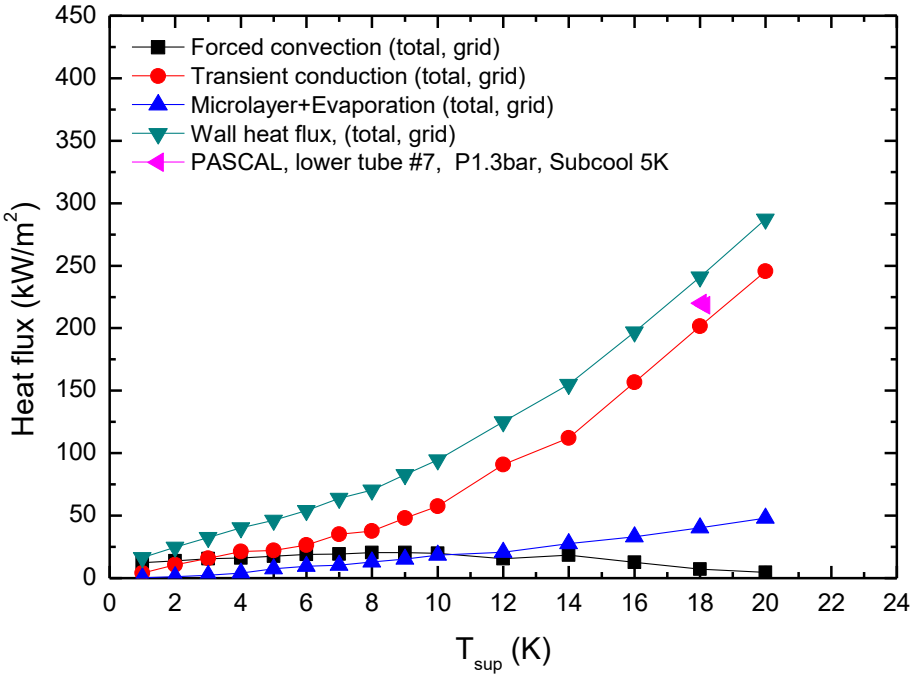

Figure 6. 14 Heat flux vs. wall superheat (P=1.3bar, Tsub=5K)

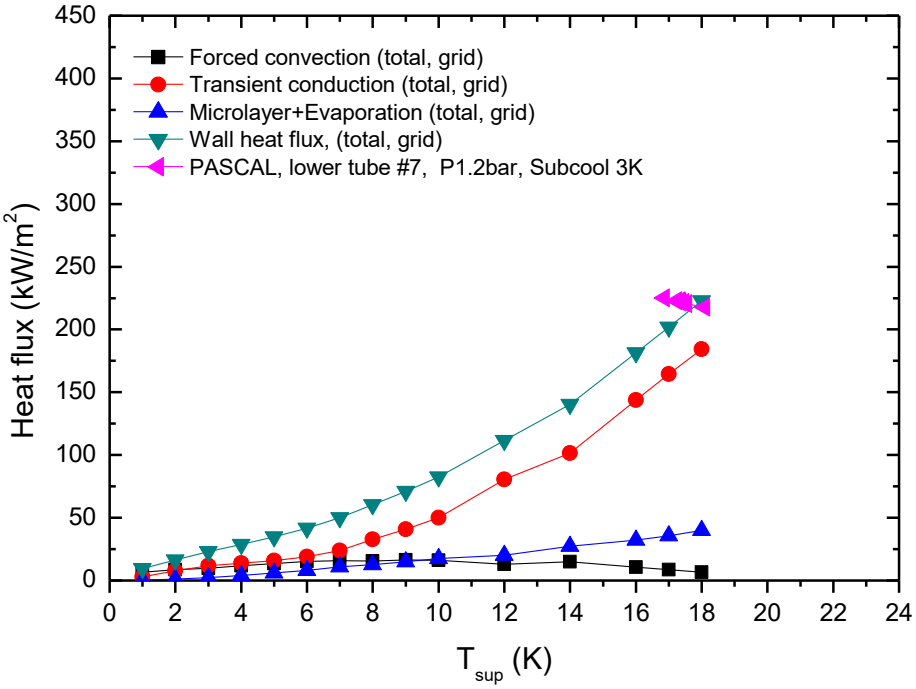

Figure 6. 15 Heat flux vs. wall superheat (P=1.2bar, Tsub=3K)

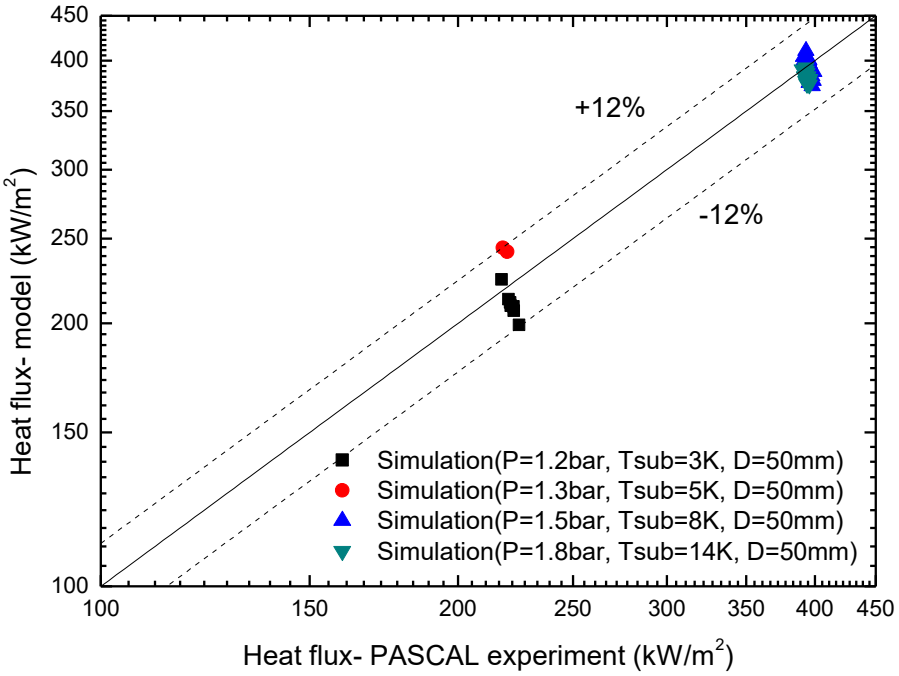

Figure 6. 16 Assessment results for PASCAL experiment

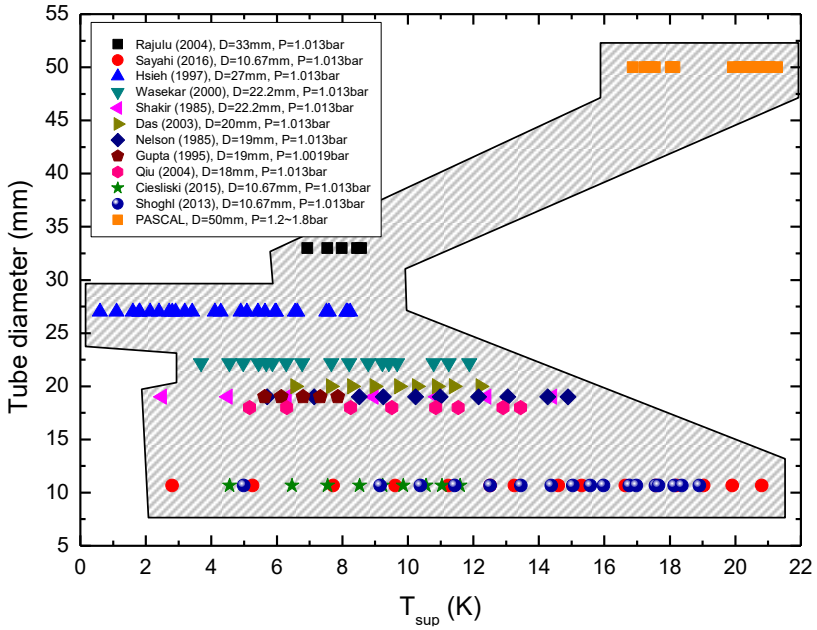

Figure 6. 17 Validation conditions to identify tube diameter effects

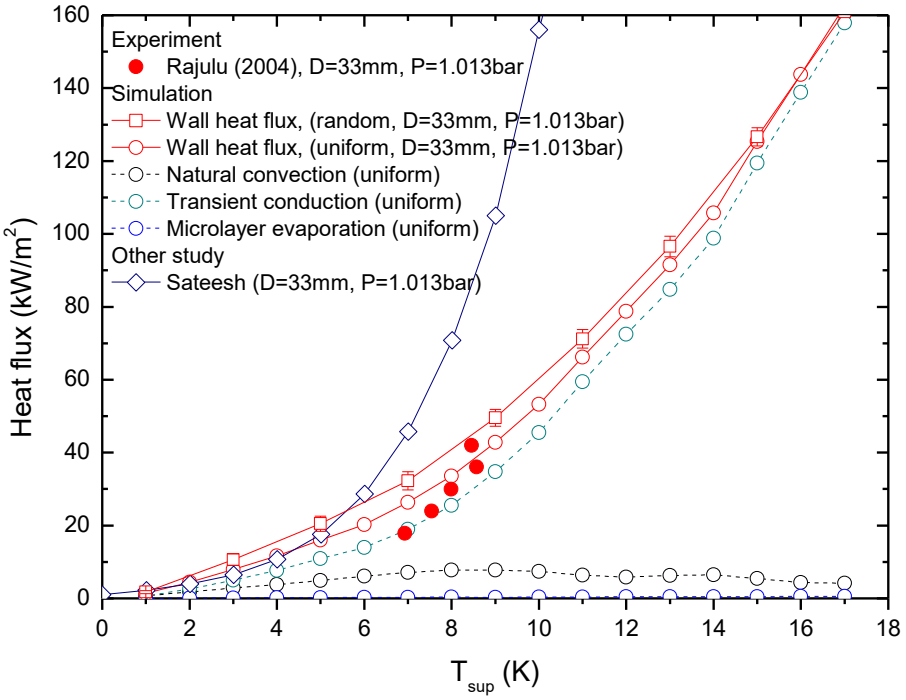

Figure 6. 18 Heat flux vs. wall superheat (D=33mm, P=1.013bar, Tsub=0.1K)

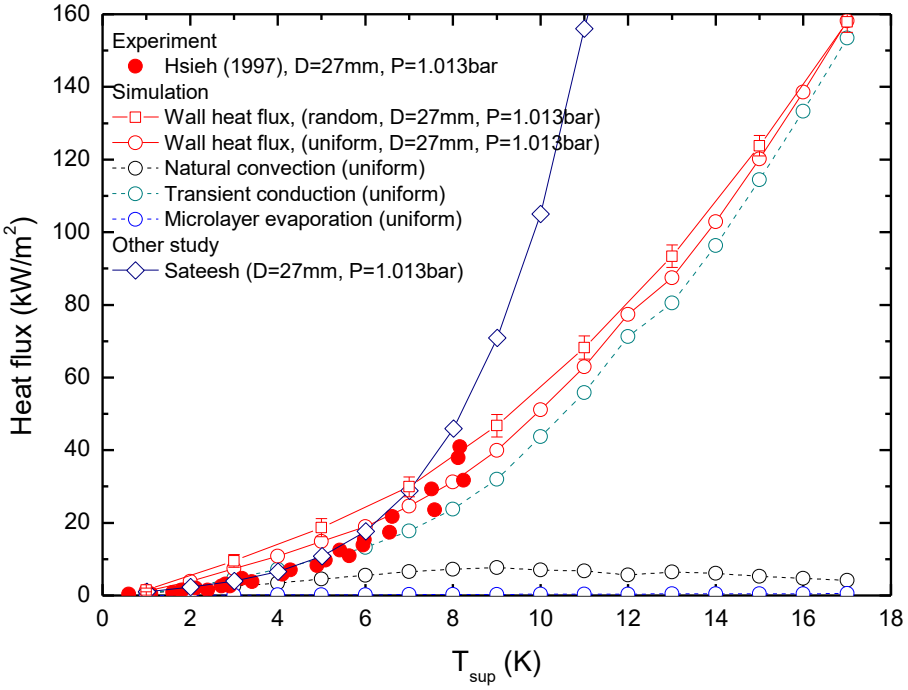

Figure 6. 19 Heat flux vs. wall superheat (D=27mm, P=1.013bar, Tsub=0.1K)

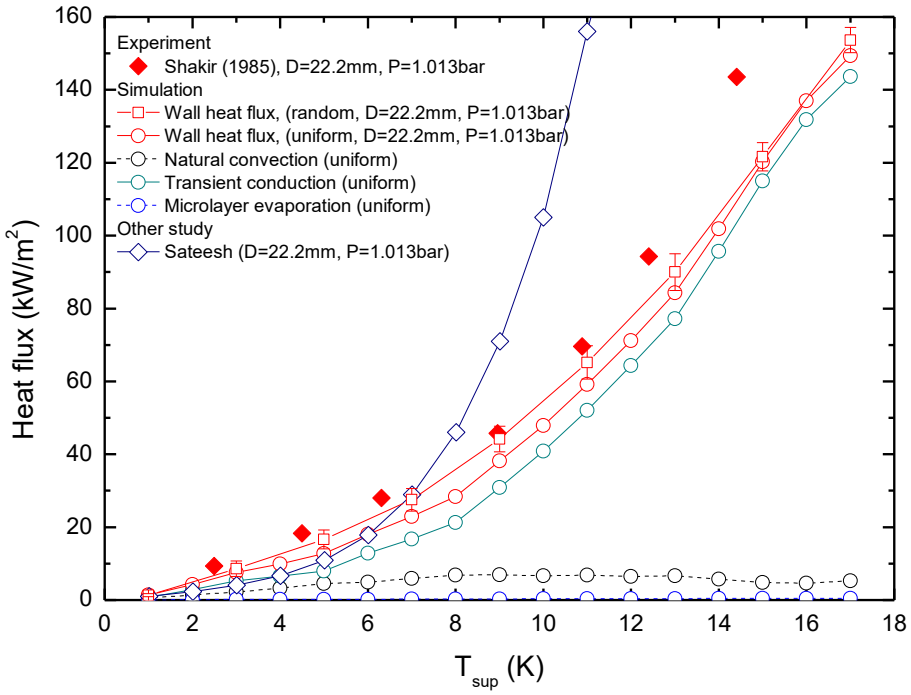

Figure 6. 20 Heat flux vs. wall superheat (D=22.2mm, P=1.013bar, Tsub=0.1K)

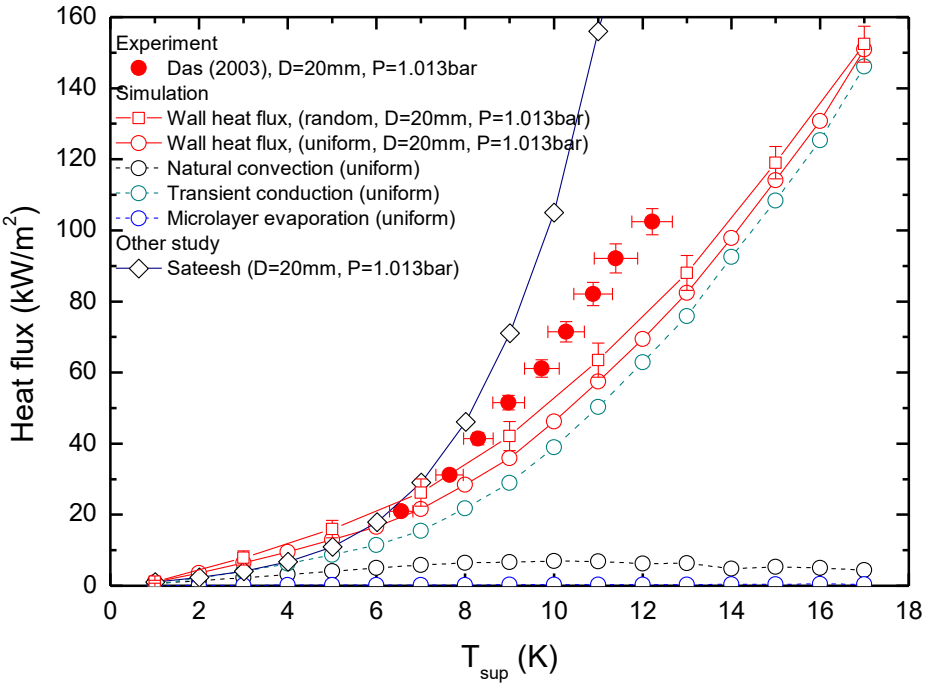

Figure 6. 21 Heat flux vs. wall superheat (D=20mm, P=1.013bar, Tsub=0.1K)

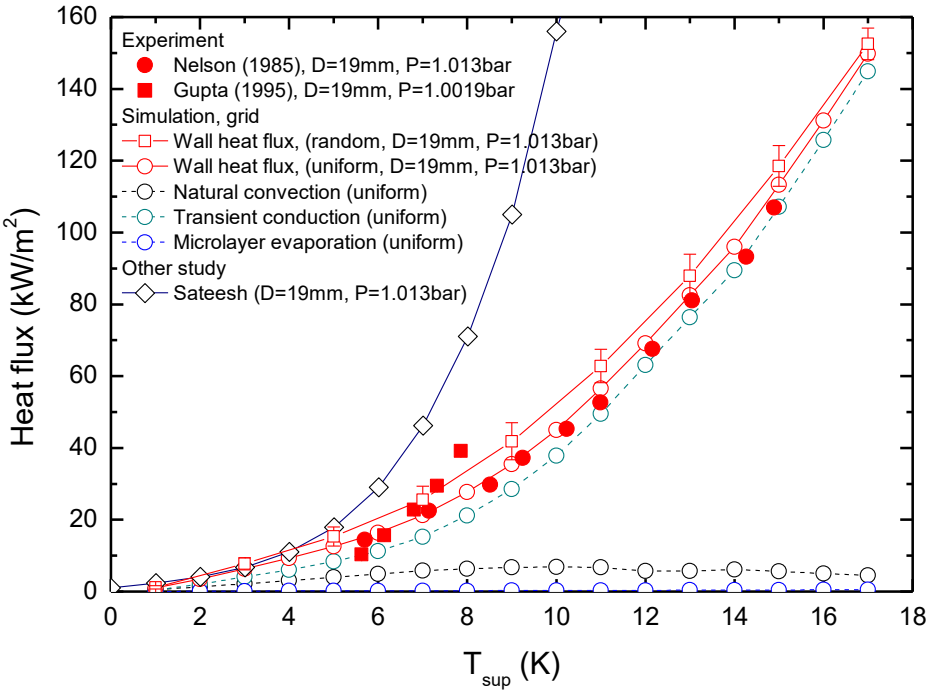

Figure 6. 22 Heat flux vs. wall superheat (D=19mm, P=1.013bar, Tsub=0.1K)

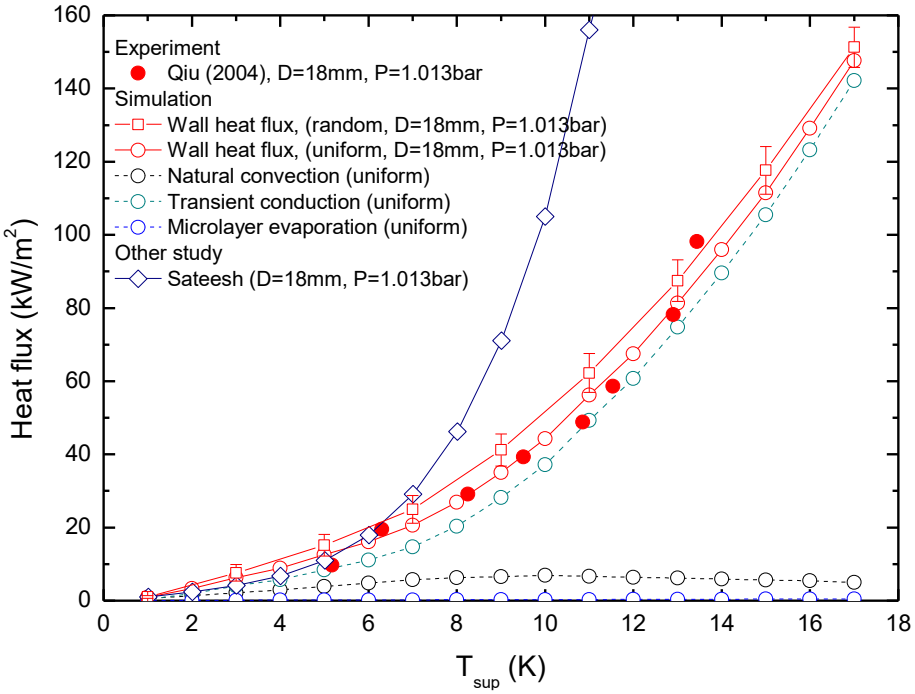

Figure 6. 23 Heat flux vs. wall superheat (D=18mm, P=1.013bar, Tsub=0.1K)

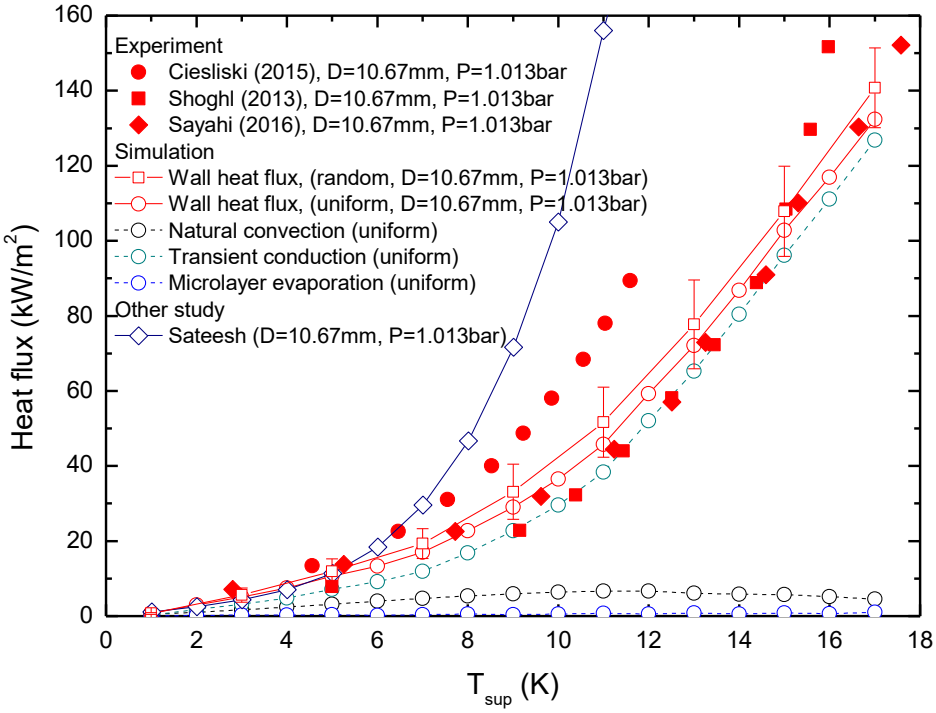

Figure 6. 24 Heat flux vs. wall superheat (D=10.67mm, P=1.013bar, Tsub=0.1K)

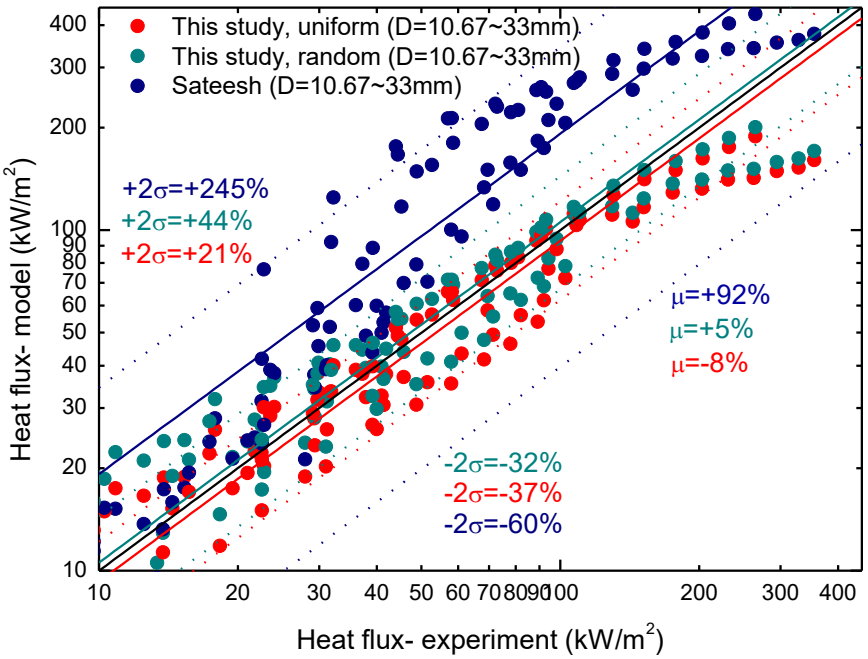

Figure 6. 25 Assessment results for various tube diameters

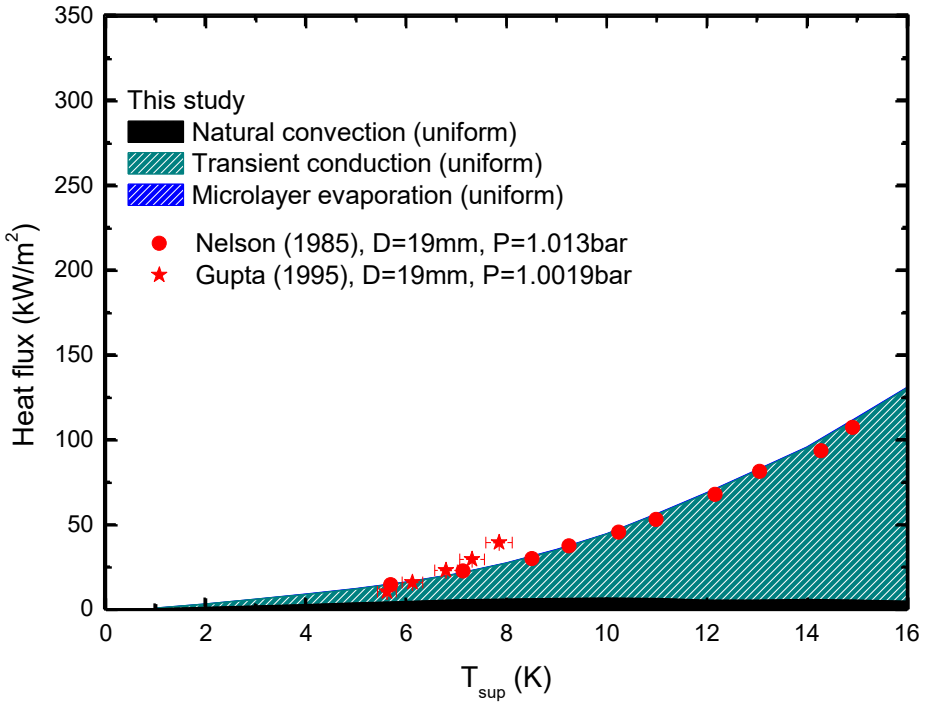

Figure 6. 26 Composition of heat flux vs. wall superheat
(D=19mm, P=1.013bar, Tsub=0.1K)

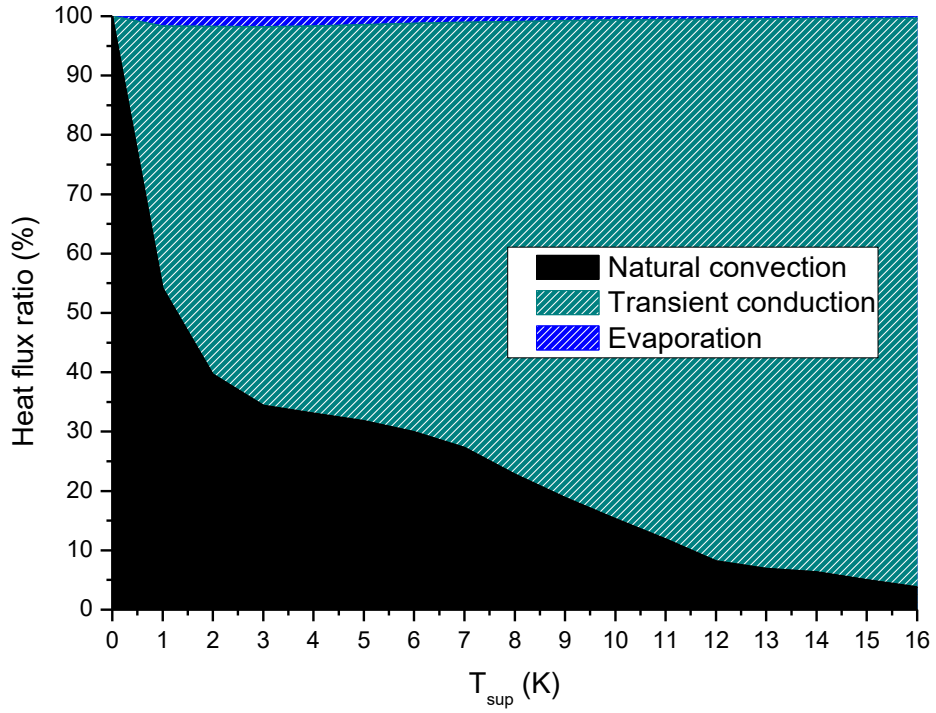

Figure 6. 27 Fractional contributions of different mechanisms at wall superheat
(D=19mm, P=1.013bar, Tsub=0.1K)

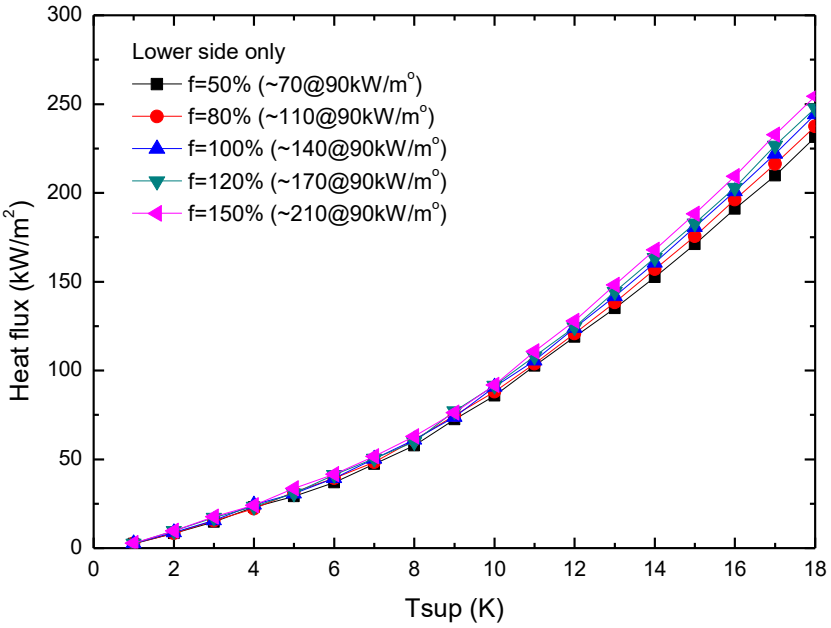

Figure 6. 28 Wall heat flux prediction results with varying the bubble frequency (D=33mm, T_sat, P_atm, Latin hypercube, lower side only)

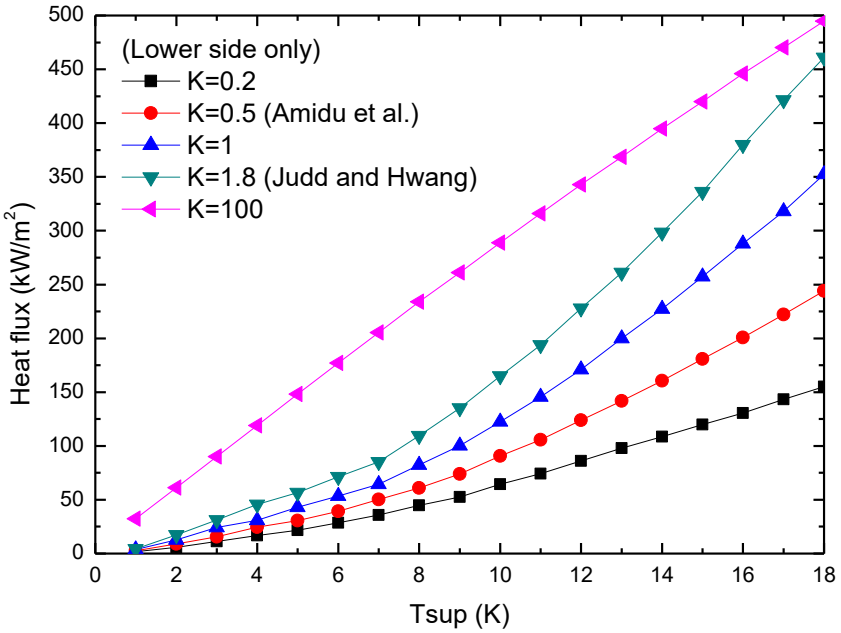

Figure 6. 29 Wall heat flux prediction results with varying the area of influence (D=33mm, T_sat, P_atm, Latin hypercube, lower side only)

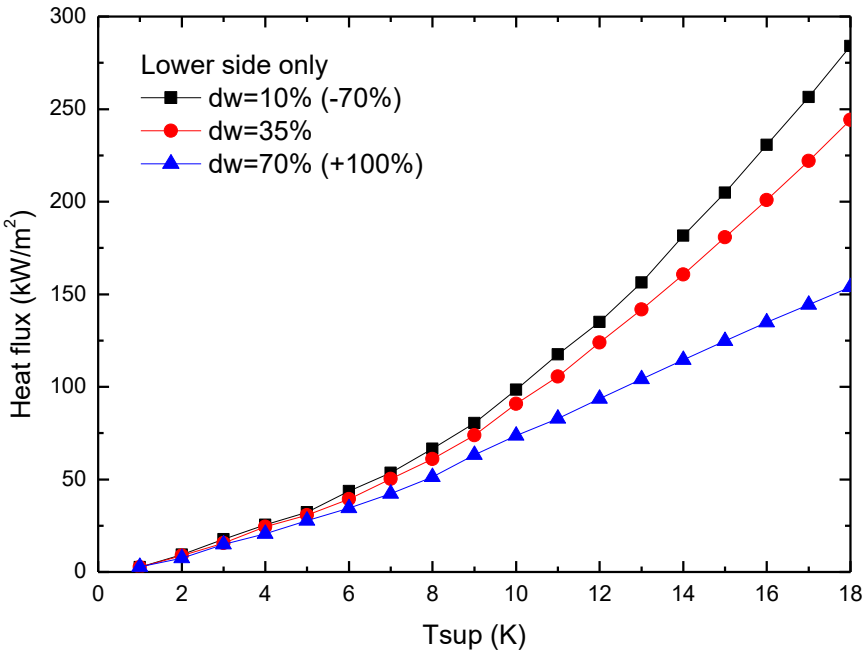

Figure 6. 30 Wall heat flux prediction results with varying the contact diameter (D=33mm, T_sat, P_atm, Latin hypercube, lower side only)

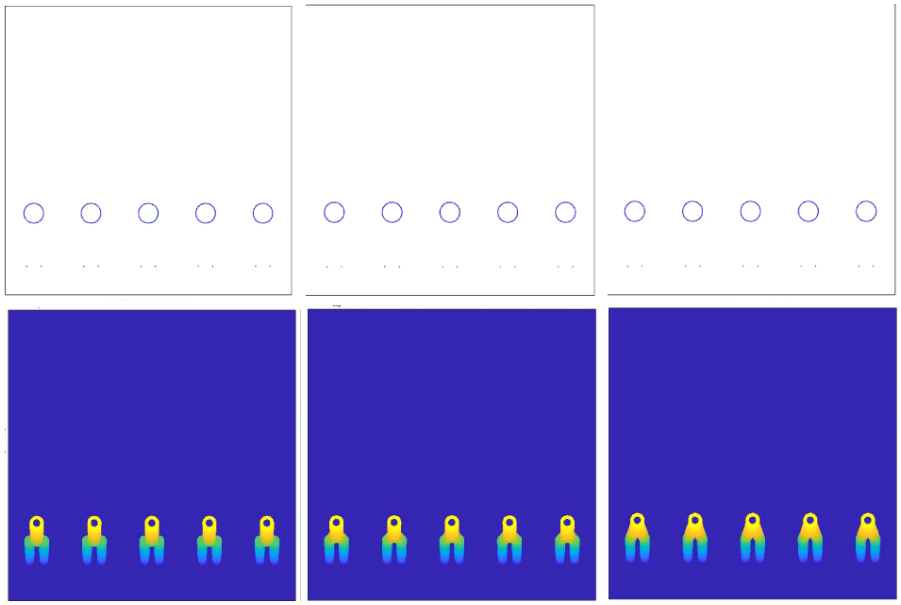

(a) (b) (c)

Figure 6. 31 Transient conduction with varying coalescence time (D=50mm, Tsup=20K, Tsat, P_atm, lower side only)

Chapter 7

Summary and conclusions

7.1 Summary

In this study, single bubble boiling experiments on the horizontal tube outside were conducted. Also, an image processing methodology for the analysis of experimental results was developed. As a results of the experiment, bubble growth rate, bubble velocity, contact diameter, bubble departure frequency, bubble departure diameter, etc. were obtained under the horizontal tube condition. A specially devised heater was fabricated for visualization experiment and boiling bubbles were generated along a thin heated surface to facilitate observation of a single bubble's motion. Also, a force balance model was derived to predict the sliding bubble behavior, where the curvature effect was included in an existing force balance model and cylindrical coordinates were adopted. The force balance formula was validated by comparison of the predicted bubble velocity with the experimental data. The analysis showed that the dominant forces were the buoyancy, quasi-steady drag, and added mass forces. The surface tension in the θ direction did not have a significant influence on the predicted sliding bubble velocity. The bubble velocity increased notably when the bubble frequency was high. It was assumed that the wake effect of the preceding bubble needs to be considered. The model predicted the bubble velocity within an error of about ±14% after the correction. In addition, development of the mechanistic and closure model for bubble departure sub-models on a horizontal tube were conducted. A bubble departure diameter model was developed, and the bubble radius model and the frequency model were closed by

using the experimental results. In addition, the bubble merging, the lift-off diameter, and the distribution of nucleation sites were solved with the numerical methods. Finally, the mechanistic heat transfer model was completed by determining the area ratio and heat flux for each heat transfer mechanism. The distribution of the nucleation sites in the model is determined by the options. Distribution options are uniform, random, and Latin hypercube. In the case of randomness, random or Latin hypercube, the average value and range of the calculation results are obtained using the Monte-Carlo method. Finally, the developed model was validated by experiments conducted at various diameters in previous studies and PASCAL experiments in which pressure and subcooling continued to change. As a result, the model reasonably predicts the wall heat flux. The predictive performance showed an error of less than ±30% at 2-sigma, with an average error of -8% in uniform sites and 5% in random sites. The developed model can be used not only to predict the heat transfer of the horizontal tube but also to assist the system code or commercial CFD code through coupling in the future.

7.2 Suggested future work

Since the wall boiling model developed in this study is based on a heat partitioning model, it can be used in coupling with TH code (system analysis code or CFD code) as well as stand alone use. As shown in Figure 7. 1, by coupling the model of this study, more diverse information can be exchanged realistically than the existing empirical correlation model. For coupling, the variables must be converted to the form required for the target code, and Figure 7. 2 shows the evaporation term change as an example in connection with the two-fluid model.

When the model is used independently, the total wall heat transfer is calculated from each wall heat flux mechanism. However, in order to link with the two-fluid model, it must be divided into the heat flux to vapor and the heat flux to liquid. This can be calculated through simple arithmetic processing in the model, and the equation is as follows:

Wall heat flux in the model

$$q_w^{"} = q_{tc}^{"} + q_{mev}^{"} + q_{sc}^{"} \tag{7.1}$$

Wall heat flux modification to coupling with the two-fluid model

$$q_w^{"} = q_{ev}^{"} + q_l^{"} = \left[\epsilon\left(q_{tc}^{"} + q_{sc}^{"}\right) + q_{mev}^{"}\right] + (1-\epsilon)\left(q_{tc}^{"} + q_{sc}^{"}\right) \tag{7.2}$$

In addition, it is expected that the model may be applicable to a wider range with the advanced variable assumptions. In order to improve the model, it is expected that some assumptions, such as the uniform wall superheats on the entire heating surface, the bubble shape assuming a spherical shape, and the assumptions that they are merged immediately after contact, can be applied to more realistic conditions.

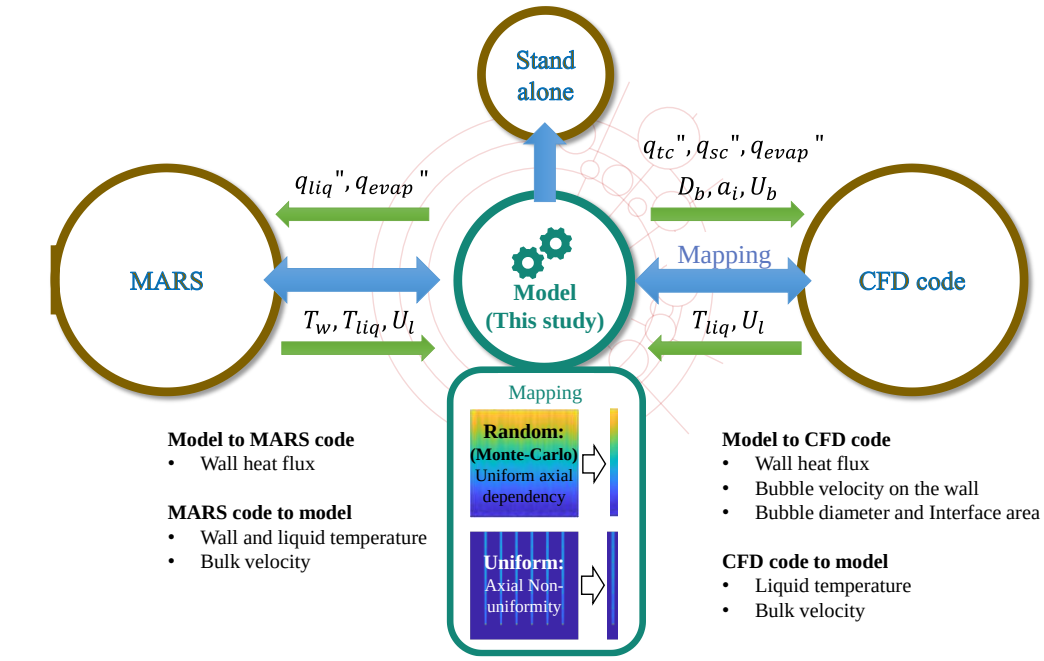

Figure 7. 1 Concept of coupling with system code and CFD code

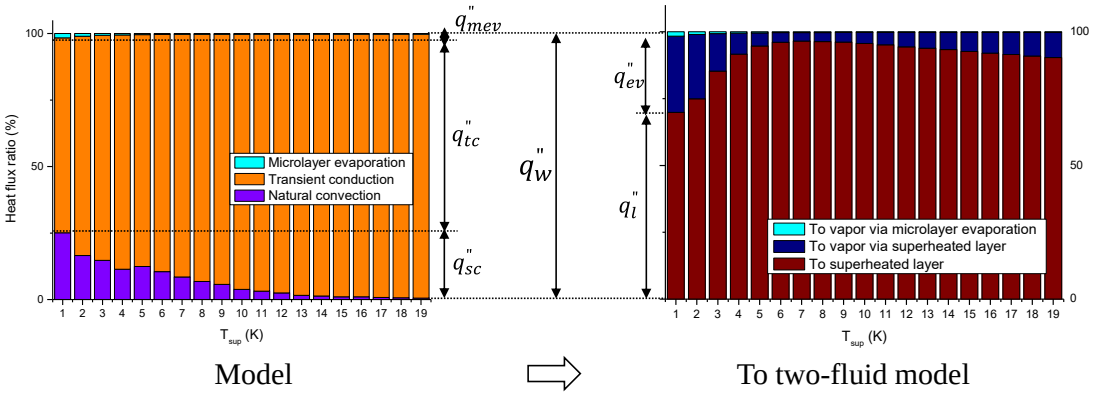

Figure 7. 2 Fraction of heat flux for linkage with the two-fluid model (D=33mm, T_sat, P_atm, Latin hypercube, lower side only)

Nomenclature

A	Cross-section of a bubble
A_s	Cross-section of a sliding bubble
Ar	Archimedes number
a	Linear acceleration
b	Bubble radius coefficient
C_D	Coefficient of drag
c_p	Specific heat
d_w	Contact diameter
F	Force
Fr	Froude number
f	Bubble frequency
g	gravitational acceleration
h_c	Condensation heat transfer coefficient
h_{fg}	Specific heat
I_{tc}	Transient conduction time index
Ja	Jakob number
K	Area of influence
k_l	Thermal conductivity of liquid
L_b	Non-dimensional distance of bubbles
l	Distance
l_c	Characteristic length
m	Mass
N_a	Nucleation site density
Nu	Nusselt number
n_b	Nucleation site density
Pr	Prandtl number

q	Heat flux
R	Distance between the centroids of the bubble and tube, bubble radius
R_a	Surface roughness
R_c	Minimum cavity radius
Ra	Reyleigh number
Re	Reynolds number
r_b	Radius of a bubble
T	Temperature
t	Time
t^*	Transient time
t_d	Departure time
t_l	Lift-off time
t_{sl}	Sliding time
t_w	Waiting time
U_b	Velocity of the bubble centroid
U_{bulk}	Bulk liquid velocity
U_l	Local liquid velocity around a bubble
U_r	Velocity of the bubble centroid in r-direction
V_b	Volume of a bubble
W	Linear interpolation weight factor
α	Upstream contact angle
α_l	Thermal diffusivity
α_θ	Angular acceleration
β	Downstream contact angle
δ_{ml}	Microlayer thickness
θ_0	Angle of the nucleation site
θ_b	Angle of the surface normal to the gravitational direction

θ_m	Mean angle of the surface normal to the gravitational direction
ρ	Density
σ	Surface tension
ν	Kinematic viscosity
χ_s	Parameter defined by the projected area and nucleation site density for sliding bubbles
χ_{st}	Parameter defined by the projected area and nucleation site density for stationary bubbles
ω_b	Bubble angular velocity

Subscript

am	Added mass
b	Bubble or buoyancy
calc	Calculation
ev	Evaporation
l	Liquid
me	Microlayer evaporation (due to stationary bubble)
mes	Microlayer evaporation (due to sliding bubble)
ml	Microlayer
nc	Natural convection
s	Surface tension
sat	Saturation
sc	Single-pahse convection
sl	Sliding
sub	Subcooling
sup	Superheated
qs	Quasi-steady drag
tc	Transient conduction (due to stationary bubble)

tcs	Transient conduction (due to sliding bubble)
tot	Total
v	Vapor
w	Wall
θ	Theta-directional

References

Amidu, M. A., Jung, S. & Kim, H., 2018. "Direct experimental measurement for partitioning of wall heat flux during subcooled flow boiling: Effect of bubble areas of influence factor". *International Journal of Heat and Mass Transfer,* Volume 127, p. 515–533.

Bae, B. U., Yun, B. J., Kim, S. & Kang, K. H., 2012. "Design of condensation heat exchanger for the PAFS (Passive Auxiliary Feedwater System) of APR+ (Advanced Power Reactor Plus)". *Annals of Nuclear Energy,* Volume 46, pp. 134-143.

Bae, B. U. et al., 2010. "Analysis of subcooled boiling flow with one-group interfacial area transport equation and bubble lift-off model". *Nuclear Engineering and Design,* 240(9), pp. 2281-2294.

Basu, N., Warrier, G. R. & Dhir, V. K., 2005. "Wall heat flux partitioning during subcooled flow boiling: part 1—model development". *Journal of Heat Transfer,* Volume 127, pp. 131-140.

Benjamin, R. J. & Balakrishnan, A. R., 1996. " Nucleate pool boiling heat transfer of pure l;iquids at low to moderate heat fluxes". *International Journal of Heat and Mass transfer,* Volume 39, pp. 2495-2504.

CD-adapco, 2013. *STAR-CCM+ Software Manual.* ed. : CD-adapco.

Chen, J. C., 1966. "Correlation for boiling heat transfer to saturated fluids in convective flow". *Industrial and Engineering Chemistry Process Design and Development,* 5(3), pp. 322-329.

Cho, S. H., Kim, S. H., Lee, J. G. & Lee, N. E., 2005. "Micro-scale metallization of high aspect-ratio Cu and Au lines on flexible polyimide substrate by electroplating using SU-8 photoresist mask". *Microelectronic Engineering,* 77(2),

pp. 116-124.

Cieslinski, J. T. & Kaczmarczyk, T. Z., 2015. "Pool Boiling of Water–Al2O3 and Water–Cu Nanofluids Outside Porous Coated Tubes". *Heat Transfer Engineering,* Volume 36, pp. 553-563.

Cole, R., 1967. "Bubble frequencies and departure volumes at subatmospheric pressures". *American Institute of Chemical Engineering Journal,* 13(4), pp. 779-783.

Colombo, M. & Fairweather, M., 2015. "Prediction of bubble departure in forced convection boiling: a mechanistic model". *International Journal of Heat and Mass Transfer,* Volume 85, pp. 135-146.

Cornwell, K. & Schuller, R. B., 1982. "A study of boiling outside a tube bundle using high speed photography". *International Journal of Heat and Mass transfer,* Volume 25, pp. 683-690.

Das, S. K., Putra, N. & Roetzel, W., 2003. Pool boiling of nano-fluids on horizontal narrow tubes. *International Journal of Multiphase Flow,* Volume 29, pp. 1237-1247.

Demiray, F. & Kim, J. H., 2004. "Microscale heat transfer measurements during pool boiling of FC-72: effect of subcooling". *International Journal of Heat and Mass Transfer,* 47(14-16), pp. 3257-3268.

Fiorenza, G. et al., 2013. *An innovative polyimide microchannels cooling system for the pixel sensor of the upgraded ALICE inner tracker.* Piscataway, NJ,, Proceedings of the 5th IEEE International Workshop on Advances in Sensors and Interfaces (IWASI), IEEE.

Gilman, L. & Baglietto, E., 2017. A self-consistent, physics-based boiling heat transfer modeling framework for use in computational fluid dynamics.

International Journal of Multiphase, Volume 95, pp. 35-53.

Gluntz, D. M. & Cooke, F. E., 1991. US, Patent No. 5,059,385.

Golobic, I. et al., 2009. "Experimental determination of transient wall temperature distributions close to growing vapor bubbles". *Heat and Mass Transfer,* Issue 45, pp. 857-866.

Gotoh, K., Nakata, Y. & Tagawa, M., 2003. "Wettability of ultraviolet excimer-exposed PE, PI and PTFE films determined by the contact angle measurements". *Colloids and Surfaces A: Physicochemical and Engineering Aspects,* 224(1), pp. 165-173.

Gupta, A., Saini, J. S. & Varma, H. K., 1995. "Boiling heat transfer in small horizontal tube bundles at low cross-flow velocities". *International Journal of Heat and Mass Transfer,* 38(4), pp. 599-605.

Han, C. Y. & Griffith, P., 1962. *The mechanism of heat transfer in nucleate pool boiling, Contract Nonr-1841 (39), Report No. 7673-19,* Cambridge 39, Massachusetts: Massachusetts Institute of Technology.

Hibiki, T. & Ishii, M., 2003. "Active nucleation site density in boiling systems". *International Journal of Heat and Mass Transfer,* 46(14), pp. 2587-2601.

Hoang, N. H., Chu, I. C., Euh, D. J. & Song, C. H., 2016. "A mechanistic model for predicting the maximum diameter of vapor bubbles in a subcooled boiling flow". *International Journal of Heat and Mass Transfer,* Volume 94, pp. 174-179.

Hsieh, S. S. & Weng, C. J., 1997. "Nucleate Pool Boiling Heat Transfer Coefficients of Distilled Water (H20) and R-134a/0il Mixtures From Rib-Roughened Surfaces". *Journal of Heat Transfer,* Volume 119, pp. 142-151.

Hwang, T. H. & Yao, S. C., 1986. "Forced convective boiling in horizontal tube bundles". *International Journal of Heat and Mass Transfer,* 29(5), pp. 785-795.

Ivey, H., 1967. "Relationships between bubble frequency, departure diameter and rise velocity in nucleate boiling". *International Journal of Heat and Mass Transfer,* 10(8), pp. 1023-1040.

Jakob, M., 1949. *Heat Transfer I.* New York: Wiley and Sons.

Jeon, S. S., 2015. *Development of heat transfer model for horizontal U-shaped heat exchanger submerged in pool.* s.l., Ph. D. thesis, Seoul National University.

Judd, R. L. & Hwang, K. S., 1976. "A comprehensive model for nucleate pool boiling heat transfer including microlayer evaporation". *Journal of Heat Transfer,* 98(4), pp. 623-629.

Jung, S. & Kim, H. D., 2015. "An Experimental Study on Heat Transfer Mechanisms in the Microlayer using Integrated Total Reflection, Laser Interferometry and Infrared Thermometry Technique". *Heat Transfer Engineering,* 36(12), pp. 1002-1012.

K. Stephan, 1992. *Heat Transfer in Condensation and Boiling.* New York: Springer-Verlag.

Kandlikar, S. G. & Stumm, B. J., 1995. "A Control Volume Approach for Investigating Forces on a Departing Bubble Under Subcooled Flow Boiling". *Journal of Heat Transfer,* Volume 117, pp. 990-997.

Kang, K. H. et al., 2012. "Separate and integral effect tests for validation of cooling and operational performance of the APR+ Passive Auxiliary Feedwater System,". *Nuclear Engineering and Technology,* Volume 44, pp. 597-610.

Kenning, D. B. R. & Yan, Y., 1996. "Pool boiling heat transfer on a thin plate: features revealed by liquid crystal thermography". *International Journal of Heat and Mass Transfer,* 39(15), pp. 3117-3137.

Kim, S. J. & Park, G. C., 2011. "Interfacial heat transfer of condensing bubble

in subcooled boiling flow at low pressure". *International Journal of Heat and Mass Transfer,* 54(13), pp. 2962-2974.

Kim, Y. N., Kim, J. S., Park, G. C. & Cho, H. K., 2017. "Measurement of sliding bubble behavior on a horizontal heated tube using a stereoscopic image processing technique". *International Journal of Multiphase Flow,* Volume 94, pp. 156-172.

Klausner, J. F., Mei, R., Bernhard, D. M. & Zeng, L. Z., 1993. "Vapor bubble departure in forced convection boiling". *International Journal of Heat and Mass Transfer,* 36(3), pp. 651-662.

Klausner, J. F., Mei, R., Bernhard, D. M. & Zeng, L. Z., 1993. "Vapor bubble departure in forced convection boiling". *International Journal of Heat and Mass Transfer,* 36(3), pp. 651-662.

Kurul, N. & M.Z. Podowski, 1990. Multidimensional effects in forced convection subcooled boiling. *Heat Transfer Conference,* Volume 2, pp. 21-26.

Kutateladze, S., 1961. Boiling heat transfer. *International Journal of Heat and Mass Transfer,* Volume 4, pp. 31-45.

Lee, D. H. et al., 2013. "Numerical evaluation of the cooling performance of a core catcher test facility". *Journal of Energy Engineering,* 22(1), pp. 8-16.

Maity, S., 2000. *"Effect of velocity and gravity on bubble dynamics" Thesis.*. s.l., University of California Los Angeles, Los Angeles, CA,.

Mikic, B. B., Rohsenow, W. M. & Griffith, P., 1970. "On bubble growth rates". *International Journal of Heat and Mass Transfer,* Volume 13, pp. 657-666.

Nelson, P. J. & Burnside, B. M., 1985. "Boiling the immiscible water/n-nonane system from a tube bundle". *International Journal of Heat and Mass Transfer,* 28(7), pp. 1257-1267.

Owoeye, E. J. & Schubring, D. W., 2015. *"Numerical study of bubble*

coalescence in sub-cooled flow boiling. Chicago, IL, NURETH-16.

Perry, R. H., Green, D. W. & Maloney, J. O., 1997. *Perry's Chemical Engineers' Handbook.* 7th edition ed. NewYork,NY: McGraw-Hill.

Plesset, M. & Zwick, S. A., 1954. The growth of vapor bubbles in superheated liquids. *Journal of Applied Physics,* Volume 25, pp. 493-500.

Polley, G. T., Ralston, T. & Grant, I. D. R., 1980. *"Forced crossflow boiling in an ideal in-line tube bundle".* New York, NY, Proceedings of the 19th National Heat Transfer Conference, ASME, Paper no. USA80-HT-46.

Qiu, D. & Dhir, V. K., 2002. "Experimental study of flow pattern and heat transfer associated with a bubble sliding on downward facing inclined surfaces". *Experimental Thermal and Fluid Science,* Volume 26, pp. 605-616.

Qiu, Y. H. & Liu, Z. H., 2004. "Boiling heat transfer of water on smooth tubes in a compact staggered tube bundle". *Applied Thermal Engineering,* Volume 24, pp. 1431-1441.

Rajulu, K. G., Kumar, R., Mohanty, B. & Varma, H. K., 2004. "Enhancement of nucleate pool boiling heat transfer coefficient by reentrant cavity surfaces". *Heat Mass Transfer,* Volume 41, pp. 127-132.

Rousselet, Y. L., 2014. *"Interacting Effects of Inertia and Gravity on Bubble Dynamics".* s.l., UCLA Electronic Theses and Dissertations.

Ryu, S. U., Kim, S. & Euh, D. J., 2014. *"Development of Lift-Off Diameter Model of Bubbles Generated on Horizontal Tube.".* s.l., In ASME 2014 International Mechanical Engineering Congress and Exposition (pp. V08BT10A055-V08BT10A055)., pp. (pp. V08BT10A055-V08BT10A055)..

Sateesh, G., S.K. Das & A.R. Balakrishnan, 2005. "Analysis of pool boiling heat transfer: effect of bubbles sliding on the heated surface". *International Journal*

of Heat and Mass Transfer, Volume 48, pp. 1543-1553.

Sayahi, T., Tatar, A. & Bahrami, M., 2015. "A RBF model for predicting the pool boiling behavior of nanofluids over a horizontal rod heater". *International Journal of Thermal Sciences,* Volume 99, pp. 180-194.

Scriven, L., 1959. On the dynamics of phase growth. *Chemical Engineering Science,* Volume 10, pp. 1-13.

Shakir, S., 1987. *Boiling incipience and heat transfer on sm ooth and enhanced surfaces.* s.l., Ph.D. thesis, Michigan State University.

Shoghl, S. N. & Bahrami, M., 2013. "Experimental investigation on pool boiling heat transfer of ZnO, and CuO water-based nanofluids and effect of surfactant on heat transfer coefficient". *InternationalCommunicationsinHeatandMassTransfer,* Volume 45, pp. 122-129.

Singh, R., J.S. Saini & H.K. Varma, 1985. Effect of cross-flow on boiling heat transfer of refrigerant-12. *International Journal of Heat and Mass Transfer,* 28(2), pp. 512-514.

Sugrue, R., Buongiorno, J. & McKrell, T., 2014. "An experimental study of bubble departure diameter in subcooled flow boiling including the effects of orientation angle, subcooling, mass flux, heat flux, and pressure". *Nuclear Engineering and Design,* Volume 279, pp. 182-188.

Sugrue, R., J. Buongiorno & T. McKrell, 2014. "An experimental study of bubble departure diameter in subcooled flow boiling including the effects of orientation angle, subcooling, mass flux, heat flux, and pressure". *Nuclear Engineering and Design,* Volume 279, pp. 182-188.

Sultan. M. & Judd. R. L., 1978. "patial distribution of active sites and bubble flux density". *Journal of Heat Transfer,* Volume 100, pp. 56-62.

Technology, A., 1997. *CFX-4.2 Solver Manual.* Didcot, Oxon, UK: .

The MathWorks Inc., 2019. *MATLAB manual, 2019. version R2019b.* s.l.:Natick, Massachusetts.

Theofanous, T. G. et al., 1997. "In-vessel coolability and retention of a core melt". *Nuclear Engineering and Design,* Volume 169, pp. 1-48.

Thorncroft, G. E. & Klausner, J. F., 2001. "Bubble forces and detachment models". *Multiphase Science and Technology,* 13(3&4), pp. doi: 10.1615/MultScienTechn.v13.i3-4.20..

Ünal, H., 1976. "Maximum bubble diameter, maximum bubble-growth time and bubble growth rate during the subcooled nucleate flow boiling of water up to 17.7 MN/m²". *International Journal of Heat and Mass Transfer,* Volume 19, pp. 643-649.

Van Helden, W. G. J., Van der Geld, C. W. M. & Boot, P. G. M., 1995. "Forces on Bubble Growing and Detaching in Flow Along a Vertical Wall". *International Journal of Heat and Mass Transfer,* 38(11), pp. 2075-2088.

Webb, R. L. & Gupte, N. S., 1992. "A critical review of correlations for convective vaporization in tubes and tube banks". *Heat Transfer Engineering,* 13(3), pp. 58-81.

Yeoh, G. H. & Tu, J. Y., 2004. "Population balance modelling for bubbly flows with heat and mass transfer". *Chemical Engineering Science,* 59(15), pp. 3125-3139.

Yeoh, G., S.C.P. Cheung, J.Y. Tu & M.K.M. Ho, 2008. Fundamental consideration of wall heat partition of vertical subcooled boiling flows. *International Journal of Heat and Mass Transfer,* Volume 51, pp. 3840-3853.

Yoo, J., Estrada-Perez, C. E. & Hassan, Y. A., 2018. "Area of bubble influence due to sliding bubbles in subcooled boiling flow".

InternationalJournalofHeatandMassTransfer, Volume 125, pp. 43-52.

Yoo, J., Estrada-Perez, C. E. & Hassan, Y. A., 2018. "Development of a mechanistic model for sliding bubbles growth prediction in subcooled boiling flow". *Applied Thermal Engineering,* Volume 138, pp. 657-667.

Yoshikawa, H. N. & Colin, C., 2010. *"Single Vapor Bubble Behavior in a Shear Flow in Microgravity".* Tampa, FI, 7th International Conference on Multiphase Flow (ICMF 2010).

Yu, D. I. et al., 2018. "Synchrotron x-ray imaging visualization study of capillary-induced flow and critical heat flux on surfaces with engineered micropillars". *Science Advances,* 4(2), p. e1701571.

Yun, B. J., Splawski, A., Lo, S. & Song, C. H., 2012. "Prediction of a subcooled boiling flow with advanced two-phase flow models". *Nuclear Engineering and Design,* Volume 253, pp. 351-359.

Yun, B., Splawski, A., Lo, S. & Song, C., 2010. "Prediction of a subcooled boiling flow with mechanistic wall boiling and bubble size models", tech. rep.: CD-adapco.

Zuber, N., 1961. "The dynamics of vapor bubbles in nonuniform temperature fields". *International Journal of Heat and Mass Transfer,* Volume 2, pp. 83-98.

Appendix A. Initial bubble parameters calculation code

```
%% Initial bubble parameters calculation

    disp(['Step1. Calculating initial bubble parameters'])
        for i=1:sitenum

        initangle(i,1)=pi/2*Y2(i);

        inputvar.Tsup=Tsup;
        inputvar.theta=initangle(i,1);
        inputvar.initR=0;
        inputvar.initU=0;
        inputvar.Tsub=Calcoption.Tsub;
        inputvar.pressure=Calcoption.pressure;
        inputvar.u_bulk=Calcoption.u_bulk;
        inputvar.r_tube=Calcoption.r_tube;
        inputvar.dryratio=Calcoption.dryratio;

        if lowertube==1

[angle,radius,velocity,frequency,Yoofindtime]=Step3_bubble_velocit
y_location(inputvar,Yoofindtime); % Appendix B.bubble velocity
calculation code
        else

[angle,radius,velocity,~,lift_off_d]=Step3_2bubble_velocity_locati
on_uppertube(inputvar); %Appendix B. bubble velocity calculation
code
        end

        radius=radius*100; %m to cm

        angle(velocity==0)=NaN;
        radius(velocity==0)=NaN;
        velocity(velocity==0)=NaN;

        angle=rmmissing(angle);
        radius=rmmissing(radius);
        velocity=rmmissing(velocity);

        bubble_t_int=round(round(1/frequency,3)/0.001); %bubble
time interval %%%%

            matsize=size(angle);
```

```
            for j=1:matsize

                for ff=0:ceil(frequency*totaltime)-1

                  if j+ff*bubble_t_int>frames
                      continue
                  end

                  if (j+ff*bubble_t_int<=0)||(i+ff*sitenum<=0)

                  end


theta_rr(j+ff*bubble_t_int,i+ff*sitenum)=angle(j); %rad
                radii(j+ff*bubble_t_int,i+ff*sitenum)=radius(j); %cm

velv_rr(j+ff*bubble_t_int,i+ff*sitenum)=velocity(j); %m/s

bubblelocationXaxis(j+ff*bubble_t_int,i+ff*sitenum)=X3(1,i); %[0
to 1]

                end
            end

        end

    %Delete zeros
    theta_rr(velv_rr == 0) = NaN;
    radii(velv_rr == 0) = NaN;
    velv_rr(velv_rr == 0) = NaN;
    bubblelocationXaxis(velv_rr == 0) = NaN;

    bubblelocationYaxis=theta_rr/(pi()/2); %Rad to coordinate
```

Appendix B. Bubble velocity prediction code

```
function
[theta_rr,radii,velv_rr,freq,Yoofindtime]=Step3_bubble_velocity_lo
cation(inputvar,Yoofindtime)

       Tsup=inputvar.Tsup;
       Tsub=inputvar.Tsub;
       pressure=inputvar.pressure;
       u_bulk=inputvar.u_bulk;
       thetainit=inputvar.theta;
       initbubbleR=inputvar.initR;
       initbubbleU=inputvar.initU;
       r_tube=inputvar.r_tube;
       dryratio=inputvar.dryratio;


%Calc option
initbubbleR=initbubbleR/100; %cm to m
 deltat=0.001;

if initbubbleU==0
    initbubbleU=0.000001;

end

Tsat= 273.15+XSteam('TSat_p',pressure); %K
rho_l=XSteam('rhoL_p',pressure); %input: MPa, Output:K
rho_v=XSteam('rhoV_p',pressure); %input: MPa, Output:K
surf_coeff=XSteam('st_p',pressure); %N/m
cpl=XSteam('CpL_p',pressure)*1000;
hfg=(XSteam('hV_p',pressure)-XSteam('hL_p',pressure))*1000;
kf=XSteam('tcL_p',pressure); %W/m-K
mu_l=XSteam('my_pT',pressure,Tsat-Tsub-273.15); %Pa-s
alpha_l=kf/(rho_l*cpl);

Pr=cpl*mu_l/kf;
Ja_sup=rho_l*cpl*Tsup/(rho_v*hfg);

%Heater property
kww=14.9;
rholw=7900;
cpw=477;

gammayoo=sqrt((kww*rholw*cpw)/(kf*rho_l*cpl));

%Bubble angle
```

```
alpha=15/180*pi();
beta=20/180*pi();
mangle=(alpha+beta)/2;


%% Bubble transient Yoo et al.
condfrac=0.5; %Assumed in Yoo et al.
byoo=0.24; %Yoo: irrespective of subcooled flow boiling conditions
or working fluids
Cyoo=0.1; %[1/K-s]
AmlAtot=1.22*gammayoo^(-0.79)*exp(-0.204*Ja_sup);
Aprimeyoo=2*gammayoo*Pr^(-0.5)*Ja_sup*alpha_l^(0.5)*AmlAtot+(1-
condfrac)*2*byoo*kf*Tsup/(rho_v*hfg*sqrt(pi*alpha_l));
Bprimeyoo=condfrac*Tsub*Cyoo/(1-rho_v/rho_l);

if initbubbleR>0

    if initbubbleR>max(Yoofindtime(2,:))

        if max(Yoofindtime(2,:))==0
            sstime=1;
        else
            sstime=max(Yoofindtime(1,:));
        end

        while (sstime)
            searchtime=0.001*sstime;


Yoofindtime(2,sstime)=(Aprimeyoo*searchtime^0.5.*(1+Bprimeyoo*sear
chtime/3))./(1+Bprimeyoo*searchtime); %[m]
            Yoofindtime(1,sstime)=sstime;
            if Yoofindtime(2,sstime)>initbubbleR
                break
            else
            sstime=sstime+1;
            end
        end

        timeinit=sstime*0.001;

    else

    [~,sstime]=min(abs(initbubbleR-Yoofindtime(2,:)));


    timeinit=sstime*0.001;

    end
```

```
else
    timeinit=0;
end

%% Departure diameter-JSK model
Cd=0.44;
l_c=(surf_coeff/(9.8*rho_l-rho_v))^0.5;
Fr_d=u_bulk/(9.8*(rho_l-rho_v)/rho_l*l_c)^0.5;
initbangle=20/180*pi; %Bubble initial contact angle
D_departure=2*l_c/(sin(thetainit))*(3/8*sqrt(0.25*Cd^2*Fr_d^4+16/3
*sin(thetainit)*sin(initbangle)*(1-cos(initbangle)))-
3/16*Cd*Fr_d^2);
if D_departure<=0
    D_departure=0.000001;
end

%%Bubble frequency
freq=(4*9.8*(rho_l-rho_v)/(3*D_departure*rho_l))^0.5; %Cole

% for reduce calculationtime, preallocation
time=(timeinit:deltat:timeinit+199*deltat);
radius_b=(Aprimeyoo*time.^0.5.*(1+Bprimeyoo*time/3))./(1+Bprimeyoo
*time); %[m]
Vb=4/3*pi()*radius_b.^3; %[m3]
A_proj=pi()*radius_b.^2;
contactd=D_departure*0.35;
C_d=0.44;

j=1;

while (1)

vel_bubble=zeros(1,200);
deltatheta=zeros(1,200);
theta=zeros(1,200);

theta(1)=thetainit; %rad [0 to pi/2]
vel_bubble(1)=initbubbleU;

i=1;
kfc=200;

while(1)

    if i>kfc
        time=(timeinit:deltat:timeinit+(i-2+kfc)*deltat);

radius_b=(Aprimeyoo*time.^0.5.*(1+Bprimeyoo*time/3))./(1+Bprimeyoo
*time); %[m]
```

```
        Vb=4/3*pi()*radius_b.^3; %[m3]
        A_proj=pi()*radius_b.^2;
        vel_bubble(1,i-1+kfc)=0;
        deltatheta(1,i-1+kfc)=0;
        theta(1,i-1+kfc)=0;
        kfc=kfc+200;
    end

f_b=(rho_l-rho_v)*9.8*Vb(i)*sin(theta(i));
if (vel_bubble(i)-u_bulk)>=0
    f_qs=-1/2*C_d*rho_l*(vel_bubble(i)-u_bulk)^2*A_proj(i);
else
    f_qs=1/2*C_d*rho_l*(vel_bubble(i)-u_bulk)^2*A_proj(i);
end
f_surface=contactd*surf_coeff*pi()*(alpha-beta)/(pi()^2-(alpha-
beta)^2)*(sin(alpha)+sin(beta));

force=f_b+f_qs+f_surface;

if (Vb(i)<=0)||(force<=0)
    acc=0;

else
acc=force/(Vb(i)*(rho_v+rho_l));
end

if (theta(i)>=pi/2)
    break
end
vel_bubble(i+1)=vel_bubble(i)+acc*deltat;
deltatheta(i)=vel_bubble(i)*deltat/r_tube;
theta(i+1)=theta(i)+deltatheta(i);

i=i+1;

end

time=time(vel_bubble>0);
radius_b=radius_b(vel_bubble>0);
Vb=Vb(vel_bubble>0);
vel_bubble=vel_bubble(vel_bubble>0);
theta=theta(vel_bubble>0);

u_bulk_corr=max((0.625-
0.125*(mean(vel_bubble)/freq/((mean(Vb)*3/4/pi())^(1/3))))*(mean(v
el_bubble)+u_bulk(1)),u_bulk(1));

if abs(u_bulk_corr-u_bulk)<0.0001
    break
end
```

```
u_bulk=u_bulk_corr;
j=j+1;

end

velv_rr=vel_bubble';
theta_rr=theta';
radii=radius_b';



end
```

Appendix C. Bubble merger code

```
%% Bubble Merger

mergetracking=zeros(frames,2);
bubbletracking=zeros(frames,2);

disp(['Step2. Calculating merge'])
for timeline=1:frames
 disp(['Merge calculating frame no.: ',num2str(timeline),' /
',num2str(frames)])

    fff=0; %For merging bubble number tracking

    k=1; %0426
    while(k<=matsizenum-1) %0426

       if
isnan(radii(timeline,k))||(theta_rr(timeline,k)>pi/2) %For reduce
calculation time
           k=k+1; %0426
           continue
       end

       %Merge check
       m=k+1;
       while(m<=matsizenum) %0426

           if
isnan(radii(timeline,m))||(theta_rr(timeline,m)>pi/2) %For reduce
calculation time
               m=m+1; %0426
           continue
           end

       dist=sqrt(  ((bubblelocationXaxis(timeline,m)-
bubblelocationXaxis(timeline,k))*gridwidth)^2
+(  (radii(timeline,m)*cos(asin(dryratio))+r_tube*100*
cos(asin(radii(timeline,m)/(r_tube*100)*dryratio)) )^2 +
(radii(timeline,k)*cos(asin(dryratio))+r_tube*100*
cos(asin(radii(timeline,k)/(r_tube*100)*dryratio)) )^2 -
2*(radii(timeline,m)*cos(asin(dryratio))+r_tube*100*
cos(asin(radii(timeline,m)/(r_tube*100)*dryratio)) ) *
(radii(timeline,k)*cos(asin(dryratio))+r_tube*100*
cos(asin(radii(timeline,k)/(r_tube*100)*dryratio)) ) *
cos(abs(theta_rr(timeline,m)-theta_rr(timeline,k))) ));%cm
       radsum=radii(timeline,m)+radii(timeline,k); %[cm]
```

```
            if dist<=radsum
                clear angle radius velocity newXaxis
                wei_k=4/3*pi()*radii(timeline,k)^3;
                wei_m=4/3*pi()*radii(timeline,m)^3;


newradius=((4/3*pi()*radii(timeline,k)^3+4/3*pi()*radii(timeline,m
)^3)*3/4/pi())^(1/3); %[cm]

newvelocity=(wei_k*velv_rr(timeline,k)+wei_m*velv_rr(timeline,m))/
(wei_k+wei_m);    %Momentum conservation

newangle=(theta_rr(timeline,k)*wei_k/(wei_k+wei_m)+theta_rr(timeli
ne,m)*wei_m/(wei_k+wei_m));

newXaxis=bubblelocationXaxis(timeline,k)*wei_k/(wei_k+wei_m)+bubbl
elocationXaxis(timeline,m)*wei_m/(wei_k+wei_m);

                fff=fff+1;

                inputvar.Tsup=Tsup;
                inputvar.theta=newangle;
                inputvar.initR=newradius;
                inputvar.initU=newvelocity;
                inputvar.Tsub=Calcoption.Tsub;
                inputvar.pressure=Calcoption.pressure;
                inputvar.u_bulk=Calcoption.u_bulk;
                inputvar.r_tube=Calcoption.r_tube;
                inputvar.dryratio=Calcoption.dryratio;

            if lowertube==1

[angle,radius,velocity,~,Yoofindtime]=Step3_bubble_velocity_locati
on(inputvar,Yoofindtime); %output [rad, m, m/s, 1/s], input [K,
rad[0to pi/2], cm, m/s]
            else

[angle,radius,velocity,~,~]=Step3_2bubble_velocity_location_uppert
ube(inputvar);
            end
                matsizere=size(angle);
                radius=radius*100; %m to cm

                %Delete matrix for bubble merger
                for n=timeline:frames
                radii(n,k)=NaN;
                radii(n,m)=NaN;

                theta_rr(n,k)=NaN;
                theta_rr(n,m)=NaN;
```

```
                velv_rr(n,k)=NaN;
                velv_rr(n,m)=NaN;

                bubblelocationXaxis(n,k)=NaN;
                bubblelocationXaxis(n,m)=NaN;

                bubblelocationYaxis(n,k)=NaN;
                bubblelocationYaxis(n,m)=NaN;
                end

                %Update new matrix for merged bubbles
                   for jj=1:matsizere

                      if timeline-1+jj>frames
                         continue
                      end
                      theta_rr(timeline-1+jj,k)=angle(jj,1);
                      radii(timeline-1+jj,k)=radius(jj,1);
                      velv_rr(timeline-1+jj,k)=velocity(jj,1);
                      bubblelocationYaxis(timeline-
1+jj,k)=angle(jj,1)/(pi/2);

                      bubblelocationXaxis(timeline-1+jj,k)=newXaxis;
                   end

                m=m+1;

             else
                m=m+1; %if not merged in this time, m=m+1, m number
to re-check merge
             end

          end

          if m==matsizenum+1
          k=k+1;
          end

       end

       mergetracking(timeline,1)=timeline;
       mergetracking(timeline,2)=fff;

       bubbletracking(timeline,1)=timeline;
       bubbletracking(timeline,2)=sum(~isnan(radii(timeline,:)));
end

if lowertube==1
```

```
   r_liftoff=radii(theta_rr>(pi/2)); %cm
else
   r_liftoff=radii( (radii>=lift_off_d*100) |
~isnan(radii(frames,:)) ); %cm
end
r_liftoff=r_liftoff(~isnan(r_liftoff)); %Delete NaNs
r_liftoff=nonzeros(r_liftoff); %Delete zeros

V_liftoff=4/3*pi()*r_liftoff.^3; %cm3
V_lift_avg=mean(V_liftoff); %cm3
V_lift_sum=sum(V_liftoff); %cm3
count_lift=size(r_liftoff,1);

Step5_transient


end
```

Appendix D. Transient conduction calculation code

```
% Set resolution
resolution=1024;

%Geometry
r_tube=Calcoption.r_tube;
gridwidth=r_tube*100*pi()/2; %cm
fromtime=Calcoption.fromtime; %First TC frame time
timerange=Calcoption.timerange;  %Time duration for average

%Fluid property
pressure=Calcoption.pressure;
Tsat= 273.15+XSteam('TSat_p',pressure);
Tsub=Calcoption.Tsub;
rho_l=XSteam('rhoL_p',pressure); %input: MPa, Output:K
cpl=XSteam('CpL_p',pressure)*1000;
kf=XSteam('tcL_p',pressure); %W/m-K
mu_l=XSteam('my_pT',pressure,Tsat-Tsub-273.15); %Pa-s
alpha_l=kf/(rho_l*cpl);
beta=0.0007453; %¥â is the coefficient of thermal expansion (equal
to approximately 1/T, for ideal gases)

visk=mu_l/rho_l;
Grl=9.8*beta*(Tsup+Tsub)*(2*r_tube)^3/visk^2;
Pr=cpl*mu_l/kf;
hfc_jeon_lower=0.0117*(Grl*Pr)^0.514*kf/(2*r_tube); %Lower tube,
Natural convection tube num
t_star=(kf/hfc_jeon_lower)^2/(pi*alpha_l);
t_star=floor(t_star*1000);
transienttime=t_star;
areaofinfluence=0.707;

timeinterval=0.001;

areamatrix=zeros(resolution,resolution,timerange);
disp(['Step3. Calculating T.C.'])
for ttt=fromtime:fromtime+timerange-1
clear bubblelocationforarea drawarea


bubblelocationforarea(:,1)=reshape(bubblelocationXaxis(ttt,:),[],1
);
```

```
bubblelocationforarea(:,2)=reshape(bubblelocationYaxis(ttt,:),[],1
);

bubblelocationforarea(:,3)=reshape(radii(ttt,:)/gridwidth,[],1); %
[cm]
    bubblelocationforarea=rmmissing(bubblelocationforarea);

    bubbleareacount=size(bubblelocationforarea);

    drawarea=resolution*bubblelocationforarea; %convert axis to
resolution, Xaxis, Yaxis, Radius


    for arr=1:bubbleareacount(1)    %draw bubble at this time

        for tt=0:0.001:2*pi %Draw bubble

xposition=round(areaofinfluence*drawarea(arr,3)*cos(tt)+drawarea(a
rr,1)); %R*cos(tt)+X

yposition=round(areaofinfluence*drawarea(arr,3)*sin(tt)+drawarea(a
rr,2)); %R*sin(tt)+Y

            if xposition<=0  %boundary
                xposition=1;
            elseif xposition>resolution
                xposition=resolution;
            end
            if yposition<=0
                yposition=1;
            elseif yposition>resolution
                yposition=resolution;
            end

            areamatrix(xposition,yposition,ttt-
fromtime+1)=transienttime-1; %Time level

        end

    end

    areamatrix(:,:,ttt-fromtime+1)=imfill(areamatrix(:,:,ttt-
fromtime+1),'holes');  %Fill holes


 for arr=1:bubbleareacount(1)    %draw bubble dry region at this
time
    for tt=0:0.001:2*pi %Draw bubble
```

```
xposition_dry=floor(dryratio*drawarea(arr,3)*cos(tt)+drawarea(arr,
1)); %R*cos(tt)+X

yposition_dry=floor(dryratio*drawarea(arr,3)*sin(tt)+drawarea(arr,
2)); %R*sin(tt)+Y

                if xposition_dry<=0  %boundary
                  xposition_dry=1;
                 elseif xposition_dry>resolution
                 xposition_dry=resolution;
                end

               if yposition_dry<=0
                yposition_dry=1;
                elseif yposition_dry>resolution
                yposition_dry=resolution;
                end

          areamatrix(xposition_dry,yposition_dry,ttt-
fromtime+1)=transienttime; %Time level

    end
 end

    areamatrix(:,:,ttt-fromtime+1)=imfill(areamatrix(:,:,ttt-
fromtime+1),'holes');  %Fill holes


    if not(ttt-fromtime+1==1)
        for xpixel=1:resolution
            for ypixel=1:resolution
                if (~areamatrix(xpixel,ypixel,ttt-fromtime+1)) &&
(areamatrix(xpixel,ypixel,ttt-fromtime+1-1))
                    if areamatrix(xpixel,ypixel,ttt-fromtime+1-1)==1
                    areamatrix(xpixel,ypixel,ttt-fromtime+1)=0;
                    else
                    areamatrix(xpixel,ypixel,ttt-
fromtime+1)=areamatrix(xpixel,ypixel,ttt-fromtime+1-1)-1;
                    end
                end
            end
        end
    end

end

    trange=size(areamatrix);
    %Convert time level to transient conduction
```

```
fcarea=sum((areamatrix==0),'all')/(trange(3)*resolution^2);    %
time, area averaged: forced convection only

dryarea=sum((areamatrix==transienttime),'all')/(trange(3)*resoluti
on^2); %time, area averaged: dry only
   tcarea=1-(fcarea+dryarea);    % time, area averaged: transient
conduction

   areamatrix(areamatrix == 0) = NaN;
   areamatrix(areamatrix == transienttime) = NaN;
   transientmatrix=1/(sqrt(deltat*(transienttime-
areamatrix))); %Time level to transient conduction

   avgTCi=nanmean(transientmatrix,'all');    %average TC intensity

   if isnan(avgTCi)
      avgTCi=0;
   end
```

국문 초록

최근에는 원자로 계통의 성능과 건전성 향상을 위해서 shell-and-tube 타입의 열교환기를 포함하여 다양한 형상의 피동안전계통이 개발되고 있다. 열교환기는 그 형태에 따라 비등 열전달량이 크게 좌우되기 때문에 정확한 계통의 성능을 평가하기 위해서는 실험과 분석을 통해 충분히 검증되어야 한다.

열분배 모델 (the heat-partitioning model)은 기구학적 비등열전달 모델 (the mechanistic boiling heat transfer model)의 하나로 실제 비등 열전달 현상의 원리에 기반하고 있다. 모델은 비등열전달이 일어나는 원리인 증발 (evaporation), 과도열전도 (transient conduction), 단상대류 (single-phase convection)의 총 합으로 전체 벽면열전달량을 계산하게 되며, 각 원리마다 주요 기포 변수 서브모델들이 직접적으로 포함된다. 열분배 모델은 원리에 기반한 특징으로 인해 좋은 적용성을 인정받아 현재 CFD (computational fluid dynamics)등의 비등열전달 예측에 널리 사용되고 있다.

본 연구의 대상인 수평관 열교환기에서는 기포의 생성지점 위치에 따라 다양한 기포의 거동과 특성을 보이는 특징이 있다. 열분배 모델에서는 기포의 거동이 직접적으로 비등열전달에 반영이 되어 전체 열전달량 예측에 영향을 미친다. 따라서 열교환기의 형상과 구조적 특성을 반영한 실험과 검증에 기반하여 기포거동 서브모델들이 개발되고 반영되어야 한다.

그러나 기존의 열분배모델은 대부분 수직관이나 평면 구조를 대상으로 연구되었다. 일부 모델이 수평관에 대해 사용될 수 있다고 주장하고 있으나, 이들 모델은 수평관 실험에 기반하지 않은 채 수평관의 구조적 특징이 고려되지 않은 서브모델들을 사용하였거나, 과도하게 단순화된 가정들에

기반하고 있다. 이는 기존의 연구에서 수평관에서의 단일 기포 실험이 아직 실시되거나 검증되지 않았기 때문이다.

따라서 본 연구는 수평관에서의 기구학적 비등열전달 개발을 목표로 하였다. 이를 위해서 수평관 외벽에서의 단일 비등기포 실험을 실시하여 기포 거동과 관련된 주요 변수 (기포 성장률, 기포 속도, 접촉지름, 기포이탈빈도, 기포 이탈 직경 등)를 취득하였다. 가시화 실험을 위해서 얇은 가열면의 특수 히터를 개발하여 단일 기포 거동의 관측을 용이하게 하였으며, 양 방향에서 촬영한 기포 영상의 이미지 분석방법론을 개발하여 실험 결과를 분석하였다.

실험 결과를 근거로 이들 주요 변수의 서브모델을 독립적으로 개발하거나 기존 모델의 수평관 적용 가능성을 검증하였다. 또한 기존에 수직면을 대상으로 개발된 힘분석모델(the force balance model)을 수평관 형상에 대응하는 원통좌표계(cylindrical coordinate system)에 맞게 유도하여 곡률 효과를 고려한 단일기포의 거동과 속도 예측에 사용하였다. 또한 현상적으로 복잡한 특성으로 인해 해석적으로 다루기 어려운 부상직경 (lift-off diameter), 기포생성지점분포 (distribution of nucleation sites), 기포합병 (bubble merging)등은 수치적으로 모델링 (numerical modelling)하였다. 이렇게 검증 및 개발한 서브모델과 수치적 모델링을 통해 수평관에서의 기구학적 비등열전달 모델을 제시하였다.

개발한 모델은 다양한 지름을 가진 수평관에서 실시된 기존 연구들과, 다양한 압력과 과냉도를 가진 KAERI의 PASCAL 실험 결과를 통해 검증하였다. 검증 결과, 모델을 통해 실험 결과가 타당한 수준에서 예측되고 있음을 확인하였다.

본 연구는 비등 기포 활주 현상에 대한 실험방법론, 실험 결과, 서브모델 개발, 기구학적 비등열전달 모델 개발과 검증결과를 다루고 있다. 이를

통해서 적절한 예측 성능을 지닌 수평관 비등열전달 모델을 개발하였고, 제시한 모델은 비등열전달 예측에 단일적으로 사용될 뿐만 아니라, 추후 시스템 코드나 상용 CFD 코드와의 연계를 통해 넓은 확장성을 지닐 수 있을 것으로 판단된다.

주요어

비등, 수평관, 벽면열속, 기구학적 비등모델, 열분배모델, FPCB, 단일기포, 자연대류, 활주기포, 힘분배모델, 기포속도, 기포합병, 기포추적, 핵비등생성지점분포, 몬테칼로방법론, PAFS, PASCAL

학번: 2015-30289